

O domínio laterítico do Centro Oeste brasileiro: características do regolito e dinâmica

The Brazilian Midwest lateritic domains:
regolith features and dynamic

RODRIGO TOKUTA CASTRO

Tese de Doutorado Nº 199

Orientador: Prof. Dr. Adriana Maria Coimbra Horbe

O domínio laterítico do Centro Oeste brasileiro: características do regolito e dinâmica

The brazilian midwest lateritic domains:
regolith features and dynamic

RODRIGO TOKUTA CASTRO

Tese apresentada ao Programa de Pós-Graduação em Geologia – Instituto de Geociências – IG da Universidade de Brasília – UnB como requisito parcial obrigatório para a obtenção do título de Doutor em Geologia.

Área de concentração:
Geologia Regional

Orientador: Prof. Dr. Adriana Maria Coimbra

Co-orientador: Prof. Maurício Parra

Comissão Examinadora:

- Prof. Dr. Adriana Maria Coimbra Horbe (IG/UnB);
Prof. Dr. Tiago Amâncio Novo (UFMG);
Prof. Dr. Maria Lídia Medeiros Vignol (UFRGS);
Prof. Dr. Elton Luiz Dantas (IG/UnB);
Prof. Dr. Jeremie Garnier (Suplente IG/UnB).

Ficha catalográfica elaborada automaticamente,
com os dados fornecidos pelo(a) autor(a)

TC355d Tokuta Castro, Rodrigo
O domínio laterítico do Centro Oeste brasileiro:
características do regolito e dinâmica / Rodrigo Tokuta
Castro; orientador Adriana Maria Coimbra Horbe. -- Brasília,
2023.
99 p.

Tese(Doutorado em Geologia) -- Universidade de Brasília,
2023.

1. Regolito. 2. Crostas lateríticas ferruginosas. 3.
Episódios lateríticos. 4. Superfície paleointempérica. 5.
Traços de fissão em apatita. I. Maria Coimbra Horbe,
Adriana, orient. II. Título.

AGRADECIMENTOS

Agradeço a Deus pelo dom da vida, das bençãos em minha vida e a conclusão deste trabalho.

Agradeço aos meus pais Avenilza e Fernando por absolutamente tudo, seu amor, por acreditarem e incentivarem em todas etapas até aqui, amo vocês.

Agradeço ao meu irmão Taffarel, pela irmandade e companheirismo.

À orientadora Profa. Dra. Adriana Maria Coimbra Horbe, pelos anos de parceria, respeito, conselhos e incentivos, sem você este trabalho não seria possível.

A minha companheira Nathana, pela paciência, lealdade, companheirismo e amor.

À Universidade de Brasília pela infraestrutura.

À CAPES e ao CNPq pelo apoio financeiro. O presente trabalho foi realizado com o apoio da Coordenação de Aperfeiçoamento de Pessoal de Nível Superior –Brasil (CAPES) – Código de Financiamento 001.

Aos meus tios Demétrio, Maria Menilza, Adailza, Aldineia, Agnaldo, Nira e Geraldo (In Memoriam).

Aos meus avós maternos Maria Rosa de Souza Tokuta e Satocy Tokuta e avós paternos Pedro Castro e Izabel Castro (In Memoriam).

Aos amigos do Laboratório de Raio-X da UnB: Caroline, Gabriel, Marcus Vinícius, Sanclever, Márcio, João Gabriel, Bárbara, Gustavo, Verônica e Rafael.

Aos amigos da pós-graduação da UnB.

Aos amigos da UFAM, em especial do DEGEO e da PPGGEO.

Ao Prof. Dr. Mauricio Parra como co-orientador deste trabalho, por compartilhar seu conhecimento, paciência e dedicação.

Ao Prof. Dr. Elton Luiz Dantas por fornecer as amostras para traços de fissão em apatita e contribuições.

Ao Prof. Dr. Peter Hackspacher (In Memoriam) pelo incentivo neste trabalho e abrir as portas dos laboratórios da UNESP.

Aos técnicos da UNESP Marli Carina e Daniel Godoy pelo auxilio na preparação das amostras de apatita.

Aos geólogos Bruno Venâncio e Gustavo Soldado por auxiliar na preparação das amostras de apatita.

Aos amigos do laboratório de Termocronologia de Baixa Temperatura da USP: Daniel Souza, Daniel Hernandez, Ana, Marlene, Sebastian e Laura.

Ao Prof. Dr. Luis Cherem pelas contribuições no primeiro artigo deste trabalho.

Aos amigos da minha querida cidade natal Parintins-AM.

Aos amigos da querida cidade Manaus-AM.

Aos amigos Netão Cardoso, Eduardo, Pedro Gaia, Evandro Picanço, Flávio Portilho, Tancredo de Castro, Fernando Junior, Gilmar Pontes, Eval Inomata e Harlinson Barbosa por sua amizade e incentivo.

Às amigas Fabiane Gonçalves, Telma Feijó, Rosicleide Anselmo e Sandrelly Inomata por sua amizade, incentivo e orações.

Aos amigos Dr. Francisco Cardoso e Dr. Tiago Cardoso, que cuidaram da minha saúde e não mediram esforços em um momento delicado da vida.

Aos amigos do Coliving Evolution em São Paulo: Felipe, Gabriel, Geraldo e Larissa.

Aos amigos e geólogos da SESAI: João Tarelow Neto, Cícero Lopes, Giuliano Bernardi, Steffano Paz e Artur Miranda.

E a todos que de alguma forma contribuíram nas diversas etapas deste trabalho.

Epígrafe

Prefiro ser
Essa metamorfose ambulante
Eu prefiro ser
Essa metamorfose ambulante

Do que ter aquela velha opinião formada sobre tudo
Do que ter aquela velha opinião formada sobre tudo

Metamorfose ambulante – Raul Seixas

RESUMO

Aa Província Tocantins é um grande orógeno Neoproterozóico que resultou da colisão dos paleocontinentes Amazônico, São Francisco e Paranapanema durante o ciclo Brasiliiano/Pan Africano, como parte da amalgamação do Gondwana Ocidental. As deformações intracontinentais causam soerguimento de superfícies erosivas e são consequência de processos de desestabilização da litosfera em domínios cratônicos. A abertura do Oceano Atlântico influenciou processos a 2,000 km da costa com reflexos no regolito. O regolito do Centro-Oeste brasileiro é caracterizado por uma paisagem escalonada de planaltos, serras, chapadas, inselbergs, cânions e planícies aluviais que formam quatro superfícies morfoestratigráficas. A superfície 1 é sustentada por serras de quartzito e as superfícies 2 e 3 por crostas lateríticas ferruginosas. As crostas da superfície 2 são quartzo-hematíticas, endurecidas, colunares, rosa-avermelhadas a vermelho-amareladas, possuem texturas protonodulares, brechóide e pisolíticas e alcançam até 3 m de espessura, enquanto as crostas lateríticas ferruginosas da superfície 3 são mais friáveis, quartzo-goethíticas, colunares, vermelho-amareladas a amarelo-alaranjadas, apresentam textura vermiforme com matriz argilo-ferruginosa microagregada e bioturbada, alcançando até 2 m de espessura. A superfície 4 inclui as planícies aluviais inferiores. O objetivo deste estudo foi entender a formação dessas superfícies regolíticas, suas relações, o impacto da dinâmica laterítica e as influências continentais como agentes formadores/controladores da paisagem. A área foi estudada por meio de imagens SRTM, perfis de varredura e Índice de Concentração de Rugosidade, bem como controle de campo, texturas, mineralogia, análise geoquímica e traços de fissão em apatita. Essas técnicas permitiram contribuir na modelagem térmica da Província Tocantins e investigar episódios de resfriamento/aquecimento e a possível influência desses processos na evolução do regolito do Centro-Oeste brasileiro. A superfície 1 marca o evento regional de erosão, enquanto as superfícies 2 e 3 marcam dois episódios de ferruginização relacionados a lateritização e mudança climática sazonal seca a úmida. A superfície 4 esculpe as planícies. As características dessas superfícies sequenciais foram produzidas a partir do final do Paléogeno em complexo processo paisagístico modelado por um extenso regime erosivo resultante de movimentos tectônicos durante a evolução do Oceano Atlântico e

clima tropical. Os TFA identificaram dois modelos de resfriamento para a região que indicam taxas de erosão de $60\text{-}80 \text{ m Myr}^{-1}$ compatíveis com a formação de crostas lateríticas apenas nos últimos 20 Ma quando a taxa de erosão decresceu.

Palavras-chave: Regolito; Crostas lateríticas ferruginosas; Episódios lateríticos; Superfície paleointempérica; Traços de Fissão em Apatita.

ABSTRACT

The Tocantins Province is a large Neoproterozoic orogen that resulted from the collision of the Amazonian, São Francisco and Paranapanema paleocontinents during the Brasiliano/Pan African cycle, as part of the West Gondwana amalgamation. Intracontinental deformations cause the uplift of erosive surfaces and are a consequence of destabilization processes of the lithosphere in cratonic domains. The opening of the Atlantic Ocean influenced processes 2.000 km from the coast with reflections on the regolith. The regolith of the Brazilian Midwest is characterized by a stepwise landscape of highlands, mountains, plateaus, inselbergs, canyons, and alluvial plains that form four morphostratigraphic surfaces. Surface 1 is supported by quartzite saws and surfaces 2 and 3 by ferruginous lateritic crusts. The crusts of surface 2 are quartz-hematitic, hardened, columnar, reddish-pink to yellowish-red, have protonodular, breccia and pisolithic textures and reach up to 3 m in thickness, while the ferruginous lateritic crusts of surface 3 are more friable, quartz - goethitic, columnar, yellowish-red to orange-yellow, they have a vermiform texture with a microaggregated and bioturbated clay-ferruginous matrix, reaching up to 2 m in thickness. Surface 4 includes the lower floodplains. The objective of this study was to understand the formation of these regolith surfaces, their relationships, the impact of lateritic dynamics and continental influences as forming/controlling agents of the landscape. The area was studied using SRTM images, scan profiles and Roughness Concentration Index, as well as field control, textures, mineralogy, geochemical analysis and fission traces in apatite. These techniques allowed contributing to the thermal modeling of the Tocantins Province and investigating cooling/heating episodes and the possible influence of these processes on the evolution of regolith in the Brazilian Midwest. Surface 1 marks the regional erosion event, while surfaces 2 and 3 mark two ferruginization episodes related to lateritization and seasonal dry to wet climate change. Surface 4 carves the plains. The characteristics of these sequential surfaces were produced from the end of the Paleogene in a complex landscape process modelled by an extensive erosion regime resulting from tectonic movements during the evolution of the Atlantic Ocean and tropical climate. The TFA identified two cooling models for the region that indicate erosion rates of 60-80 m Myr⁻¹ compatible with the formation of lateritic

duricrusts only in the last 20 Ma when the erosion rate decreased in consequence of final cooling.

Keywords: Regolith; Ferruginous lateritic duricrust; Lateritic episodes; Palaeoweathering surface; Apatite Fission Tracks

LISTA DE ILUSTRAÇÕES

Figura 1.1	Mapa de localização da área estudo	04
Figura 2.1	Mapa geológico simplificado da área estudo, com todas as amostras de crostas e rochas, amostras com análises químicas, traços de fissão em apatita e compiladas.	06
Figura 3.1	Diagrama esquemático da ocorrência de traços de fissão em um cristal de apatita	14
Figura 3.2	Fluxograma de etapas de preparação das amostras para traços de fissão em apatita.	18
Figura 3.3	Preparação das amostras e montagem para contagem	19
Figura 3.4	Traços de fissão de amostras do norte da Faixa Brasília	19
Figura 4.1	Simplified geological map of the studied area and sampling locations.	23
Figura 4.2	Lateritic regolith of the study area.	24
Figura 4.3	The swath profiles with approximately 100 km EW wide and 800 km NS long.	25
Figura 4.4	The lateritic profiles of study area	26
Figura 4.5	Distinct ferruginous lateritic duricrusts in the study area.	27
Figura 4.6	X-ray diffractograms of the lateritic duricrusts of the study area, samples and most common minerals at duricrust identified by XRD.	28
Figura 4.7	Ternary diagram $\text{SiO}_2 - \text{Al}_2\text{O}_3 - \text{Fe}_2\text{O}_3$ showing the classification of the ferruginous lateritic duricrusts according to Schellmann (1983).	29
Figura 4.8	Regional main topographic features and weathering surfaces of the study area.	31
Figura 5.1	Simplified geological map of the studied area and sampling locations.	52
Figura 5.2	Sample preparation of apatite fission track and counting on microscope.	53
Figura 5.3	AFT data and thermal history models	54
Figura 5.4	Test thermal history models	55

LISTA DE TABELAS

Tabela 3.1	Amostras de crosta dura laterítica analisadas com base no posicionamento do relevo e na unidade geomorfológica	12
Tabela 3.2	Ataques químicos comumente utilizados segundo o tipo de mineral	15
Tabela 3.3	Determinação da calibração zeta, a partir de amostras padrões de apatitas Durango e Fish Canyon Tuff.	16
Tabela 4.1	Distribution of major elements (%) and wt of lateritic duricrusts in the study area.	29
Tabela 5.1	Basement apatite fission track analysis results of northern of Brasilia Belt	56
Tabela 5.2	FT data for the Tocantins Province	57
Tabela 6.1	Chemical composition values express as wt %	63
Tabela 6.2	Chemical composition values express as ppm	65
Tabela 6.3	REE values express as ppm	67

SUMÁRIO

1 INTRODUÇÃO.....	2
1.1 <i>Localização e acesso.....</i>	4
2 REVISÃO BIBLIOGRÁFICA: ÁREA DE ESTUDO, CARACTERÍSTICAS GEOLÓGICAS E GEOMORFOLÓGICAS	6
2.1 <i>Geologia.....</i>	6
2.2 <i>Geomorfologia.....</i>	8
3 MATERIAIS E MÉTODOS.....	11
3.1 <i>Mineralogia e geoquímica</i>	11
3.2 <i>Modelo Digital de Elevação do regolito.....</i>	11
3.3 <i>Traços de fissão em apatita.....</i>	13
3.3.1 <i>Determinação da idade do TF</i>	15
3.3.2 <i>Preparação de amostras</i>	16
4 ARTIGO 1: THE BRAZILIAN MIDWEST LATERITIC DOMAINS: REGOLITH FEATURES AND DYNAMIC	21
5 CENOZOIC EVOLUTION OF CRATONIC REGOLITH: INSIGHTS FROM THERMOCHRONOLOGICAL APATITE FISSION TRACK PERSPECTIVE.....	36
1. INTRODUCTION	36
2. GEOLOGICAL SETTING OF TOCANTINS PROVINCE	37
3. THERMOCHRONOLOGY DATA IN TOCANTINS PROVINCE.....	39
4. MATERIAL AND METHODS	40
5. RESULTS	43
6. DISCUSSION.....	43
7. CONCLUSIONS	45
8. REFERENCES	45

FIGURE CAPTIONS	52
6 MINERALOGY AND GEOCHEMISTRY OF REGOLITH IN THE BRAZILIAN MIDWEST LATERITIC DOMAINS – ESBOÇO	59
1. INTRODUCTION	59
2. GEOLOGICAL SETTING OF TOCANTINS PROVINCE	60
7 CONSIDERAÇÕES FINAIS E SUGESTÕES PARA ESTUDOS FUTUROS	71
7.1 <i>Conclusões.....</i>	71
7.2 <i>Participação em artigos científicos</i>	72
7.3 <i>Sugestões para estudos futuros.....</i>	73
8 ANEXOS - DADOS DA CONTAGEM DE TRAÇOS DE FISSÃO EM APATITA.....	1

CAPÍTULO 1

INTRODUÇÃO

1 INTRODUÇÃO

Na modelagem de separações intracontinentais, o reequilíbrio do interior continental e reacomodações de blocos litosféricos, aliados ao gradiente geotérmico da litosfera, anomalias sísmicas e intrusões magmáticas (Davis e Kusznir, 2004; Kusznir e Karner, 2007; Brito Neves et al., 2014; Flament et al., 2013 e 2015; Fuck et al., 2017; Louterbach et al., 2017; Hu et al. 2018), pode elevar a crosta continental em 0,1 a 1 km (Magee et al. , 2017) com impacto direto nas feições do relevo (Ribeiro et al., 2018).

No limite leste da América do Sul, a separação com a África provocou a formação das serras da Mantiqueira e do Mar, intenso magmatismo alcalino e a discordância erosiva na Bacia Potiguar e na Província Borborema (Morais Neto et al., 2009; Oliveira et al., 2016.; Ribeiro et al., 2018 entre outros). No limite oeste, houve soerguimento andino e formações de várias bacias tipo foreland (por exemplo, Roddaz et al., 2005; Hoorn et al., 2010; Assine et al., 2016). Da mesma forma, na África, houve elevação, magmatismo e subsidência (Catuneanu et al., 2005; Hanson et al., 2009; Stanley et al., 2013; Guillocheau et al., 2017; Ye et al., 2017). Todos esses fatores que causam erosão, dissecação e reorganização hidrográfica, têm influência direta nas feições do regolito continental criando feições geológicas, geomorfológicas e pedológicas complexas (por exemplo, Büdel 1982, Summerfield 1991, Saadi, 1993 e Saadi et al., 2005, Beauvais et al., 2008; Beauvais e Chardon, 2013; Batezelli et al., 2016; Ribeiro et al., 2018, Chardon et al., 2018, Côrrea e Monteiro, 2021; Peulvast e Bétard, 2021).

Na Plataforma Sul-Americana brasileira, foram identificadas cinco paleosuperfícies regolíticas: Superfície Gondwana (Triássica), Superfície Pós-Gondwana (Cretáceo), Superfície Sul-Americana (Paleoceno), Superfície Velhas (Plioceno) e Superfície Paraguaçu (Quaternária) (De Martonne, 1943; Freitas, 1951; King, 1953 e 1956; Bigarella et al., 1965; Salgado, 2007; Valadão, 2009) formando relevo em escadarias. As Superfícies da América do Sul e Velhas na Amazônia estão lateritizadas e existem grandes depósitos de bauxita (depósitos de Paragominas, Juruti, Trombetas e Almerim) derivados principalmente de rochas siliciclásticas (por exemplo, Bardossy e Aleva, 1990; Boulangé e Carvalho, 1997; Lucas, 1997; Kotschoubey et al., 2005; Costa, 1997; Oliveira et al., 2016). Também há vários pequenos depósitos de bauxita ao longo da costa atlântica na Serra da Mantiqueira, (Poços de Caldas, Miraí entre outros) e Quadrilatero Ferrífero, todos derivados de rochas ígneas e metamórficas (Valeton et al., 1991, Melfi, 1997; Oliveira e Toledo 1997, Leonardi et al. 2011 e suas referências) Entretanto, a maioria dessas bauxitas fora da Amazônia, tem gênese hidrotermal (Valeton et al., 1991, Leonardi 2011, Moura 2019).

As idades Ar-Ar e U-Th/He das superfícies lateríticas (Vasconcelos et al., 1994; Ruffet et al., 1996; Costa et al. al., 2005; Shuster et al., 2005; Lima 2008, Monteiro et al., 2014; Monteiro et al., 2018a e b; Vasconcelos e Carmo, 2018; dos Santos Albuquerque et al., 2020, Heller et al. 2022), estão de acordo com

os vários episódios de formação laterítica na África, Índia, China e Austrália (Hénocque et al., 1998; Dammer et al., 1999; Vasconcelos, 1999; Pidgeon et al., 2004; Colin et al., 2005; Spier et al., 2006; Beauvais et al., 2008; Beauvais e Chardon, 2013, Bonnet et al., 2014 e 2016; Deng et al., 2016; Mathian et al., 2019; Wells et al., 2019; Jean et al., 2020). Os episódios mais antigos são datados do Cretáceo Superior, pré-África e descolamento da América do Sul, e os picos de formação da maioria dos depósitos de bauxita estão no Paleoceno-Oligocene (~60–50 Ma, ~45–40 Ma, ~30 Ma), com sucessivos episódios ferruginosos mais jovens no Mioceno Médio ao Plioceno (18–10 Ma, 7,2–5,8 Ma e 3,4–2,9 Ma).

As bauxitas e as crostas ferruginosas sustentam superfícies deplainamento e são formadas episodicamente em algumas áreas e continuamente em outras sob repetidas pedimentações áridas ou semiáridas e intemperismo tropical sazonal (por exemplo, Bardossy e Aleva, 1990, Tardy e Roquin 1998; Burke e Gunnell, 2008; Retallack, 2010; Beauvais e Chardon, 2013; Grimaud et al., 2015). As bauxitas estão principalmente relacionadas a períodos úmidos, necessitam de mudanças climáticas de longo prazo e são do Paleógeno, enquanto as crostas ferruginosas, geralmente mais jovens e relacionadas a clima mais sazonal, são do Neógeno. Essa relação entre composição e idade identificada na América do Sul (por exemplo, Costa 1997, Kostschoubey et al. 2005) é uma característica importante e útil para estabelecer a cronologia das superfícies.

O Planalto Central brasileiro pertence ao megacompartimento geomorfológico do Atlântico Brasil (Saadi et al., 2005; Salgado et al., 2015). É composto por áreas de serras, montanhas, chapadas, tabuleiros, inselbergs, cânions e áreas de geoformas dissecadas rebaixadas esculpidas pelas três principais bacias hidrográficas brasileiras (Paraná, São Francisco e Amazonas) (por exemplo, Braun, 1971; Mamede et al., 1981a e b; Nascimento, 1991; Moreira, 1995; Martins e Baptista, 1999). Nessa região, afloram rochas arqueanas a paleozóicas e, diferentemente das bauxitas lateríticas bem desenvolvidas e preservadas da região amazônica, ocorrem apenas crostas lateríticas ferruginosas (Martins et al., 2004, Latrubblesse e Carvalho, 2006, Moraes, 2014; Ribeiro, 2017; Souza et al. 2021 e Peixoto et al. 2021) apesar de prevalecer condição climática favorável à formação de bauxita (Price et al. 1997).

Uma vez que as crostas lateríticas e suas características como altitude, composição mineral e química são usadas para estabelecer o desenvolvimento da paisagem regolítica, dando idades relativas e absolutas (Ollier e Pain, 1996; Costa 1997, Beauvais et al., 2008; Beauvais e Chardon, 2013; Vasconcelos e Carmo, 2018), foi selecionada uma área no Centro-Oeste brasileiro (norte de Goiás e sul do Tocantins Fig. 1), com complexo cenário geológico, geomorfológico e pedológico. O objetivo foi compreender o cenário, a formação das superfícies regolíticas, a relação entre as superfícies e identificar processos geotectônicos/ geodinâmicos que possam controlar a dinâmica

laterítica. A área foi estudada com imagens SRTM, perfis de varredura e Índice de Concentração de Rugosidade, texturas, mineralogia, geoquímica e traços de fissão em apatita associados a controle de trabalho de campo.

1.1 Localização e acesso

A área do presente estudo, com cerca de 555.540,00 Km², localiza-se no norte do Centro Oeste do Brasil e o sul do estado do Tocantins, é delimitada por um polígono que compreende as coordenadas 10°S/46°W, 10°S/51°W, 19°S/46°W e 19°S/51°W. O acesso, a partir de Brasília foi realizado todo via terrestre, principalmente pelas rodovias BR-010, BR-020, BR-040, BR-060, além das rodovias federais, estaduais e vicinais adjacentes para estudar a região.

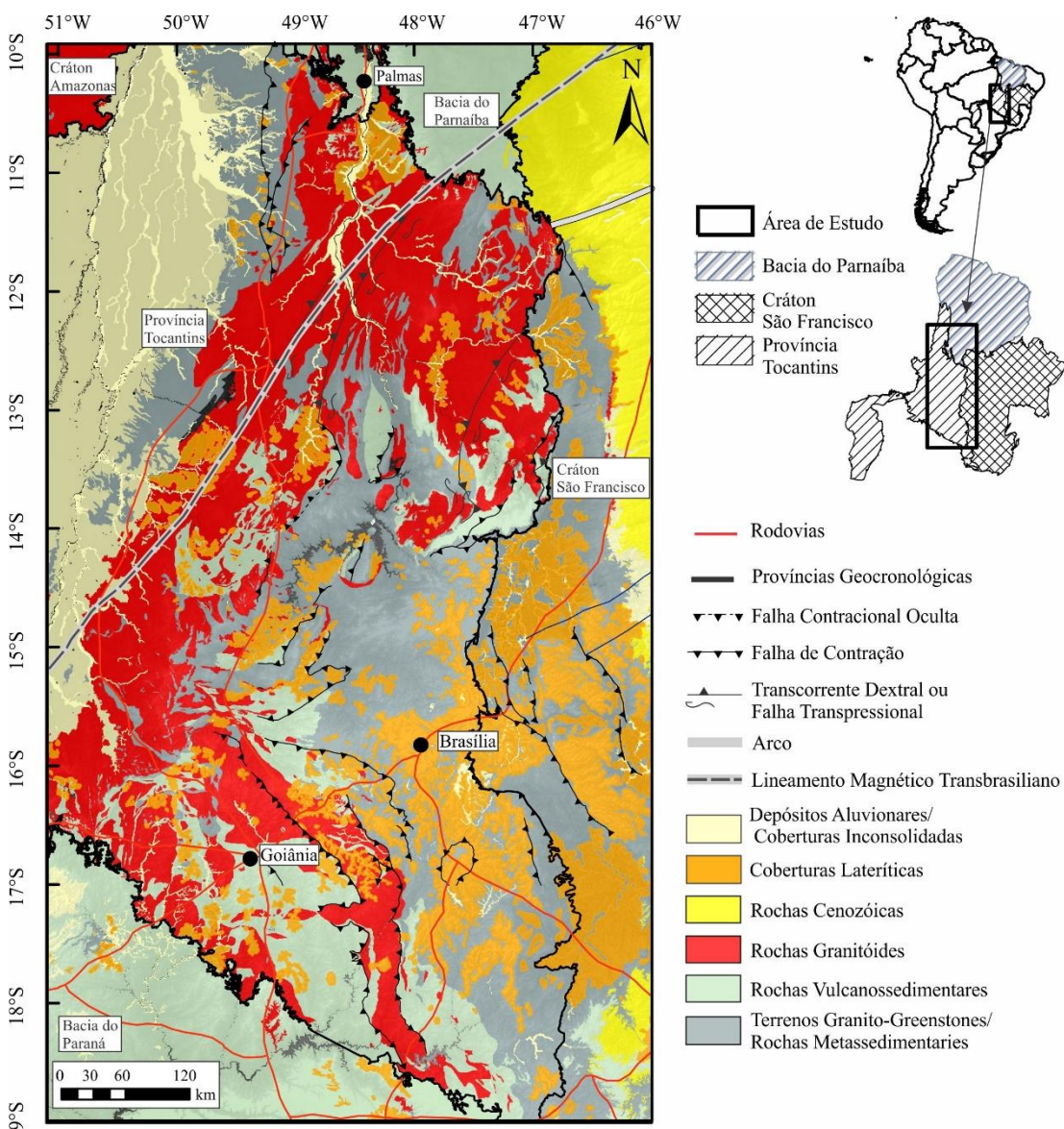


Figura 1.1: Mapa de localização da área estudo.

CAPÍTULO 2

REVISÃO BIBLIOGRÁFICA: ÁREA DE ESTUDO, CARACTERÍSTICAS GEOLÓGICAS E GEOMORFOLÓGICAS

2 REVISÃO BIBLIOGRÁFICA: ÁREA DE ESTUDO, CARACTERÍSTICAS GEOLÓGICAS E GEOMORFOLÓGICAS

2.1 Geologia

A Província Tocantins (Almeida et al., 1981) é um extenso orógeno Brasiliano/Pan-Africano da Plataforma Sul-Americana formado pela colisão entre os crátons Amazônico, São Francisco/Congo, Oeste Africano/São Luís e Paranapanema que resultou na amalgamação do supercontinente Gondwana Ocidental no Neoproterozóico (orogenia Brasiliana) (Figura 1).

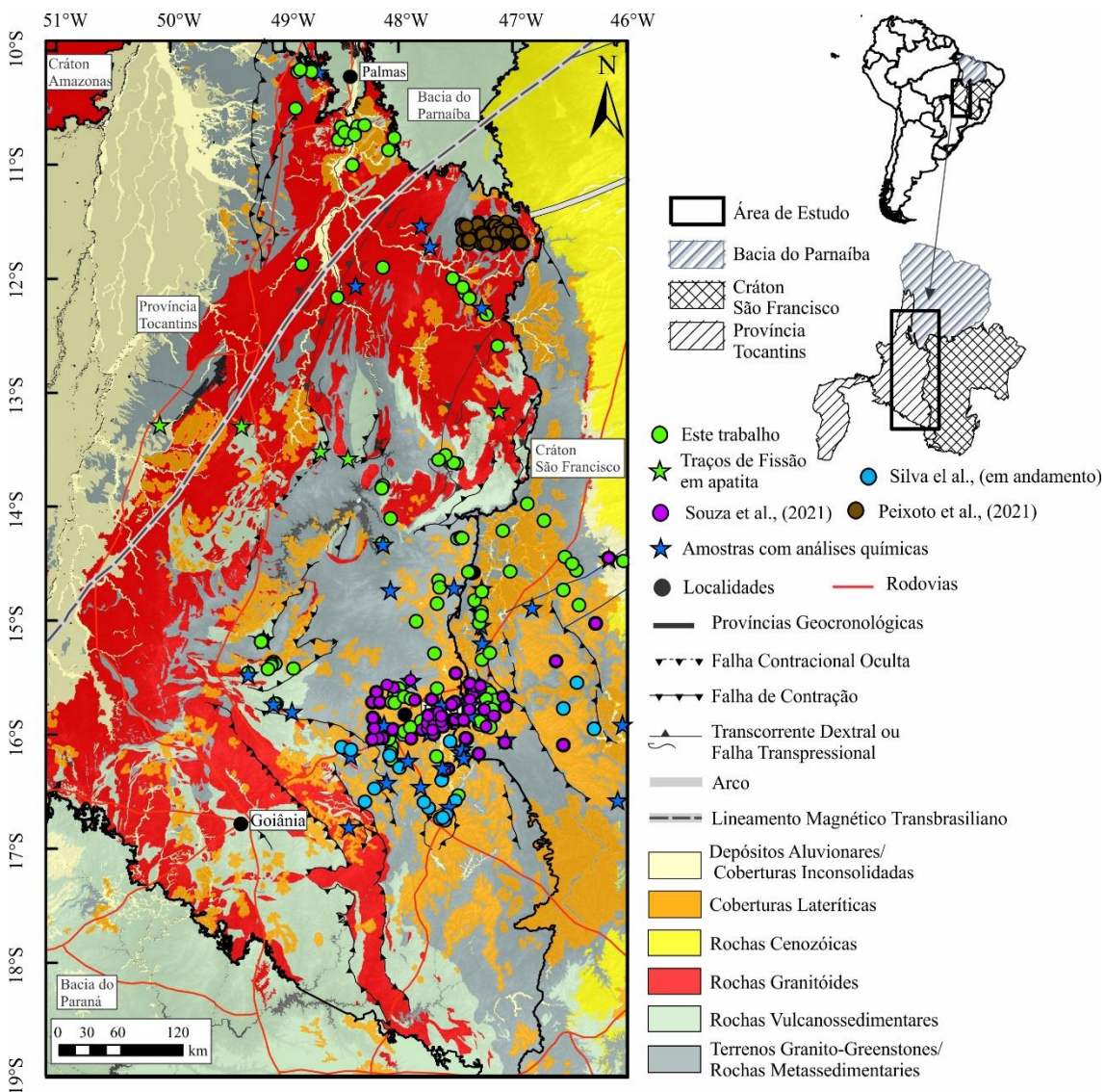


Figura 2: Mapa geológico simplificado da área estudo, com todas as amostras de crostas e rochas, amostras com análises químicas, traços de fissão em apatita e compiladas.

A província é composta por três faixas neoproterozóicas: as faixas Paraguai, Araguaia e Brasília (Pimentel et al., 2000), neste trabalho são encontradas apenas rochas das faixas Araguaia e Brasília. A área é cortada pelo Lineamento Transbrasiliano (LTB), uma das principais descontinuidades litosféricas da região, que define o limite de diferentes domínios crustais (Cordani e Sato, 1999; Cordani et al., 2013; Brito Neves e Fuck, 2014).

A Faixa Araguaia compreende as partes central e norte da Província Tocantins. Ao longo de seu limite leste, a faixa é coberta por rochas sedimentares da bacia do Parnaíba (Paleozóico-Mesozóico). Esta bacia abrange um bloco litosférico, que provavelmente representa seu núcleo cratônico (Brito Neves et al., 1984; Góes et al., 1993; Nunes, 1993; Brito Neves, 1998; Castro et al., 2014; Daly et al., 2014). Na porção oeste por granitóides do Cráton Amazônico. A sudeste, a faixa é delimitada pelo Maciço Goiás.

A faixa Brasília é delimitada com a margem oeste do Cráton do São Francisco e é um dos orógenos brasileiros preservados da Plataforma Sul-Americana. Esta faixa tem uma forma alongada na direção norte-sul, estendendo-se por mais de 1000 km na porção centro-norte do Brasil (Dardenne, 2000; Fuck et al., 2014; Pimentel, 2016). A Faixa Brasília é formada por Zona Externa, Margem Passiva, Zona Interna e Arco Magmático Goiás, (Pimentel e Fuck, 1992, 1994; Pimentel et al., 2000a, 2000b; Valeriano et al., 2008; Fuck et al., 2014, 2017; Pimentel, 2016; Cordeiro e Oliveira, 2017; Cuadros et al., 2017a).

A Zona Externa compreende o embasamento formado por rochas metassedimentares da Formação Ticunzal, os granitos das suítes Aurumina e Pedra Branca (Alvarenga et al., 2007; Tanizaki et al., 2015; Cuadros et al., 2017b), Grupos Araí, Paranoá e Bambuí (Fuck et al., 2014; Pimentel, 2016). Essas rochas recobrem as unidades do embasamento, cobrindo uma área de aproximadamente 10.000 km² no nordeste de Goiás e sudeste do Tocantins (Dardenne, 2000; Alvarenga et al., 2007; Pimentel, 2016; Tanizaki et al., 2015; Cordeiro e Oliveira, 2017; Martins-Ferreira et al., 2018).

A Margem Passiva é formada por rochas metassedimentares dos Grupos Vazante, Paranoá, Canastra, Andrelândia e Ibiá (Fuck et al., 2014; Pimentel, 2016; Pimentel et al., 2004; Valeriano et al., 2004, 2008). A Zona Interna compreende o Núcleo Metamórfico e o Maciço Goiás (Fuck et al., 2014; Pimentel, 2016). O núcleo metamórfico compreende as rochas metassedimentares Neoproterozóicas do Grupo Araxá e as rochas de alto grau do Complexo Anápolis-Itauçu e o maciço Goiás inclui terrenos arqueanos graníticos e ortognaisses Paleoproterozóicos, cobertos pelo Grupo Paleoproterozóico Serra da Mesa (Fuck et al., 2017). O Arco Magmático Goiás compreende terrenos ortognaisses Neoproterozóicos e sequências vulcânicas-sedimentares (Fuck et al., 2017) é dividido em Arcos Magmáticos Mara Rosa (norte) e Arenópolis (sul-sudeste) (Cordeiro e Oliveira, 2017; Fuck et al., 2008, 2014; Laux et al., 2005; Pimentel e Fuck, 1994; Pimentel et al., 2000a, 2000b; 2004; Pimentel, 2016; Valeriano et al., 2008).

As rochas sedimentares Fanerozóicas das bacias do Parnaíba e do Paraná cobrem a província ao norte e ao sul, respectivamente, essas bacias também cobrem blocos continentais estáveis mais antigos, como os chamados blocos Parnaíba e Paranapanema (Fuck et al., 2014, 2017). O magmatismo alcalino Pós-Paleozóico intrudiu o embasamento da província principalmente em áreas ao redor da bacia do Paraná e da faixa Brasília, três bacias intracratônicas

muito semelhantes foram desenvolvidas no Cretáceo: as bacias Sanfranciscana, Parecis e Bauru. A faixa Brasília hospedou vários pulsos magmáticos alcalinos entre o final do Cretáceo e o Paleógeno (Riccomini et al. 2005). A bacia Sanfranciscana desenvolveu-se sobre o Cráton São Francisco e apresenta a seguinte estratigrafia mesozóica: sequência flúvio-lacustre do Cretáceo Inferior (Grupo Areado) e sequências do Cretáceo Superior depositadas no sistema eólico (Grupo Urucuia), leques aluviais (Formação Capacete, Mata da Corda Grupo) e vulcânica alcalina (Formação Patos, grupo Mata da Corda) (Campos e Dardenne 1997a, b). As coberturas continentais cretáceas e cenozóicas, destacando-se o Pantanal, a planície do Araguaia (Almeida et al. 1981) e a bacia Sanfranciscana são pulsos de sedimentação mais jovens (Campos e Dardenne, 1997 a, b; Uhlein et al., 2011).

2.2 Geomorfologia

As geoformas dissecadas de serras, montanhas, chapadas, tabuleiros, inselbergs, cânions e planícies são agrupadas em quatro unidades geomorfológicas: Planalto Central Goiano (CGH) na região Centro-Oeste, Divisor Planalto São Francisco-Tocantins (DSFTH) na região leste e Tocantins Depressão e Planalto Residual do Tocantins (TDRH) na região norte e noroeste (Mamede et al., 1981a; Nascimento, 1991).

O CGH apresenta a maior variedade de formas, litologias e altitudes (Braun, 1971; Nascimento, 1991; Moreira, 1995) que formam três estruturas geomorfológicas: 120 km na direção SW-NE e 130 km na direção NNW-SSE. É 350 a 1650 m m.s.l. alto na parte central e é fortemente controlada por falhas e dobras esculpidas em vales, montanhas e planaltos, nos metassedimentares principalmente quartzitos (Grupos Araí, Paranoá e Bambuí) e rochas graníticas Proterozóicas (Suítes Aurumina e Pedra Branca, Figs. 2 e 3); B) planaltos altos (Alto Tocantins-Planalto Paranaíba) na parte central sudoeste, são 1000 e 1200 m a.n.m. e é formado por serras e planaltos alongados também nas rochas metassedimentares proterozóicas (grupos Araí, Paranoá e Bambuí) e complexos máfico-ultramáficos (Canabrava, Niquelândia e Barro Alto; (Colin et al., 1990; Nascimento, 1991; Oliveira et al., 2011; Moraes, 2014) emergem; C) um planalto baixo (Planalto do Distrito Federal) entre 500 e 1240 m a.n.m. localizada ao sul da área de estudo, possui formas planas levemente onduladas e dissecadas, esculpidas nos grupos metassedimentares Paranoá e Bambuí.

O DSFTH ou Serra Geral de Goiás, no lado leste da área de estudo, compreende planaltos de 500 a 1200 m a.n.m. desenvolvido nas rochas sedimentares do Cretáceo (Grupo Urucuia). A Depressão Tocantins (TD) na parte centro-norte é uma grande planície que separa a serra do CGH do DSFTH (Fig. 2). Esta área em 200 a 600 m a.n.m. nas rochas metassedimentares (Grupos Araí, Paranoá e Bambuí), foram esculpidas pelo rio Tocantins (Mamede et al., 1981a; Nascimento, 1991; Moreira, 1995; Costa et al., 2010). O RTH ao norte com 500 a 900 m a.n.m. e grandes escarpas, é formado por serras de 12 a 60 km de extensão sustentadas por rochas do

embasamento (Província do Tocantins) e rochas sedimentares (Bacia do Parnaíba; Mamede et al., 1981b; Costa et al., 2010). Os rios Corumbá e São Francisco cortam as partes sul e leste da área de estudo.

CAPÍTULO 3

LOCALIZAÇÃO E ACESSO, MATERIAIS E MÉTODOS

3 MATERIAIS E MÉTODOS

3.1 Mineralogia e geoquímica

Para estudar a evolução do domínio laterítico do Centro-Oeste do Brasil e suas características foram coletadas 112 amostras de rochas e crostas lateríticas. Metade dessas amostras foram usadas para desenvolver técnicas matemáticas nos mapeamentos realizados por Peixoto et al. (2021), Souza et al. (2021), e Silva et al. (em preparação).

Vinte das 56 amostras de crostas lateríticas coletadas neste estudo foram analisadas quanto à composição mineral e química, estas amostras foram coletadas de acordo com a rocha mãe e o posicionamento no relevo (Tabela 1) uma alíquota foi pulverizada para análises mineralógicas e químicas. As outras 36 amostras foram análises minerais e químicas realizadas por Peixoto et al. (2021), Souza et al. (2021), e Silva et al. (em preparação). A identificação mineral das vinte amostras foi feita por difração de raios X (RIGAKU ULTIMA IV) com tubo de Cu na Universidade de Brasília com faixa de leitura de 5° a 60° 2 Θ .

As concentrações dos elementos maiores e menores (SiO_2 , Al_2O_3 , Fe_2O_3 , CaO , MgO , Na_2O , K_2O , TiO_2 e P_2O_5) foram determinadas por ICP-AES após fusão com LiBO_2 e digestão em água régia. A perda ao fogo (PF) foi feita aquecendo as amostras à 1000°C. Essas análises químicas foram realizadas na ALS Corplab, Brasil.

3.2 Modelo Digital de Elevação do regolito

A partir das análises cartográficas e melhor identificação das geoformas geológicas e dissecadas e a relação do regolito laterítico foi feito um modelo digital de elevação (MDE) usando 54 SRTM (Shuttle Radar Topography Mission) com resolução espacial de 90 m obtidas no USGS (<https://earthexplorer.usgs.gov/>) foi criado. A partir do MDE foram criados dois perfis topográficos de varredura (PTV), o primeiro com 100 km de largura na direção N-S (extensão de 780 km com 69.076 pontos cotados) e o segundo com direção L-W (extensão de 380 km com 26.155 pontos cotados), foram gerados no ArcGIS 10.6® software usando o método automático de Silva e Silva (2018). Os PTV que utilizam um modelo digital de elevação (DEM) permitem uma visão mais refinada e completa do relevo e reconhecimento topográfico de declives do que os tradicionais topográficos feitos ao longo de uma linha (Bavil e Bavil, 2019; Jaiswara et al., 2020; Bertolini et al., 2021; Fonseca et al., 2021). Do MDE, o software extraiu cerca de 100.000 pontos topográficos. Nos dois perfis, cada ponto topográfico é representado por um único círculo preto, com a altitude do ponto plotada no eixo y e a posição geográfica plotada no eixo x.

Tabela 3.1: Amostras de crosta dura laterítica analisadas com base no posicionamento do relevo e na unidade geomorfológica.

Amostras	Altitude	Superfície	Amostras	Altitude	Superfície
1	1180	2	29	629	3
2	948	2	30	537	3
3	1028	2	31	450	3
4	994	2	32	501	3
5	785	2	33	523	3
6	814	2	34	445	3
7	944	2	35	517	3
8	938	2	36	309	3
9	971	2	37	382	3
10	1007	2	38	410	3
11	1081	2	39	360	3
12	1015	2	40	327	3
13	1059	2	41	535	3
14	982	2	42	309	3
15	1011	2	43	420	3
16	933	2	44	415	3
17	929	2	45	423	3
18	935	2	46	394	3
19	937	2	47	400	3
20	1006	2	48	352	3
21	1109	2	49	362	3
22	1117	2	50	367	3
23	970	2	51	377	3
24	1002	2	52	382	3
25	1071	2	53	412	3
26	754	2	54	380	3
27	748	2	55	395	3
28	793	2	56	651	3

O índice de concentração de rugosidade (ICR) foi calculado usando o mesmo software (Sampaio e Augustin, 2014). A função de inclinação do ArcGIS e a declividade espacial por unidade de área do MDE são usadas no cálculo. Esse procedimento resultou na criação de uma matriz na qual cada pixel armazena um valor único. A matriz foi transformada em um arquivo de pontos para a aplicação do estimador de densidade Kernel, que transforma os valores dos índices obtidos em dados espaciais. As seis classes (plana, suavemente ondulada, ondulada, fortemente ondulada, íngreme e fortemente inclinada) foram identificadas de acordo com a distribuição espacial e recorrência da declividade do talude (<1, 1-3, 3-6, 6-14, 14-20 e >20°) permitiu identificar as unidades gerais de relevo. O PTV e o ICR permitem a identificação de bandas de transição limiares, a escala de feições de relevo e a

descrição de feições de superfície regolítica; essas duas ferramentas foram utilizadas em escala regional (resolução de 90 m).

3.3 Traços de fissão em apatita

Dentro da geologia isotópica, o ramo da termocronologia de baixa temperatura se concentra na compreensão da história térmica da crosta superior, onde ocorrem os processos morfotectônicos, que podem ser usados para reconstruir histórias geológicas, com base no tempo e na taxa de aquecimento e resfriamento em temperaturas $\sim 50^{\circ}\text{C}$ a $\sim 320^{\circ}\text{C}$ (Chew and Spikings 2015; Tagami 2005). Os métodos de investigação mais consolidados e empregados incluem um conjunto de sistemas termocronométricos com análise de traço de fissão (TF) e a termocronometria (U-Th)/He em cristais de apatita.

O método dos Traços de fissão é baseado no acúmulo de trilhas estreitas de danos (ou seja, traços de fissão) em grãos minerais ricos em urânio (por exemplo, apatita, zircão, titanita) e vidros naturais, que se formam como resultado do decaimento espontâneo da fissão nuclear de ^{238}U , do qual o isótopo pai se divide em dois núcleos de alta energia carregados positivamente. (Price e Walker 1963; Fleischer et al. 1975). As partículas ionizadas pesadas viajam em alta velocidade através do sólido isolante (detector) e moldam um canal danificado amorfo. Esses defeitos na rede cristalina são os traços de fissão, e cada um representa um evento de decaimento de fissão.

O tempo decorrido desde que os traços de fissão começaram a se acumular é estimado pela determinação da densidade dos traços acumulados em um determinado material em relação ao teor de urânio desse material. Após o polimento e o ataque químico permite aumentar a zona danificada na estrutura cristalina do mineral, causada pela passagem de uma partícula ionizante, de sorte que se possa observar os traços de fissão em microscopia óptica. (Price e Walker 1962).

Na apatita, os TF recém-formados têm um comprimento total de aproximadamente 16 μm (Figura 3.1) e encurtam progressivamente em certos intervalos de temperatura como resposta à cura do dano cristalográfico em um processo chamado *annealing* (Wagner e Van den Haute, 1992). Os traços de fissão são totalmente apagados quando o mineral é submetido a altas temperaturas; enquanto em temperaturas menores, os traços são encurtados lentamente com o tempo (Green, 1988; Brown et al., 1990). Para escalas de tempo geológicas (10^6 – 10^8 anos), uma faixa de temperatura na qual tais fenômenos ocorrem é denominada Zona Parcial de Apagamento (*Partial Annealing Zone - PAZ*). Para apatita, experimentos de *annealing* estimam que o *PAZ* está entre ~ 110 - 60°C (Laslett et al., 1987). Em temperaturas mais baixas, o efeito de apagamento torna-se menos eficaz e os traços são em sua maioria preservados. Assim, os traços de fissão registram a passagem do mineral pela *PAZ* e o tempo de residência nesta vai influenciar na quantidade

observável e na distribuição de comprimento dos traços. Essas informações são usadas para modelar a história termal dos minerais e a evolução da paisagem e suas relações relacionadas ao resfriamento, soerguimento e exumação (Ketcham, 2005; Gallagher, 2012; Malusà e Fitzgerald, 2018).

O número de átomos de ^{238}U é medido por meio da quantidade de ^{235}U , que mantém uma relação com o ^{238}U , ou seja, é a razão ou abundância natural entre o ^{238}U e ^{235}U .

As duas concentrações de urânio, o ^{238}U e o ^{235}U . Ao induzir o ^{235}U em reator nuclear, obtem-se a quantidade de ^{235}U e antes da irradiação são revelados os traços fósseis de ^{238}U que fornece essa grandeza. Assim temos as duas concentrações necessárias para uma datação isotópica. Para isso a amostra é irradiada para a indução da fissão dos átomos de ^{235}U , cuja densidade de traços leva à quantidade deste isótopo, que permitirá determinar a quantidade de ^{238}U presente no mineral e a idade da passagem pela isoterma de 110°C e sua estabilidade térmica..

Segundo Wagner e Van den Haute (1992) devido ao tamanho dos TF ser de μm , a observação direta só é possível no microscópio de transmissão eletrônica (TEM), porém tratamento químico (*Chemical Etching*) com uma solução de HNO_3 na apatita e ou de $\text{KOH}:\text{NaOH}$ no zircão o TF é amplificado o que facilita a observação em microscópio óptico (Gleadow et al., 1976) (Tabela 1). Os traços que cortam a superfície exposta ao ataque das soluções são utilizados na contagem da quantidade de ^{238}U e os traços confinados paralelos à superfície do mineral, são utilizados para medida de comprimento. A média das medidas é importante para os dados estatísticos dos traços de fissão, pois a variação de tamanhos é consequência das diferentes temperaturas a que o mineral foi submetido.

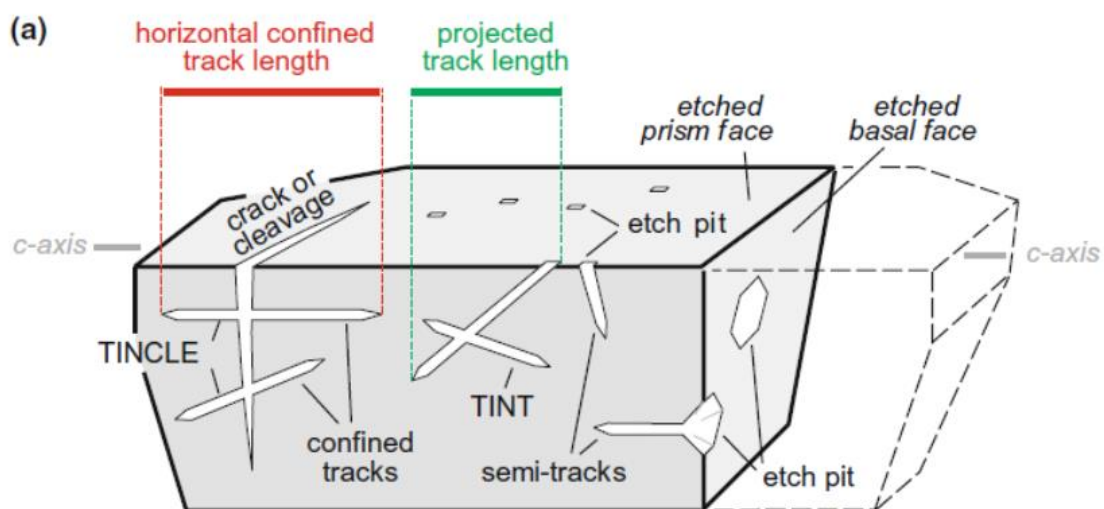


Figura 3.1: Diagrama esquemático comparando traços semi e confinados em um cristal de apatita. TINCLE é um traço confinado que cruza uma fratura ou clivagem; TINT é um traço confinado que cruza um traço de superfície (Fonte: Hurford, 2019).

Tabela 3.2: Ataques químicos comumente utilizados segundo o tipo de mineral.

Mineral	Ataque químico	Condições
Apatita	5 N HNO ₃ (Gleadow and Lovering 1978)	20 ± 1 °C, 20 s
	5.5 N HNO ₃ (Carlson et al., 1999; Donelick et al., 2005)	21 ± 1 °C, 20 ± 0.5 s
Zircão	Mistura de KOH:NaOH (em proporções por peso: 8.0 g KOH e 11.2 g NaOH - Gleadow et al. 1976)	225–230 °C 4–120 h (ou mais)
	Uma variante do eutético é NaOH:KOH:LiOH (6:14:1) que aumenta a eficiência do ataque a temperaturas de ataque mais baixas para tempos de ataque comparáveis (Zaun e Wagner, 1985)	
	Outras possibilidades: Garver (2003); Tagami e O'Sullivan, 2005)	

3.3.1 Determinação da idade do TF

A determinação da idade do TF obedece aos princípios de outros métodos geocronológicos baseados no decaimento natural de átomos-pai para átomos-filho. O método fundamenta-se na equação que rege o decaimento radioativo, cuja integração permite que se descreva a acumulação de TF. Estes parâmetros são obtidos indiretamente por meio da medida de densidade de TF. A idade é obtida utilizando-se a calibração zeta e absoluta, tanto as datações com uso da calibração zeta quanto a aquelas por calibração absoluta exigem irradiação em reator nuclear. Ambas exigem o uso de dosímetros de vidro, para a datação absoluta pode ser fios finos metálicos. No caso da calibração zeta é necessário também utilizar um padrão geológico, normalmente apatitas durango ou Fish Canyon para determinação do fator zeta (Tabela 3.2), que dependerá dos dosímetros utilizados.(Wagner e Van den Haute, 1992). Os dados utilizados na equação da idade são obtidos após a análise ao microscópio da densidade dos TF espontâneos (ρ_S) e dos induzidos (ρ_I). A densidade ρ_S está relacionada com o número de átomos de urânio ^{238}U e outros parâmetros na equação 1:

$$\rho_S = \varepsilon^{238} \cdot N_U \cdot C_{238} \cdot \frac{\lambda_F}{\lambda} \cdot [\exp.(\lambda \cdot T) - 1], \quad (1)$$

onde ε^{238} é um fator de detecção, que representa a razão entre o número de traços de fissão do ^{238}U , observados por unidade de superfície e o número de fissões espontâneas ocorridas no mineral, por unidade de volume; N_U é o número de átomos de urânio por unidade de volume presente no mineral; C_{238} é a concentração isotópica do ^{238}U no urânio natural; λ_F é a constante de decaimento por fissão espontânea do ^{238}U ; e λ é a constante de decaimento alfa do ^{238}U .

As causas geológicas capazes de influenciar a estabilidade dos TF nos minerais podem ser: tempo, temperatura, pressão, soluções intergranulares e radiações ionizantes (Fleischer e Hart, 1972; Gleadow e Lovering, 1978). Destes, a temperatura é a mais importante, pois é capaz de reordenar a estrutura do sólido que foi desordenada pela passagem de um fragmento de fissão (Gallagher; et al., 1998), ou seja, os átomos que foram deslocados com a formação dos TF podem retornar ao seu local de origem quando expostos a tratamento térmico. O *annealing* é o fenômeno que qualifica o método como a ferramenta termocronológica capaz de reconstruir eventos geológicos (Carter e Bristow, 2000). Como a idade termocronológica é determinada pela comparação da quantidade de TF e a temperatura afeta esta quantidade, a evolução da idade reflete a evolução da temperatura, ou seja, a datação destes minerais nos fornece a idade do último evento térmico que causou a geração e/ou apagamento dos TF (Wagner e Van den Haute, 1992; Tagami e O'Sullivan, 2005; Kohn; et al., 2019)

A potência do FT para investigações geológicas deriva precisamente de sua sensibilidade térmica, os métodos são únicos entre os termocronômetros, pois, após a formação, cada produto filho torna-se um registrador sensível da história térmica que seu mineral hospedeiro sofre (Ketcham, 2019). Se as informações de temperatura em um grande número de traços que se formaram durante um longo intervalo de tempo puderem ser recuperadas com sucesso, essas informações podem ser integradas e mescladas com outras restrições geológicas para verificar histórias térmicas detalhadas (por exemplo, Green et al. 1989; Gallagher 1995, 2012; Issler 1996; Ketcham 2005).

Tabela 3.3: Determinação da calibração zeta, a partir de amostras padrões de apatitas Durango e Fish Canyon Tuff.

Calculation of zeta						
	zeta		zeta+error	zeta-error		
Standard Sample	serial number	Samples	zeta		zeta+error	zeta-error
Durango	1	POA1-14A	98.74	6.43	105.17	92.31
Durango	2	POA1-14B	102.08	7.14	109.22	94.94
Durango	3	POA1-14C	107.79	7.25	115.04	100.54
Durango	4	POA1-14D	109.4	7.69	117.09	101.71
Fish Canyon Tuff	5	POA1-11A	98.77	6.09	104.86	92.68
Fish Canyon Tuff	6	POA1-11B	107.69	6.65	114.34	101.04
Fish Canyon Tuff	7	POA1-11C	91.31	5.63	96.94	85.68
Arithmetic			102.25	6.70		

3.3.2 Preparação de amostras

Os grãos de apatita foram separados por técnicas convencionais de Trituração, peneiramento, separador magnético e líquido pesado (Figura 3.2) no Laboratório de preparação de amostras pedológicas e geológicas, situado no Departamento de Petrologia e Metalogenia – Unesp – IGCE – Rio Claro – SP e

a separação manual e montagem em resina epóxi (Figura 3.2) no Laboratório de Catodo-Luminescência no Departamento de Petrologia e Metalogenia – Unesp – IGCE – Rio Claro – SP. Foram preparadas 23 amostras em resinas epóxi, as amostras são de gnaisses, granitos, metassedimentares e tonalito.

As resinas epóxi foram polidas e atacadas (Figura 3.3) usando 5,5 M HNO₃ a 21° C por 20 s para revelar traços de fissão espontâneos (Donelick et al. 2005) no Laboratório de Termocronologia de Baixa Temperatura do Instituto de Geociências da Universidade de São Paulo (IGc/USP), apenas 10 amostras revelaram traços de fissão.

Os *mounts* de apatita foram cobertos com folhas de micas para obter revelar traços de fissão usando o método de detector externo (Gleadow, 1981). A irradiação de nêutrons foi realizada no reator nuclear do IPEN/CNEN (São Paulo, Brasil), usando uma fluência de nêutrons de ~ 9,0 E15 n/cm². Após a irradiação, os detectores de mica foram atacados com 40% HF por 45 min para revelar traços de fissão induzidos (Figura 3.4).

A contagem de traços de fissão foi realizada em um microscópio Olympus SZX16 com ampliação de 1250x. As idades de traços de fissão foram calculadas usando a abordagem de calibração zeta (Hurford, 1983) com um vidro dosímetro CN1 e o padrão de idade Durango apatita. Pelo menos 22 grãos foram contados por amostra, exceto uma amostra com 6 grãos datáveis.

Pelo menos cem traços horizontais confinados foram medidos por amostra (Gleadow et al., 1986; Gallagher et al., 1998). A orientação dos traços em relação ao eixo c também foi medida, então usamos o comprimento médio projetado dos traços (MTL) para modelagem (por exemplo, Ketchman et al., 2009).

Idades concordantes e discordantes são relatadas como idades agrupadas ou centrais, respectivamente, com variação percentual (Galbraith, 1988). Ao longo deste estudo, os erros de idade de traços de fissão são cotados no nível de confiança 1 σ e foram derivados pelo método convencional (Green, 1981 ou Galbraith, 1988). O teste qui-quadrado ($P(\chi^2) \geq 5\%$) foi usado para quantificar a homogeneidade de idade (Galbraith, 1990) usando o software “IsoplotR” (Vermeesch, 2018). O tamanho do diâmetro do etch-pit paralelo ao eixo c (D_{par}) também foi determinado, pois é um parâmetro cinético usado na modelagem da história térmica (Donelick et al., 1999; Ketcham et al., 1999; Donelick et al., 2005) pelo menos quatro valores D_{par} foram medidos por cristal (Fig. 3.4, todas etapas de contagem, tratamento de dados e modelagem foram realizadas no Laboratório de Termocronologia de Baixa Temperatura do Instituto de Geociências da Universidade de São Paulo (IGc/USP). Todos os dados obtidos na contagem e necessários para a modelagem térmica estão em anexo.

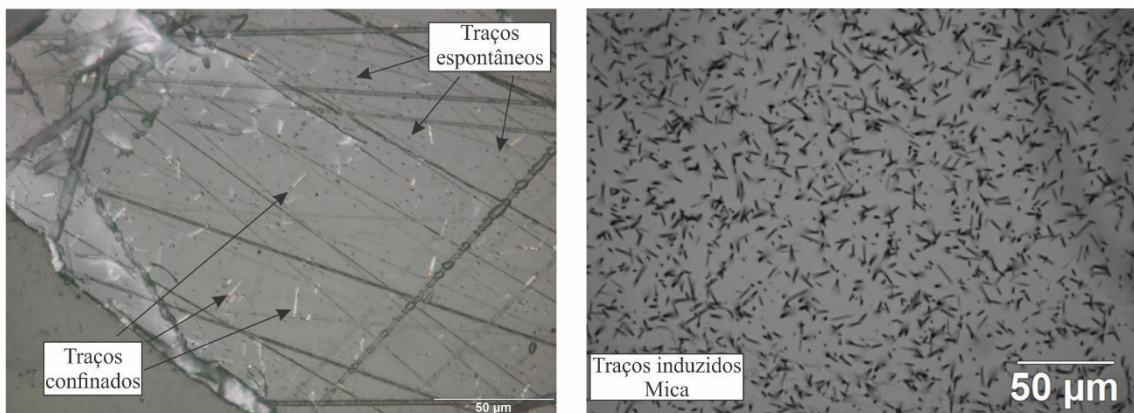
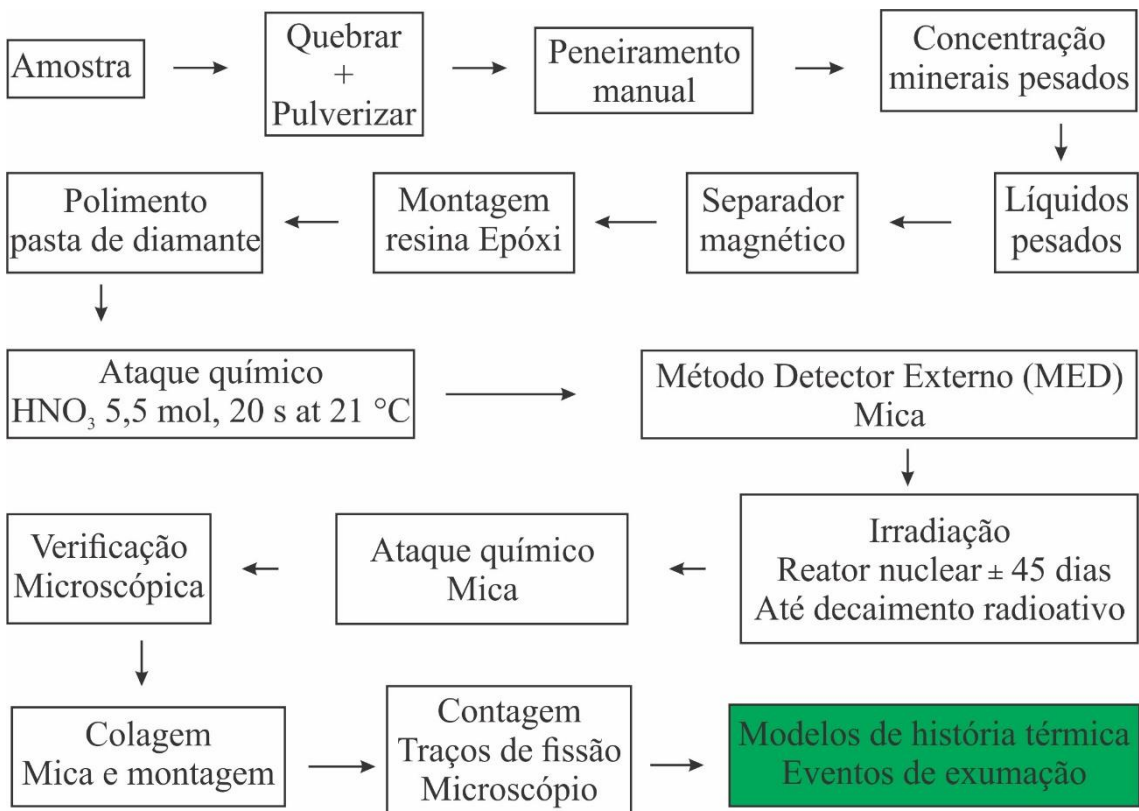


Figura 3.2: Etapas de preparação das amostras para traços de fissão em apatita.

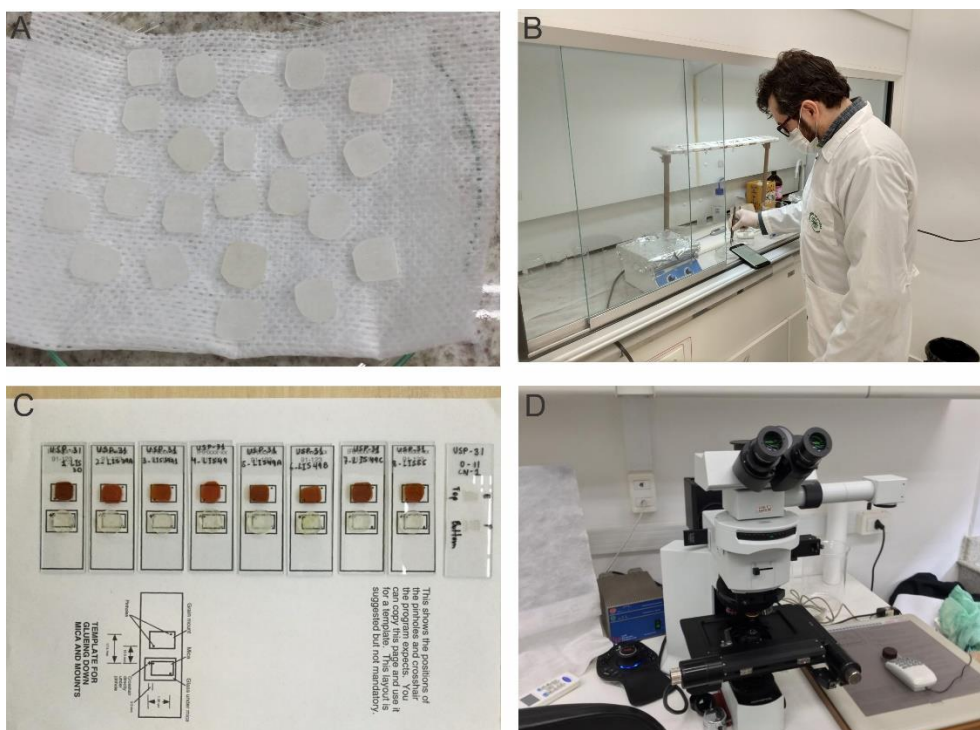


Figura 3.3: Preparação das amostras de apatita. A) Montagem dos grãos em resina. B) Ataque química para revelar traços espontâneos. C) Após a irradiação e ataque nas micas, montagem das amostras para contagem. D) Microscópio para contagem de traços de fissão nas amostras e no detector externo (mica)

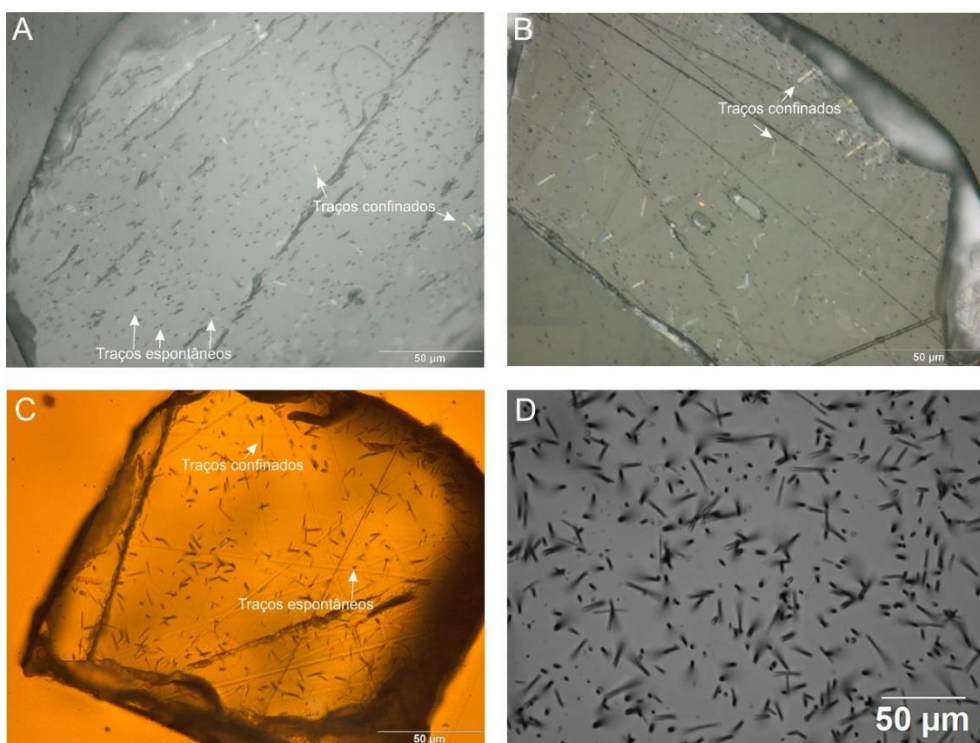


Figura 3.3: Traços de fissão de amostras do norte da Faixa Brasília. A e B) Traços de fissão espontâneos e confinados em cristais de apatita, em luz refletida. C) Traços de fissão espontâneos e confinados, em cristal de apatita, luz transmitida. D) Traços induzidos em mica após irradiação.

CAPÍTULO 4

ARTIGO 1: THE BRAZILIAN MIDWEST LATERITIC DOMAINS: REGOLITH FEATURES AND DYNAMIC

4 ARTIGO 1: THE BRAZILIAN MIDWEST LATERITIC DOMAINS: REGOLITH FEATURES AND DYNAMIC



Contents lists available at ScienceDirect

Journal of South American Earth Sciences

journal homepage: www.elsevier.com/locate/james

The Brazilian Midwest lateritic domains: Regolith features and dynamic

Rodrigo Tokuta Castro ^{a,*}, Adriana Maria Coimbra Horbe ^a, Luis Felipe Soares Cherem ^b^a Universidade de Brasília, Instituto de Geociências, Campus Universitário Darcy Ribeiro, Distrito Federal, Brasília, 70910-900, Brazil^b Universidade Federal de Goiás, Instituto de Estudos Socioambientais, Goiás, Goiânia, 74001-970, Brazil

ARTICLE INFO

Keywords:
 Regolith
 Ferruginous lateritic duricrust
 Lateritic episodes
 Palaeoweathering surface

ABSTRACT

Intracontinental deformations cause the uplift of erosive surfaces and are consequence of lithosphere destabilization processes in cratonic domains. The Atlantic Ocean opening influenced processes 2000 km away from the coast with reflections in the regolith. The Brazilian Midwest regolith is characterised by a stepwise landscape of highlands, mountains, plateaus, inselbergs, canyons, and lowlands that form four morphostratigraphic surfaces. Surface 1 is sustained by quartzite mountains. Surfaces 2 and 3 are mantled by ferruginous lateritic duricrusts. The duricrusts in surface 2 are quartz-hematitic, hardened, columnar, reddish-pink to yellowish-red, have protomodular, fragmental, and pisolithic textures, and reach up to 3 m thick, whereas the duricrusts in surface 3 are more friable, quartz-goethitic, columnar, yellowish-red to orangish-yellow, have a vermiform texture with bioturbated micro-aggregated clay-ferruginous matrix, reaching up to 2 m thick. Surface 4 includes the lower alluvial plains. The purpose of this study was to understand the formation of these regolith surfaces, their relationships, the impact of the lateritic dynamic, and the continental influences as a landscape-shaping agent. The area was studied using SRTM images, swath profiles, and the Roughness Concentration Index, as well as fieldwork control, textures, mineralogy, and geochemistry analysis. Surface 1 marks the regional erosional event, while surfaces 2 and 3 mark two stable well-drained ferruginization weathering episodes and a seasonal drier to humid climate change. Surface 4 sculpts the lowlands. These regolith sequential landforms surfaces were produced in a complex landscape process modelled by an extensive erosional regime as a result of tectonic movements during the Atlantic Ocean evolution evolution and tropical weathering climate since the Neogene, as indicated by the lateritic duricrusts features (textures, mineral, and chemical composition). This landscape is younger than expected for Archean to Paleozoic terrains subjected to tropical weathering, dating back at least to the Paleogene, the age of the majority of older lateritic duricrusts in Brazil and around the world. These younger morphostratigraphic surfaces in cratonic domains, as well as the geological processes involved in tectonic and climate influence, had significant implications for the Brazilian South American Platform regolith.

1. Introduction

In intracontinental detachment modelling, the re-equilibration of the continental hinterland and re-accommodations of lithospheric blocks, in conjunction with lithosphere geothermal gradient, seismic anomalies, and magmatic intrusions (Davis and Kusznir, 2004; Kusznir and Karner, 2007; Brito Neves et al., 2014; Flament et al., 2013, 2015; Fuck et al., 2017; Loutherbach et al., 2017; Hu et al., 2018), can uplift the continental crust in 0.1–1 km (Magee et al., 2017), with direct impact on the relief features (Ribeiro et al., 2018).

In the eastern boundary of South America, the detachment causes the formation of the Mantiqueira and do Mar Mountain ranges, intense alkaline magmatism, and erosive unconformity in the Potiguar Basin

and Borborema Province (Morais Neto et al., 2009; C.H.E. de Oliveira et al., 2016; Ribeiro et al., 2018). There were Andean uplift and several foreland basins formations along the western boundary (Rodaz et al., 2005; Hoorn et al., 2010; Assine et al., 2015). Similarly, in Africa, there was uplift, magmatism, and subsidence (Catuneau et al., 2005; Hanson et al., 2009; Stanley et al., 2013; Guillocheau et al., 2017; Ye et al., 2017). All of these features, which cause erosion, dissection, and hydrographic reorganization, have a direct impact on the continental regolith features, resulting in complex geological, geomorphological, and pedological features (Büdel, 1982; Summerfield, 1991; Saadi, 1993; Saadi et al., 2005; Beauvais et al., 2008; Beauvais and Chardon, 2013; Batezelli and Ladeira, 2016; Ribeiro et al., 2018; Chardon et al., 2018; Côrrea and Monteiro, 2021; Peulvast and Béard, 2021).

* Corresponding author.

E-mail addresses: castrotokuta@gmail.com (R.T. Castro), ahorbe@unb.br (A.M.C. Horbe).

<https://doi.org/10.1016/j.james.2022.103959>

Received 14 February 2022; Received in revised form 25 July 2022; Accepted 28 July 2022

Available online 9 August 2022

0895-9811/© 2022 Elsevier Ltd. All rights reserved.

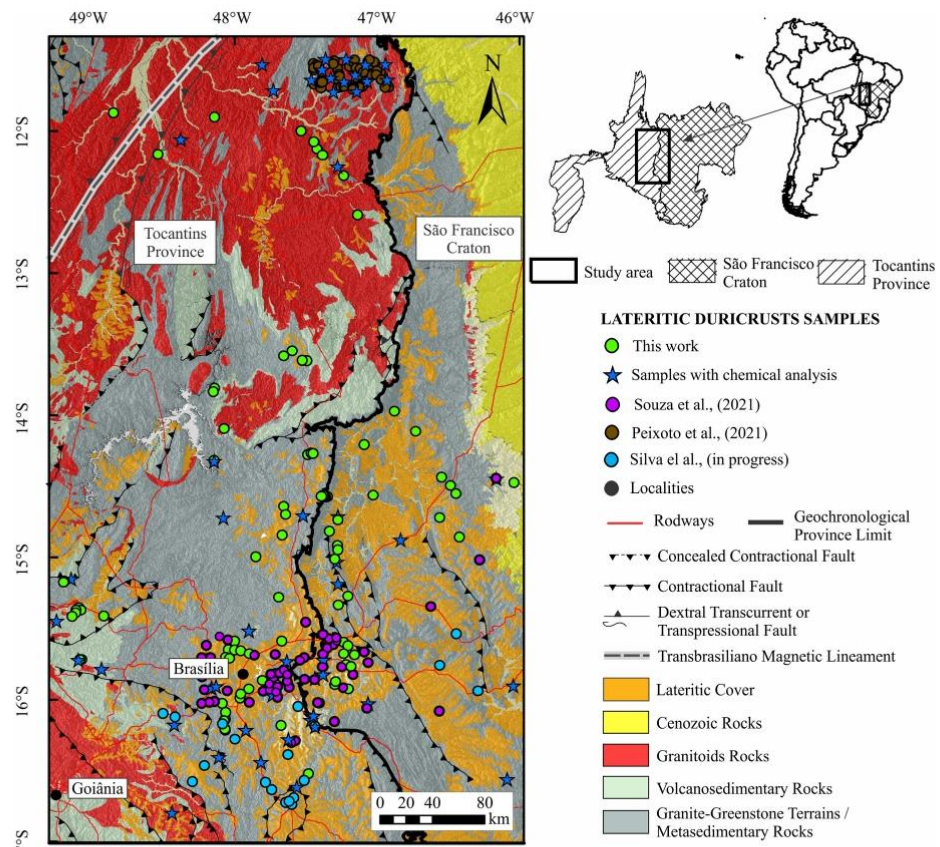


Fig. 1. Simplified geological map of the studied area and sampling locations.

Five regolith paleosurfaces were identified in the Brazilian South American Platform including, Gondwana Surface (Triassic), Post-Gondwana Surface (Cretaceous), South American Surface (Paleocene), Velhas Surface (Pliocene), and Paraguaçu Surface (Quaternary) (De Martonne, 1943; Freitas, 1951; King, 1953, 1956; Bigarella et al., 1965; Salgado, 2007; Valadão, 2009), forming step pediments. There are large bauxite deposits (Paragominas, Juruti, Trombetas, and Almerim deposits) in the South American and Velhas Surfaces in Amazônia, mostly derived from siliciclastic rocks (Bardossy and Aleva, 1990; Boulangé and Carvalho, 1997; Lucas, 1997; Kotschoubey et al., 2005; Costa, 1997; S.B. Oliveira et al., 2016). There are also large deposits in the Midwest of Brazil (Oliveira et al., 2011) and several small bauxite deposits alongside the Atlantic coast (Serra da Mantiqueira) (e.g. Poços de Caldas, Mirai) and Quadrilatero Ferrífero all derived from igneous and metamorphic rocks (Valeton et al., 1991; Melfi, 1997; Oliveira and Toledo, 1997; Leonardi et al., 2011). However, the majority of these bauxites form Amazônia possess hydrothermal origin (Valeton et al., 1991; Leonardi et al., 2011; Moura, 2019). In the younger surfaces, there are ferruginous duricrusts (Costa et al., 2014). The Ar–Ar and U–Th/He ages of these lateritic surfaces (Vasconcelos et al., 1994; Ruffet et al., 1996; Costa et al., 2005; Shuster et al., 2005; Lima, 2008; Monteiro et al., 2014, 2018; Vasconcelos and Carmo, 2018; dos Santos Albuquerque et al., 2020; Heller et al., 2022), are in accordance with several lateritic formation episodes in Africa, India, China, and Australia (Hénocque et al.,

1998; Dammer et al., 1999; Vasconcelos, 1999; Pidgeon et al., 2004; Colin et al., 2005; Spier et al., 2006; Beauvais et al., 2008; Beauvais and Chardon, 2013; Bonnet et al., 2014, 2016; Deng et al., 2016; Mathian et al., 2019; Wells et al., 2019; Jean et al., 2019). The older episodes are from the Late Cretaceous, pre-Africa, and South America detachments, and the peaks of most bauxite deposit formation are in the Paleocene-Oligocene (~60–50 Ma, ~45–40 Ma, ~30 Ma), with younger ferruginous episodes in the Middle Miocene to Pliocene (18–10 Ma, 7.2–5.8 Ma, and 3.4–2.9 Ma).

Under repeated arid or semi-arid pedimentation and seasonal tropical weathering, the bauxites and ferruginous duricrusts sustain planing surfaces formed episodically in some areas and continuously in others (Bardossy and Aleva, 1990; Tardy and Roquin, 1998; Burke and Gunell, 2008; Retallack, 2010; Beauvais and Chardon, 2013; Grimaud et al., 2015). The bauxites are mostly associated with humid periods, necessitate long-term climatic changes, and are from the Paleogene, whereas the ferruginous ones are generally younger and are from the Neogene. This relationship between composition and age identified in South America (Costa, 1997; Kotschoubey et al., 2005) is an important feature for the establishment of surface chronology.

Diverse paleoclimates and climates act on different tectonic compartments, substrates, and reliefs on the South American Platform, resulting in a diverse landscape (Salgado et al., 2015). Brazil is contained within a single geotectonic unit known as the South American



Fig. 2. Lateritic regolith of the study area. A) Typical quartzite mountainous ranges and stepped relief with dissected valleys of surface 1 carved on the meta-sedimentary rocks of the Araí, Paranoá, and Bambuí Groups. B) The quartzites mountain ranges of surface 1 and the ferruginous lateritic surface 2. C) The great Urucuia formation escarpments of surface 2 and the lower ferruginous lateritic surface 3 in the eastern boundary of the study area. D) The great Bambuí Group escarpment of surface 2 relative to the lower ferruginous lateritic surface 3 in the western boundary. E) View of the highlands carved on the granite-gneiss rocks of surface 2 and the lower ferruginous lateritic surface 3. F) The ferruginous lateritic plateaus of surface 2 and the lower ferruginous lateritic surface 3 are both carved on basement rocks of the Porto Nacional and Rio dos Mangues Complexes, granite-gneiss domain, Aurumina and Pedra Branca Suites, the metasedimentary rocks of the Araí, Canastra, Paranoá, Araxá, Canastra, and Bambuí Groups and the sedimentary rocks of the Pimenteiras Formation and Urucuia Group.

Platform. Although, vertical movements and climate influence regolith features (Margirier et al., 2019; De Putter and Ruffet, 2020), the believed tectonic stability of South American Platform indicates climate is the main landscape-shaping agent since the Early Cenozoic.

The Brazilian Central Plateau is a geomorphological mega compartment of the Brazil Atlantic (Saadi et al., 2005; Salgado et al., 2015). It is composed of highland, mountains, plateaus, tablelands, inselbergs, canyons, and lowered dissected geofoms areas carved by the three major Brazilian hydrological basins (Paraná, São Francisco, and

Amazonas) (Braun, 1971; Mamede et al., 1981a, 1981b; Nascimento, 1991; Moreira, 1995; Martins and Baptista, 1999). Archean to Paleozoic rocks outcrop in this region, and unlike the well-developed and preserved lateritic bauxites of the Amazon, only large ferruginous lateritic duricrusts occur (Martins et al., 2004; Latrubesse, 2006; Moraes, 2014; Ribeiro, 2017; Souza et al., 2021; Peixoto et al., 2021). Despite the presence of favourable climatic conditions for the formation of bauxite (Price et al., 1997), only hydrothermal bauxites have been identified in this region (Valeton et al., 1991; Moura, 2019).

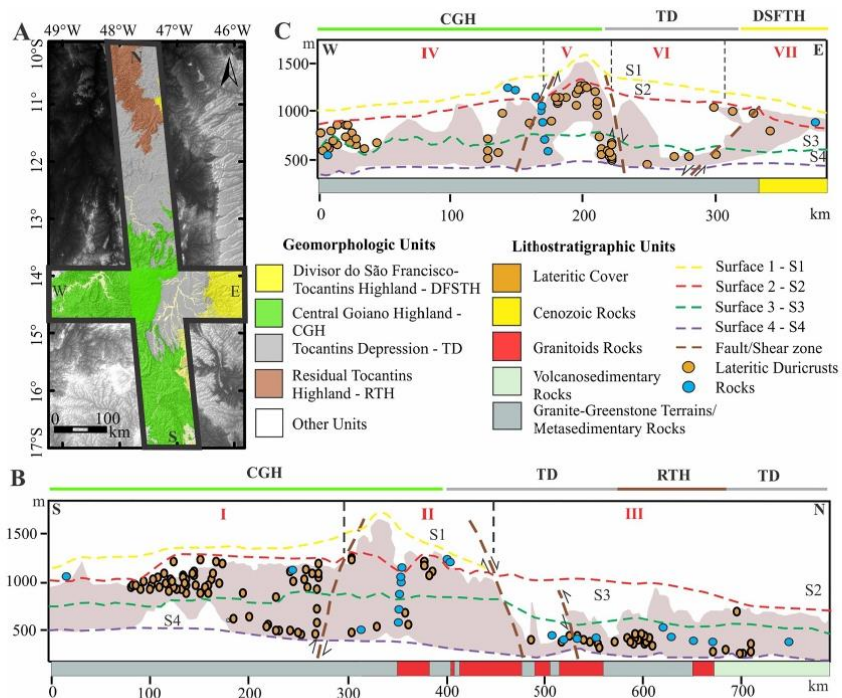


Fig. 3. A) Position of the swath profiles with approximately 100 km EW wide and 800 km NS long. B) NS swath profile between Tocantins Province and the Parnaíba Basin. C) LW swath profile between Tocantins Province and the Sanfranciscan Basin. The dashed lines delimit the surfaces. The geomorphologic units are at the top and the lithostratigraphic units are at the base.

Because lateritic duricrusts and their features such as altitude, mineral, and chemical composition are used to establish regolith landform development, providing relative and absolute ages (Ollier and Pain, 1996; Costa, 1997; Beauvais et al., 2008; Beauvais and Chardon, 2013; Vasconcelos and Carmo, 2018), an area in the Brazilian Midwest was selected (northern of Goiás and southern of the Tocantins States) (Fig. 1), where the regolith form a complex geological, geomorphological, and pedological scenario. The purpose of this research was to better understand this scenario, the formation of the regolith surfaces, the relationship between the surfaces, lateritic dynamics, regional, and continental influences in shaping the landscape. The area was investigated using SRTM images, scanning profiles, and the Roughness Concentration Index with fieldwork control, textures, mineralogy, and geochemistry.

2. Study area and geological and geomorphological background

There is a wide range of Archean to Proterozoic igneous and metamorphic rocks in the study area (granites, granulites, gneiss, quartzites, rhythmites, slates, schist, phyllite, and carbonates). In the southern and the western part, the Tocantins Province (Almeida et al., 1981) comprises two-fold belts: Araguaia and Brasília. The Araguaia belt forms the basement granite-greenstone domain (Porto Nacional and Rio dos Mangues Complexes) and the Brasília belt comprises the Goiás Massif (granite-greenstone terrains, orthogneiss, and mafic-ultramafic complexes), the Metamorphic Nucleus (metasedimentary rocks and high-grade metamorphic rocks), and the Goiás Magmatic Arc (orthogneiss terrains and volcanic-sedimentary sequences) arranged in faults, folds, and thrust. The crystalline basement is represented by Aurumina

and Pedra Branca Suites, and the metasedimentary sequences (Fig. 1) by Araí, Canastra, Paranoá, Araxá, Canastra, and Bambuí Groups (Brito Neves and Cordani, 1991; Fuck et al., 1994, 2017; Pimentel et al., 1999, 2011; Dardenne, 2000; Rodrigues et al., 2010; Campos et al., 2013; Guadagnin and Chemale, 2015).

The Cenozoic deposits are formed by sandstones in the eastern part (Urucuia Group, Sanfranciscana Basin) (Campos and Dardenne, 1997). Extensive lateritic duricrusts are widespread in the area (Latrubblesse, 2006; Moraes, 2014; Ribeiro, 2017; Souza et al., 2021; Peixoto et al., 2021). The strike-slip shear Transbrasiliano Lineament zone, with NE main direction (Schobbenhaus et al., 1975), extending across the Tocantins Province, cut the area and was active from the Cambrian to the Cenozoic, controlling the structuring of Phanerozoic basins (Vidotti et al., 1998; Castro et al., 2014; Curto et al., 2014).

The dissected geoforms of highlands, mountain ranges, plateaus, inselbergs, canyons, and lowlands are grouped into four geomorphologic units: Central Goiano Highland (CGH) in the Midwest area, Divisor São Francisco-Tocantins Highland (DSFTH) in the east area, and Tocantins Depression and Tocantins Residual Highland (TDRH) in the north and north-western area (Fig. 2) (Mamede et al., 1981a; Nascimento, 1991).

The CGH has the most diverse shapes, lithologies, and altitudes (Braun, 1971; Nascimento, 1991; Moreira, 1995), resulting in three geomorphological structures: A) a boomerang-shaped mountain complex (Veadeiros-Araí-Nova Roma) measuring 120 km in the SW-NE direction and 130 km in the NW-SSE direction. It is 350–1650 m a.s.l. high in the central part and is strongly controlled by faults and folds sculpted valleys, mountains, and plateaus, on metasedimentary mainly quartzites (Araí, Paranoá, and Bambuí Groups) and granitic Proterozoic

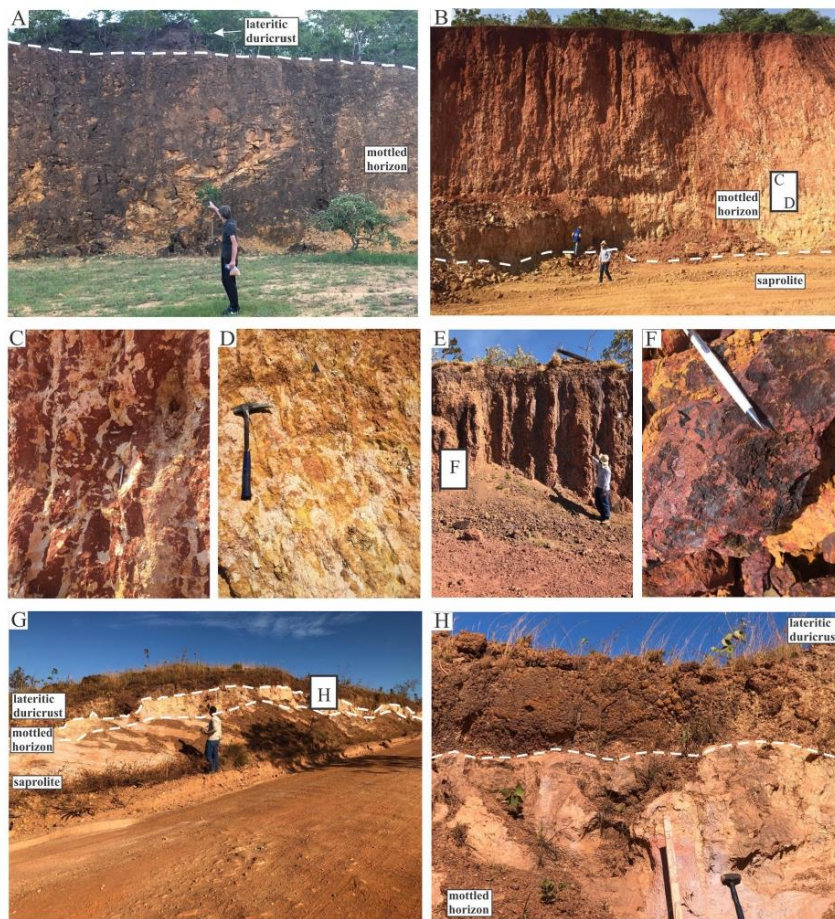


Fig. 4. A) The lateritic profile on the Urucuia Group, surface 2, showing the saprolite, mottled horizon, and the lateritic ferruginous duricrust on the top. B) Lateritic profile on the Paranoá Group, surface 2, showing the saprolite, mottled, and the ferruginous lateritic duricrust on the top. C) Detail of B showing the hematite-kaolinite reddish and whitish stains typical of the top of the mottled horizon. D) Detail of B showing the goethite-kaolinite ochreous to whitish stains typical of the base of the mottled horizon. E) Detail of the columnar ferruginous lateritic duricrust on the top of the profile of Fig. B. F) Detail of the vermiciform ferruginous lateritic duricrust of Fig. B. G) General view of the lateritic profile of S3 on the Paranoá Group. H) Detail of G showing the mottled and the ferruginous lateritic duricrust.

rocks (Aurumina and Pedra Branca Suites) (Figs. 2 and 3); B) high plateaus (Alto Tocantins-Paranába Plateau) in the southwest central part, it is 1000 and 1200 m a.s.l. and is formed by elongated mountain ranges and plateaus also on the metasedimentary Proterozoic rocks (Araí, Paranoá and Bambuí groups) and mafic-ultramafic complexes (Canabirava, Niquelândia, and Barro Alto; (Colin, 1990; Nascimento, 1991; Oliveira et al., 2011; Moraes, 2014) emerge; C) a low plateau (The Distrito Federal Plateau) between 500 and 1240 m a.s.l. located in the south of the study area, it has slightly wavy and dissected flat shapes, sculpted in the metasedimentary Paranoá and Bambuí Groups (Fig. 2).

On the east side of the study area, the DSPTH or Serra Geral de Goiás (Fig. 2) consists of plateaus 500–1200 m a.s.l. formed on Cretaceous

sedimentary rocks (Urucuia Group). The Tocantins Depression (TD) in the north-central part is a large lowland that separates the mountain range of CGH from the DSPTH (Fig. 2). These areas at 200–600 m a.s.l. on the metasedimentary rocks (Araí, Paranoá and Bambuí Groups), were sculpted by the Tocantins River (Mamede et al., 1981a; Nascimento, 1991; Moreira, 1995; Costa et al., 2010). The RTH on the north (Fig. 2) with 500–900 m a.s.l. and great escarpments is formed by 12–60 km long mountain ranges sustained by the basement rocks (Tocantins Province) and sedimentary rocks (Paranába Basin) Mamede et al. (1981b); Costa et al. (2010). The Corumbá and São Francisco rivers cut through the southern and eastern parts of the study area.

3. Materials and methods

To study the lateritic regolith evolution in the Midwest of Brazil, 112 samples were collected. Half of these samples were used to develop mathematical mapping regolith techniques by Peixoto et al. (2021), Souza et al. (2021), and Silva et al. (in preparation).

For cartographic analyses and better identification of the geological and dissected geoforms and the landscape lateritic duricrusts

relationship, a swath topographic profile using 54 SRTM radar (Shuttle Radar Topography Mission) together with a spatial resolution of 90 m was obtained in the USGS (<https://earthexplorer.usgs.gov/>) was used. The swath topographic profiles (STP), 100 km wide along the N-S direction (extension of 780 km with 69.076 quoted points) and L-W direction (extension of 380 km with 26.155 quoted points) (Fig. 3), were created in ArcGIS 10.6® software using the automatic method of Silva and Silva (2018). These STPs that use a digital elevation model (DEM)

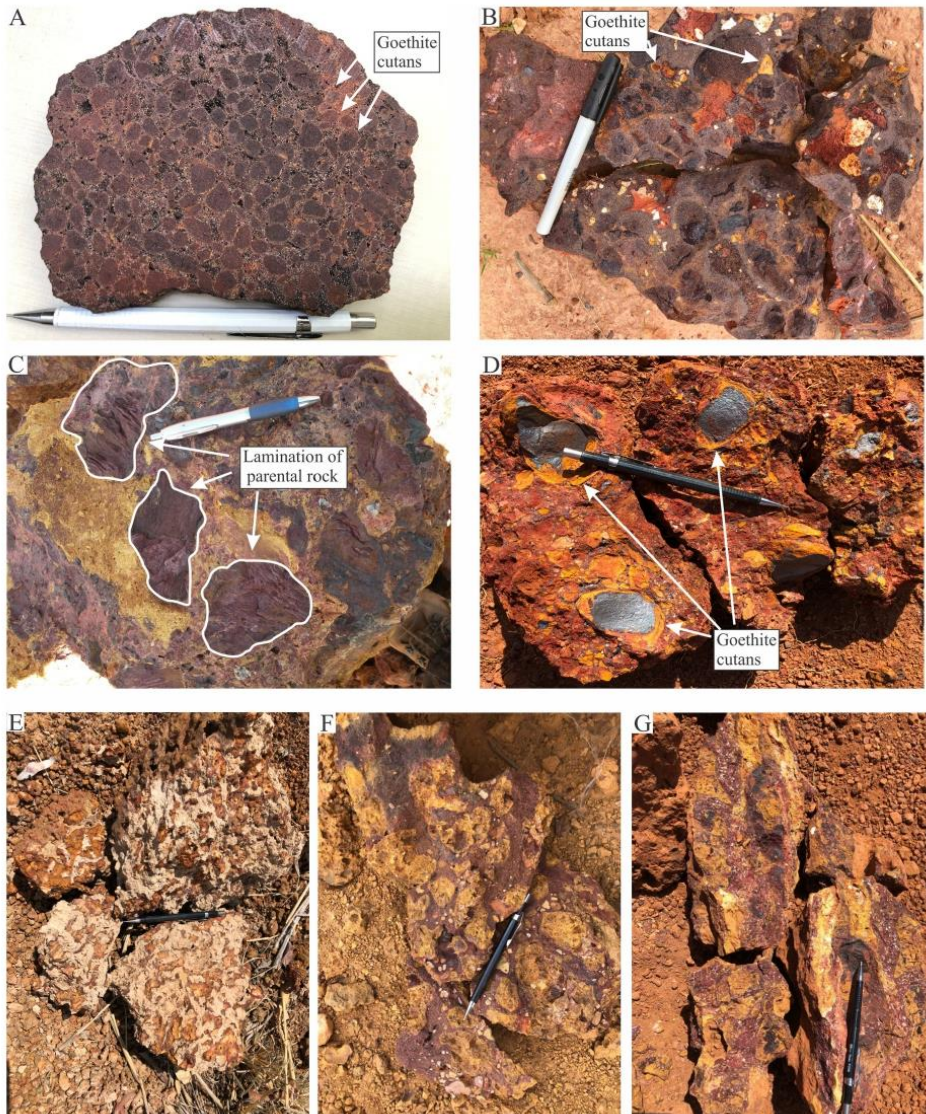


Fig. 5. Distinct ferruginous lateritic duricrusts in the study area, A to D are those of surface 2, and E to G are those of surface 3. A and B) Hard ferruginous pisolithic duricrusts showing the hematite pisoliths with goethite cutans and quartz grains from the Urucuia Group. C) Preserved fragments of ferruginous phyllite and quartz grains in a yellow oolitic matrix of the ferruginous lateritic duricrust of surface 2 from Canastra Group. D) Protonodular ferruginous lateritic crust with two hematite generations, one metallic gray and the other brown to red of the surface 2 from the Paranoá Group. E, F, and G) Three samples of the vermicular ferruginous lateritic duricrust of surface 3 from Paranoá Group.

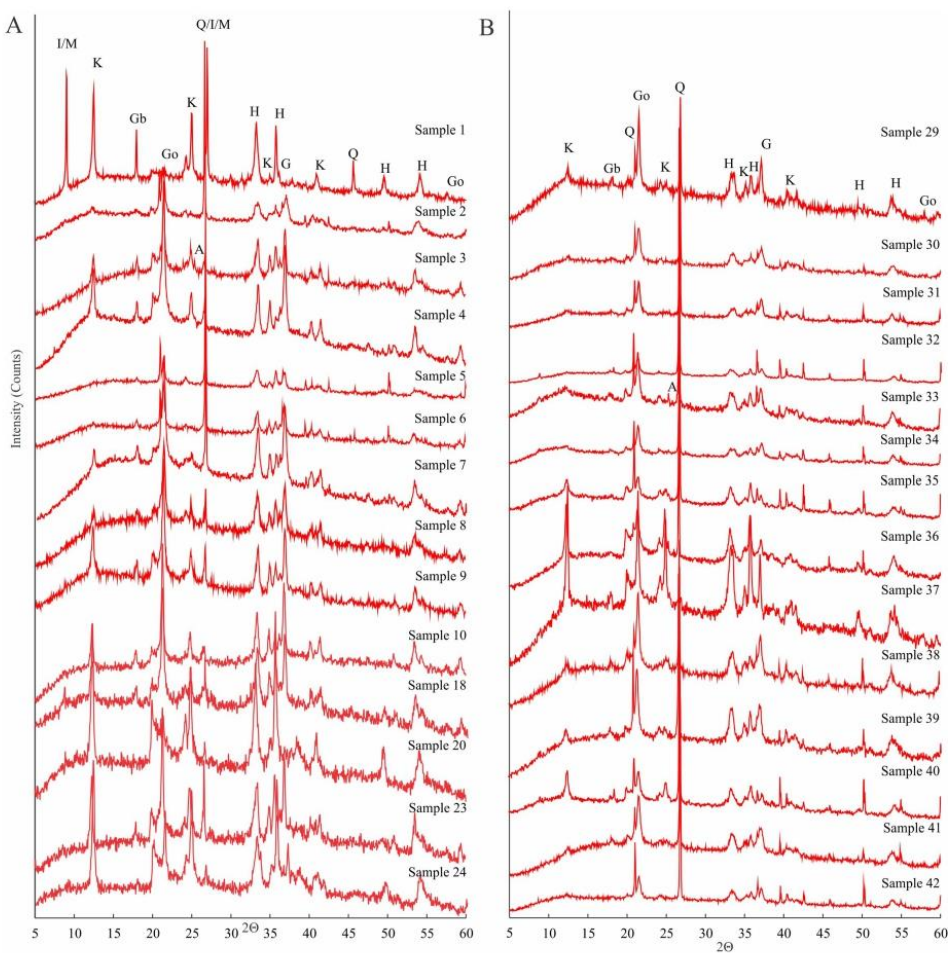


Fig. 6. X-ray diffractograms of the lateritic duricrusts of the study area, samples and most common minerals at duricrust identified by XRD. A) Surface 2. B) Surface 3. A – anatase, Gb – gibbsite, Go - goethite, H - hematite, I – illite, K - kaolinite, M – muscovite and Q – quartz.

allow for a more refined and complete relief view and topographic slopes recognition than traditional ones done along a line (Bavil and Bavil, 2019; Jaiswara et al., 2020; Bertolini et al., 2021; Fonseca et al., 2021). From the digital elevation model, the software extracts nearly 100,000 topographic points (DEM). In the figure, each topographic point is represented by a single black circle, with the altitude of the point plotted on the y-axis and the geographic position plotted on the x-axis. The yellow dots represent the lateritic duricrust samples' altitude and geographic location.

The roughness concentration index was calculated using the same software (RCI) (Sampaio and Augustin, 2014). The slope ArcGIS function and the spatial declivity per unit area from the DEM are used in the calculation. This procedure resulted in the creation of a matrix in which each pixel stores a unique value. The matrix was transformed into a point file for the application of the Kernel density estimator, which transforms the obtained index values into spatial data. The six classes (flat, smoothly wavy, wavy, strongly wavy, steeped, and heavily steepled) were identified according to the spatial distribution, and recurrence of the slope declivity (<1, 1–3, 3–6, 6–14, 14–20 and > 20°)

allowed the general relief units to be identified. The STP and the RCI allow for the identification of threshold transition bands, the scaling of relief features, and the description of regolith surface features; these two tools are used on a regional-scale (resolution of 90 m).

Twenty of the 56 samples collected for this study were analysed for mineral and chemical compositions, according to parent rock and relief (Supplemental data), and an aliquot was pulverised. The other 36 with mineral and chemical analysis are from Peixoto et al. (2021), Souza et al. (2021), and Silva et al. (in preparation). The mineral was identified using X-ray diffraction (RIGAKU ULTIMA IV) with a Cu tube at Universidade de Brasília in the reading range of 5° to 60° 2θ. The concentrations of major and minor elements (SiO_2 , Al_2O_3 , Fe_2O_3 , CaO , MgO , Na_2O , K_2O , TiO_2 , and P_2O_5) were determined by ICP-AES after fusion with LiBO_2 , and aqua regia digestion. Loss of ignition (LOI) was done by heating the samples at 1000 °C. These chemical analyses were carried out at ALS Corlab, Brazil.

Table 1
Distribution of major elements (%) and wt of lateritic duricrusts in the study area.

	Surface 2 (n = 28)			Surface 3 (n = 28)		
	Average	Maximum	Minimum	Average	Maximum	Minimum
SiO ₂	24.78	38.10	16.30	36.00	51.30	21.30
Al ₂ O ₃	16.57	23.40	3.53	14.21	22.00	9.29
Fe ₂ O ₃	44.55	55.80	28.50	37.24	50.10	26.80
CaO	0.01	0.04	0.01	0.05	0.18	0.01
MgO	0.07	0.59	0.01	0.09	0.29	0.01
Na ₂ O	0.02	0.21	0.01	0.01	0.03	0.01
K ₂ O	0.32	1.86	0.01	0.30	0.93	0.02
TiO ₂	0.88	1.93	0.14	0.69	1.65	0.28
P ₂ O ₅	0.10	0.59	0.02	0.11	0.34	0.02
LOI	11.86	14.70	6.49	10.65	12.60	7.68
Total	99.27	101.90	94.92	99.48	101.94	96.31

4. Results

4.1. Topographic features and weathering surfaces

The 100 km wide swath topographic profiles (STP) along the NS and LW directions show abrupt topographic variation (Fig. 3). Three blocks limited by thrust faults were identified (I, II e III) in the NS profile and four (IV, V, VI, VII) in the LW profile (block II, profile NS and block V profile LW are the same).

At the top of these blocks there are quartzites mountains (1230–1650 m a.s.l.). Widespread on the plateaus, and on the lowland, there are ferruginous lateritic duricrusts (230–1230 m a.s.l.), and on the river network plains, there are alluvial sediments (<230 m a.s.l.) (Martins et al., 2004; Latrubesse, 2006; Moraes, 2014; Ribeiro, 2017; Peixoto et al., 2021; Souza et al., 2021). These features allow the four weathering regolith surfaces in the study area to be highlighted (Figs. 2 and 3, and Supplementary data).

S1: Encompasses the high quartzites mountain ranges with abrupt scarps (Araí, Bambuí, and Paranóia Groups) of blocks II and V in the NS and EW profiles, respectively (Figs. 1, 2, 3B, and 3C). This surface, located in the study area's centre, ranges in elevation from 1230 to 1650 m above sea level (a.s.l.) and contains quartzites, Litholic soils, and Spodosols (Moreira, 1995). The STP shows high roughness aligned hilltops (Fig. 3B and C) with a slope of 14–20° and >20°. The relief was classified as steeped and strongly steeped by these RCI

indexes, indicating high dissected and erosional morphology surface properties.

S2: This is the largest and most complex spatial surface of the study area. It gathers both the Archean to the Proterozoic basement and the metasedimentary rocks, as well as the Paleozoic sedimentary rocks. Block I of the NS profile and blocks IV to VII of the LW profile (Fig. 3B and C) contain the mosaic of mountains, highlands, plateaus, and escarpments. (range between 750 and 1230 m a.s.l.). These regolith features are the most frequent landforms in the southern, eastern, and northern area, and are supported by rocks and widespread harder ferruginous lateritic duricrusts. Associated with these rocks are Oxisol and Cambysols (Moreira, 1995) (Figs. 2–4). Three successive subsurfaces were recognized in the STP according to the physical features: 1. hilltops that decrease gradually from 1200 m to 800 m a.s.l. in the southern part of the block I (Fig. 3B) classified in the RCI, as well as S1, in steeped and strongly steeped (slope of 14–20° and >20°, respectively); 2. Hilltops that decrease gradually from 1200 m to 1000 m a.s.l. in the eastern part of the block I till the blocks VI and VII (Fig. 3C) that are classified in the RCI as flat to smoothly wavy, with a slope between <1° and 1–3°, where harder lateritic duricrusts; 3. An intermediary surface with hilltops that decrease from 800 m to 740 m a.s.l. in the central part of block II to block III and in the central part of block IV to the west (Fig. 3B and C), classified in the RCI as wavy to strongly wavy (slopes from 3 to 6 to 6–14°, respectively).

S3: This encompasses mountains, plateaus, inselbergs, canyon, and escarpments mosaic between 230 and 750 m a.s.l. (Figs. 2 and 3B), formed from the Archean to the Proterozoic basement and metasedimentary rocks, and the Paleozoic sedimentary rocks, and supported by rocks, softer lateritic duricrusts, Oxisol and Cambysols (Moreira, 1995). This lower surface has abrupt contact with other surfaces ones as shown by the great escarpments between blocks II and III and between VI and VII (Fig. 3B and C) and some waterfalls. The RCI classifies it as wavy to strongly wavy (slopes ranging from 3–6° to 6–14°, respectively) as subsurface 2, but at a lower altitude (Fig. 3B and C).

S4: Encompasses the alluvial plains <230 m a.s.l. containing outcrop rocks, saprolite, and alluvial sediments. This surface has abrupt contact with S3 forming a canyon. The RCI classifies it as flat to smoothly wavy, with a slope between <1° and 1–3°, respectively.

4.2. Lateritic duricrust and their chemical composition

The lateritic duricrusts in the study area occur as blocks and/or slabs and outcrop in the relief breaking or in the road cuts (Fig. 4). They are derived from granites, granulites, gneiss, quartzites, rhythmites, slates, schists, phyllites, and sandstones (Figs. 1 and 2).

The lateritic duricrusts in S2 are hardened, reddish-pink to yellowish-red, display columnar structure, protonodular, fragmental, and pisolithic textures, reaching up to 3 m thick. The majority of the

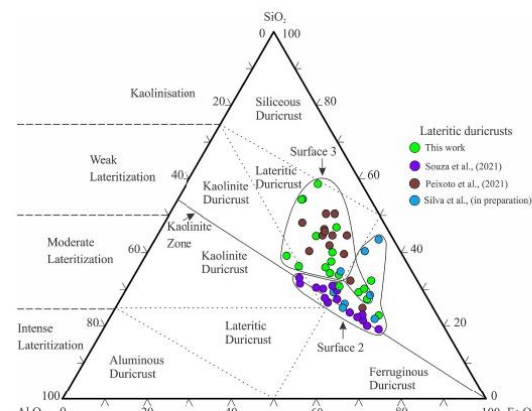


Fig. 7. Ternary diagram SiO₂ – Al₂O₃ – Fe₂O₃ showing the classification of the ferruginous lateritic duricrusts according to Schellmann (1983).

ferruginous pisoliths have goethite brown cutans with nanometric crystals developed perpendicular to the edge of the hematitic-kaolinite-quartz cores (Fig. 5A–D). The lateritic duricrusts in S3 are more friable, yellowish-red to orangish-yellow, display columnar structure and vermicular texture with clay-ferruginous matrix (Fig. 5E–G), and a thickness of 2 m. Occasionally, the laminations structure of the parental rock is preserved (Fig. 5C). The lateritic duricrusts are usually covered with 1 m thick Oxisol, especially when dismantled.

All lateritic duricrusts are composed of quartz grains, hematite, goethite, with variable content of kaolinite, and a minor amount of gibbsite, anatase, and illite/muscovite (Fig. 6). Gibbsite occurs preferentially in S2 (samples 1, 3, 4, 7, 8, 9, 10, 18, and 23). They contain 26.8–55.8% Fe_2O_3 , 16.3–51.3% SiO_2 and 3.53–23.40% Al_2O_3 . The CaO , Na_2O , K_2O , and MgO contents are always lower than 2% (Table 1 and Supplementary data). These compositions allow for the classification of the majority of S2 lateritic duricrusts as quartz-hematitic (having the highest hematite and Fe_2O_3 content, up to 55.8%) and the majority of S3 lateritic duricrusts as quartz-goethitic (up to 50.1% of Fe_2O_3). They are respectively the product of intense to weak lateritization environment effect and ferruginous duricrust to kaolinite duricrust/lateritic duricrust (Schellmann, 1983; Bourman and Ollier, 2002; (Fig. 7); however, the classification as weak is due to the high amount of SiO_2 as quartz, with the majority of them as pebbles and coarse sand grains. These high quartz grain contents in lateritic duricrusts are primarily derived from quartzites and Cenozoic sandstones (Urucuia Group), which also cause a lower kaolinite content in some lateritic duricrust located further north and northeast.

5. Discussion

The geomorphologic units that form the regolith scenario of the study area evolve through landscape dissection, which is the process by which paleolandscape remnants become isolated as relics. Large truncated bedrock outcrops surrounded by eroding slopes or scarps form a stepwise surface during this process. The topographic position, the hardness features, the mineral and iron content of the lateritic duricrusts, and the long-term climatic change gradient for bauxite formation relative to the ferruginous ones, are used to correlate and establish putative ages for the regolith surfaces (Thomas, 1995; Costa, 1997; Tardy and Roquin, 1998; Twidale and Boume, 1998; Kotschoubey et al., 2005). According to this premise, the most eroded surface in large quartzite mountains is the higher steeped to heavily steeped (high roughness indices) S1 (1650–1230 m a.s.l., block II/V). It was formed as a result of the higher denudation resistance of quartzite and represents the erosional process associated with the stripping of an exhumed feature.

The S2 and S3 in lower flat to strongly wavy dissected plateaus (S2 = 780 and 1230 m a.s.l., S3 = 230 and 780 m a.s.l.), where there are widespread ferruginous lateritic duricrusts (Figs. 2, 3, 5 and 7), mark an episode of weak to strong stable lateritic weathering conditions in the study area, although the weak classification of some S3 lateritic duricrust, (Fig. 7), is a consequence of the high amount of quartz relicts fragments and grains derived from the quartzite and the Cenozoic sandstones parent rock. The formation of these ferruginous lateritic duricrusts from the weathering of Archean to Proterozoic and Palaeozoic igneous, metamorphic, and sedimentary rocks indicates a dry to seasonally wet tropical climate (Price et al., 1997; Zachos et al., 2001; Maizatto, 2001; Thomas, 2008). The higher, harder, thicker and more resistant protomodular, fragmental, and pisolithic quartz-hematitic lateritic duricrusts with higher gibbsite and Fe_2O_3 content of S2, relative to the more friable vermicular quartz-goethite lateritic duricrusts with higher SiO_2 and lower Fe_2O_3 content of S3 (Table 1), highlight two weathering ferruginization episodes in the study area. These episodes indicate younger, stable, well-drained, and oxidizing conditions, unlike bauxite which needs a long-term (Paleogene) climatic change gradient. Stratigraphic correlations with other lateritic duricrusts from Amazonia (Costa, 1997; Kotschoubey et al., 2005; Allard et al., 2018; dos Santos

Albuquerque et al., 2020) and the Quadrilátero Ferrífero region (Monteiro et al., 2014) allow linking these ferruginous lateritic duricrusts to younger Neogene ferruginization episodes (<25 Ma). S4 (below 230 a.s.l. high) marks the erosional alluvial plains drained by the actual river network.

These two main processes, erosion followed by lateritic weathering ferruginization episodes, reflect the long denudation history of the Gondwanaland/Brazilian Plateau, as indicated by Saadi (1993), Ab'saber (2000), Marangoni and Mantovani (2013), and Ribeiro et al. (2018), all of which are related to the uplift of the South American Platform during Atlantic Ocean evolution and tropical climate. The Transbrasiliense Lineament (Fig. 1), which cut the study area in the NE direction and was reactivated in the Cenozoic (Vidotti et al., 1998; Castro et al., 2014; Curto et al., 2014), must have accelerated the extensive erosional process that formed the quartzites mountain ranges at least until the Middle Cenozoic, as indicated by regolith features. Since a tropical ferruginization weathering process predominated, the extensive ferruginous lateritic surfaces in the study region have formed.

Fault in the quartz-hematitic lateritic duricrusts of S2, as well as grabens, tectonic valleys, fluvial asymmetric valleys, and valleys with residuals escarpment, reinforce tectonic reactivation (Campos et al., 2016; Martins-Ferreira and Campos, 2017) in the study area. This reactivation, which occurred primarily as vertical and transcurrent movements in the Eocene to Middle Pleistocene, along Precambrian geosutures in the Brazilian South American Platform as a result of Atlantic Ocean evolution (Saadi, 1993; Saadi et al., 2005; Salgado et al., 2015), indicates that the South American Platform was not stable at this time. Thus, the long denudation history of the Gondwanaland/Brazilian Plateau landscape was caused by factors other than climate. While tectonic reactivation dissected the exhumed landscape, the formation of lateritic duricrusts suggests more stable tectonic conditions, *in situ* chemical weathering and iron accumulation.

The identification of a second lateritic episode (quartz-goethitic S3) surrounding the higher dissected S2 quartz hematitic lateritic surface indicates that the previous lateritic surface was dissected, resulting in the plateaus mosaic between 750 and 1230 m a.s.l. in great scarps. A lower surrounding erosional stripping surface (S3), outcropping rocks, and sculpting inselberg and canyons were formed (Figs. 1–3). The tropical climate in this lowland gives rise to the younger S3 lateritic surface (230–750 m a.s.l.). The progressive tropical ferruginization episode on the higher S2 surface made the lateritic duricrusts more leached, harder, and Fe_2O_3 rich, resulting in more complex protomodular, fragmental, and pisolithic textures. Moreover, the hematitic pisoliths involved by goethite cutans in the S2 lateritic ferruginous duricrusts and the presence of gibbsite (Fig. 5), indicate a more humid climate in the modern lateritization event of S3 than in S2. Later humid conditions favoured the advancement of the inland drainage network, regressive erosion, weathering, and ferruginization, resulting in the formation of the younger quartz-goethitic lateritic duricrust surface.

The escarpments highlighted in the irregular swath profiles (Figs. 2 and 3) as well as by some waterfalls highlight the dissection of S2 relative to S3. The drainage network incised channels and escarpments in the eastern study area (blocks I, II and III and V, VI, and VII) (Fig. 3) modelled by the Tocantins River network, also support the Cenozoic erosion of the Paleozoic Urucuia sedimentary Group. ^{10}Be indicates a low erosion rate of 4.5 m Ma^{-1} and a lateral displacement between 37 ± 5 and 68 ± 6 m Myr^{-1} in the region (Braucher et al., 2004), which favours iron accumulation and lateritic surfaces formation.

All these sequential surfaces with mountain ranges, highlands, plateaus, inselbergs, lowlands, canyon, and great escarpments on metamorphic, igneous, and sedimentary rocks and the younger Neogene extensive tropical lateritic duricrust residual surfaces, form the modern complex stepped land surfaces in the cratonic Midwest of South America regolith along the Late Cenozoic. The high tectonic dynamism in the landscape shape as a result of Atlantic Ocean evolution and climate influence is highlighted by hydrographic reorganization, river incision,

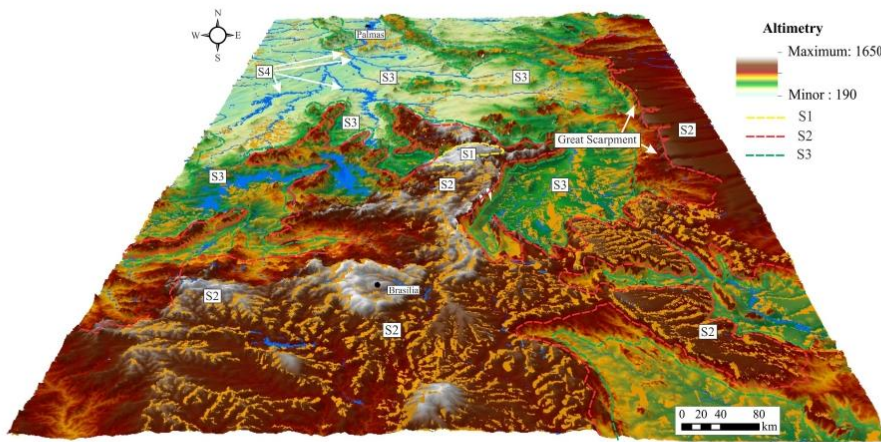


Fig. 8. Regional main topographic features and weathering surfaces of the study area.

and a large amount of clastic sediments transported to the north out of the study region (Araguaia Formation, Ribeiro, 2017).

We interpret the surfaces marker of morphostratigraphic units using the age-elevation relationships (older surfaces higher in the topography) (Figs. 3 and 8).

6. Conclusions

The study of the Brazilian Midwest regolith revealed a complex geological, geomorphological, and pedological stepwise scenario with mountains, highlands, plateaus, escarpments, inselbergs, and canyons formed on Archean to Cenozoic rocks. In this scenario, four surfaces with particular geomorphological and geochemical features and two lateritization phases were identified in the intermediary surfaces. These surfaces were formed as a result of erosion episodes that sculpted the exhumed resistant quartzites mountain ranges, as well as a dry to seasonally contrasted wet tropical climate, which formed quartz-hematic and quartz-goethitic lateritic surfaces. Humid conditions are indicated by S3 lateritic duricrusts with goethite cutans perpendicular to the edge of the hematitic-kaolinite-quartz cores. This regolith scenario highlighted by quartzites mountains and lateritic duricrusts, has existed since the Neogene (<25 Ma) as a result of continental crust uplift and tectonic reactivation during the Atlantic Ocean evolution and extensive tropical weathering.

Credit authorship contribution statement

Rodrigo Tokuta Castro: Writing – review & editing, Writing – original draft, Visualization, Validation, Supervision, Software, Methodology, Formal analysis, Data curation, Conceptualization. **Adriana Maria Coimbra Horbe:** Writing – review & editing, Writing – original draft, Visualization, Validation, Supervision, Resources, Methodology, Data curation, Conceptualization. **Luis Felipe Soares Cherem:** Writing – review & editing, Writing – original draft, Supervision, Methodology.

Declaration of competing interest

The authors declare the following financial interests/personal relationships which may be considered as potential competing interests: Rodrigo Tokuta Castro reports financial support was provided by National Council for Scientific and Technological Development. Rodrigo Tokuta Castro reports financial support was provided by Coordination of

Higher Education Personnel Improvement.

Data availability

No data was used for the research described in the article.

Acknowledgments

The authors thank Universidade de Brasília for the technical and physical support, and for Coordenação de Aperfeiçoamento de Pessoal de Nível Superior (CAPES) (Code 001) and Conselho Nacional de Desenvolvimento Científico e Tecnológico (CNPq) (grant nº 168367/2018-1) for financial support.

Appendix A. Supplementary data

Supplementary data related to this article can be found at <https://doi.org/10.1016/j.jsames.2022.103959>.

References

- Ab'sáber, A.N., 2000. Summit surfaces in Brazil. *Rev. Bras. Geociencias* 30, 515–516.
- Allard, T., Gautheron, C., Bressan Riffel, S., Balan, E., Soares, B.F., Pinna-Jamme, R., Derycke, A., Morin, G., Bueno, G.T., do Nascimento, N., 2018. Combined dating of goethites and kaolinites from ferruginous duricrusts. Deciphering the Late Neogene erosion history of Central Amazonia. *Chem. Geol.* 479, 136–150. <https://doi.org/10.1016/j.chemgeo.2018.01.004>.
- Almeida, F.F.M., Hasui, Y., Brito Neves, B.B., Fuck, R.A., 1981. Brazilian structural provinces: an introduction. *Earth Sci. Rev.* 17, 1–29. [https://doi.org/10.1016/0012-8252\(81\)90003-9](https://doi.org/10.1016/0012-8252(81)90003-9).
- Assine, M.L., Merino, E.R., Pupim, F.N., Warren, L.V., Guerreiro, R.L., McGue, M.M., 2015. Geology and geomorphology of the Pantanal basin. C.R.: In: Warren, Lucas V., Quaglió, Fernanda, Simões, Marcello G., Freitas, Bernardo T., Assine, Mario L. (Eds.), Dynamics of the Pantanal Wetland in South America. Springer International Publishing, p. 28. https://doi.org/10.1007/998_2015_349.
- Bardossy, G., Aleva, G.J.J., 1990. Lateritic Bauxites. Lateritic bauxites. <https://doi.org/10.1346/ccmn.1991.0390116>.
- Batezelli, A., Ladeira, F.S.B., 2016. Stratigraphic framework and evolution of the Cretaceous continental sequences of the Bauru, Sanfranciscana, and Paracatu basins, Brazil. *J. South Am. Earth Sci.* 65, 1–24. <https://doi.org/10.1016/j.jsames.2015.11.005>.
- Bavil, A.Y., Bavil, K.Y., 2019. SCPAT: a MATLAB-based toolbox for analysing swath characteristic profiles. *Arabian J. Geosci.* 12, 282. <https://doi.org/10.1007/s12517-019-4437-6>.
- Beauvais, A., Chardon, D., 2013. Modes, tempo, and spatial variability of Cenozoic cratonic denudation: the West African example. *G-cubed* 14, 1590–1608. <https://doi.org/10.1002/ggpe.20093>.
- Beauvais, A., Ruffet, G., Hénocque, O., Colin, F., 2008. Chemical and physical erosion rhythms of the West African Cenozoic morphogenesis: the 39 Ar-40 Ar dating of

- supergene K-Mn oxides. *J. Geophys. Res. Earth Surf.* 113 <https://doi.org/10.1029/2008JF000996>.
- Bertolini, W.Z., Deodoro, S.C., Zambot, N., 2021. Análise morfométrica do relevo Da região hidrográfica da Várzea-Alto Rio Uruguay (Rs). *Geosciences* 40, 83–99.
- Bigarella, J.J., Mousinho, M.R., Silva, J.X., 1965. Pediplanos, Pedimentos e seus Depósitos Correlativos no Brasil. *Bol. Paraná. Geogr.* 16–17, 117–151.
- Bonnet, N.J., Beauvais, A., Arnaud, N., Chardon, D., Jayananda, M., 2014. First 40Ar/39Ar dating of intense Late Palaeogene lateritic weathering in Peninsular India. *Earth Planet Sci. Lett.* 386, 126–137. <https://doi.org/10.1016/j.epsl.2013.11.002>.
- Bonnet, N.J., Beauvais, A., Arnaud, N., Chardon, D., Jayananda, M., 2016. Cenozoic lateritic weathering and erosion history of Peninsular India from 40Ar/39Ar dating of supergene K-Mn oxides. *Chem. Geol.* 446, 33–53. <https://doi.org/10.1016/j.chemgeo.2016.04.018>.
- Boulangé, B., Carvalho, A., 1997. The bauxite of Ponte Tumbetas. In: Carvalho, A., Boulangé, B., Melfi, A.J., Lucas, Y. (Eds.), *Brazilian Bauxites*. USP/FAPESP/ORSTOM, São Paulo, pp. 55–73.
- Bourman, R.P., Ollier, C.D., 2002. A critique of the Schellmann definition and classification of 'laterite'. *Catena* 47, 117–131.
- Braucher, R., Lima, C.V., Bourles, D.L., Gaspar, J.C., Assad, M.L.L., 2004. Stone-line formation processes documented by in-situ-produced 10 Be distribution, Jardim River basin, DF, Brazil. *Earth Planet Sci. Lett.* 222, 645–651. <https://doi.org/10.1016/j.epsl.2004.02.033>.
- Braun, O.P.G., 1971. Contribuição à geomorfologia do Brasil Central. *Rev. Bras. Geogr. Rio de Janeiro* 32, 3–39.
- Brito Neves, B.B., Cordani, U.G., 1991. Tectonic evolution of South America during the late proterozoic. *Precambrian Res.* 53, 23–40. [https://doi.org/10.1016/0301-9268\(91\)90004-T](https://doi.org/10.1016/0301-9268(91)90004-T).
- Brito Neves, B.B., Fuck, R.A., Pimentel, M.M., 2014. The Brasiliano collage in South America: a review. *Braz. J. Geol.* 44, 493–518. <https://doi.org/10.5327/Z2317-4889201400030010>.
- Büdel, J., 1982. *Climatic Geomorphology*. Princeton Univ. Press, Princeton, p. 443p.
- Burke, K., Gunnell, Y., 2008. The African erosion surface : environmental change over the past 180 million years. *Geol. Soc. Am.* 1–66. <https://doi.org/10.1130/2008.1201>.
- Campos, J.E.G., Dardenne, M.A., 1997. Origem e evolução tectônica da Bacia sanfranciscana. *Rev. Bras. Geociências* 27, 283–294.
- Campos, J.E.G., Dardenne, M.A., Freitas-Silva, F.H., Martins-Ferreira, M.A.C., 2013. Geologia do Grupo Paranoá na porção externa da Faixa Brasília. *Braz. J. Geol.* 43, 461–476. <https://doi.org/10.5327/Z2317-48892013000300004>.
- Campos, J.E.G., Xavier, T.O., Freitas-Silva, F.H., 2016. Registros de atividade neotectônica no Distrito Federal. *São Paulo/UNESP/Geociências* 35, 203–219.
- Castro, D.L., Fuck, R.A., Phillips, J.D., Vidotti, R.M., Bezerra, F.H.R., Dantas, E.L., 2014. Crustal structure beneath the Paleozoic Parnaíba Basin revealed by airborne gravity and magnetic data. *Brazil. Tectonophy.* 614 <https://doi.org/10.1016/j.tecto.2013.12.009>.
- Catunaru, O., Wopfner, H., Eriksson, P.G., Cairncross, B., Rubidge, B.S., Smith, R.M.H., Hancock, P.J., 2005. The Karoo basins of south-central Africa. *J. Afr. Earth Sci.* 43, 211–253. <https://doi.org/10.1016/j.jafrearsci.2005.07.007>.
- Chardon, D., Grimaud, J., Beauvais, A., Bamba, O., 2018. West African lateritic pediments : landform-regolith evolution processes and mineral exploration pitfalls. *Earth Sci. Rev.* 179, 124–146. <https://doi.org/10.1016/j.earscirev.2018.02.009>.
- Colin, F., 1990. Lateritic weathering. *Econ. Geol.* 85, 1010–1023.
- Colin, F., Beauvais, A., Ruffet, G., Hénocque, O., 2005. First 40Ar/39Ar geochronology of lateritic manganeseiferous pisolithes: implications for the Palaeogene history of a West African landscape. *Earth Planet Sci. Lett.* 238, 172–188. <https://doi.org/10.1016/j.epsl.2005.06.052>.
- Correa, A.C.B., Monteiro, K.A., 2021. Revisitando as superfícies de aplanaimento: novos enfoques e implicações para a geomorfologia geográfica. *Humboldt – Rev. Geo. Fís e Meio Ambiente* 1, e57370.
- Costa, M.L., 1997. Lateritization as major process of ore deposit formation in the Amazon Region. *Explor. Min. Geol.* 6, 79–104.
- Costa, M.L., Fernandez, O.J.C., Requiem, M.E.R., 2005. O depósito de manganes do Azul, Carajás: estratigrafia, mineralogia, geoquímica e evolução geológica. In: Marini, O.J., Queiroz, E.T., Ramos, B.W. (Eds.), *Caracterização de Depósitos Minerais em Distritos Mineiros da Amazônia*. DNPM-CT/Mineral-ADIMB, Brasília, pp. 227–334.
- Costa, W.D., Siqueira, L., Dias, R.R., Pedrosa, V.A., Carry, L., Feitosa, E.C., Manoel Filho, J., Henrique, H.S., Santos, R.J.C., 2010. Estudos hidrogeológicos da região sudeste do estado do Tocantins. Relatório final elaborado pela COSTA Consultoria e Serviços Técnicos e Ambientais Ltda., para a SEMARH-Secretaria de Recursos Hídricos e Meio Ambiente do Estado de Tocantins, p. 291.
- Costa, M.L., da Cruz, G. da S., Almeida, H.D.F., de Poellmann, H., 2014. On the geology, mineralogy and geochemistry of the bauxite-bearing regolith in the lower Amazon basin: evidence of genetic relationships. *J. Geochem. Explor.* 146, 58–74. <https://doi.org/10.1002/2013JB010593>.
- Curto, J.B., Vidotti, R.M., Fuck, R.A., Blakely, R.J., Alvarenga, C.J.S., Dantas, E.L., 2014. The tectonic evolution of the Transbrasiliana Lineament in northern Parana Basin, Brazil, as inferred from aeromagnetic data. *J. Geophys. Res. Solid Earth* 119. <https://doi.org/10.1002/2013JB010593>.
- Dammer, D., McDougall, I., Chivas, A.R., 1999. Timing of weathering-induced alteration of manganese deposits in Western Australia: evidence from K/Ar and 40Ar/39Ar dating. *Econ. Geol.* 94, 87–108. <https://doi.org/10.2113/gsecongeo.94.1.87>.
- Dardenne, M.A., 2000. The Brasília fold belt. In: Cordani, U.G., Milani, E.J., Thomaz Filho, A., Campo, D.A. (Eds.), *Tectonic Evolution of South America*, pp. 231–264.
- Davis, M., Kuznir, N.J., 2004. Depth-dependent lithospheric stretching at rifted continental margins. In: KARNER, G.D. (Ed.), *Proceedings of NSF Rifted Margins*. Theoretical Institute, New York, pp. 92–136.
- De Martonne, E., 1943. Problemas morfológicos do Brasil tropical Atlântico. *Rev. Bras. Geogr.* 4, 523–550.
- De Putter, T., Ruffet, G., 2020. Supergene manganese ore records 75 Myr-long Campanian to Pleistocene geodynamic evolution and weathering history of the Central African Great Lakes Region – tectonics drives, climate assists. *Gondwana Res.* 83, 96–117. <https://doi.org/10.1016/j.gr.2020.01.021>.
- Deng, X.D., Li, J.W., Vasconcelos, P.M., 2016. 40Ar/39Ar dating of supergene Mn-oxides from the Yunyi Mn deposit, Guizhou Plateau, SW China: implications for chemical weathering and paleoclimatic evolution since the late Miocene. *Chem. Geol.* 445 <https://doi.org/10.1016/j.chemgeo.2016.02.009>.
- dos Santos Albuquerque, M.F., Horbe, A.M.C., Danišk, M., 2020. Episodic weathering in Southwestern Amazonia based on (U/Th)/He dating of Fe and Mn lateritic duricrust. *Chem. Geol.* 553 <https://doi.org/10.1016/j.chemgeo.2020.119792>, 119792.
- Flament, N., Gurnis, M., Dietmar Müller, R., 2013. A review of observations and models of dynamic topography. *Lithosphere* 5, 189–210. <https://doi.org/10.1130/L245.1>.
- Flament, N., Gurnis, M., Müller, R.D., Bower, D.J., Husson, L., 2015. Influence of subduction history on South American topography. *Earth Planet Sci. Lett.* 430, 9–18. <https://doi.org/10.1016/j.epsl.2015.08.006>.
- Fonseca, A.C.L., Novo, T.A., Nachtergaele, S., Fonte-Boa, T.M.R., Van Ranst, G., De Grave, J., 2021. Differential Phanerozoic evolution of cratonic and non-cratonic lithosphere from a thermochronological perspective: São Francisco Craton and marginal orogens (Brazil). *Gondwana Res.* 93, 106–126. <https://doi.org/10.1016/j.gr.2021.01.006>.
- Freitas, R.O., 1951. Relevos policíclicos na tectônica do escudo brasileiro. *Boletim Paul. Geogr.* 7, 3–19.
- Fuck, R.A., Jardim de Sa, E.F., Pimentel, M.M., Dardenne, M.A., Soares, A.C.P., 1994. As faixas de dobramento marginais do Cratão do São Francisco: síntese dos conhecimentos. In: Dominguez, J.M.L., Misí, A. (Eds.), *O Cratão Do São Francisco*. SBG-SGM-CNpq, Salvador, pp. 161–185.
- Fuck, R.A., Pimentel, M.M., Alvarenga, C.J.S., Dantas, E.L., 2017. The northern Brasília belt. In: Hellbron, M., Cordani, U.G., Alkmim, F.F., Orgs (Eds.), *Regional Geology Reviews*, pp. 205–220. https://doi.org/10.1007/978-3-319-01715-0_11.
- Grimaud, J., Chardon, D., Metelka, V., Beauvais, A., Bamba, O., 2015. Neogene cratonic erosion fluxes and landform evolution processes from regional regolith mapping (Burkina Faso, West Africa). *Geomorphology* 241, 315–330. <https://doi.org/10.1016/j.geomorph.2015.04.006>.
- Guadagnin, F., Chemaney, F., 2015. Detrital zircon record of the paleoproterozoic to mesoproterozoic cratonic basins in the São Francisco craton. *J. South Am. Earth Sci.* 60, 104–116.
- Guillocheau, F., Simon, B., Baby, G., Bessin, P., Robin, C., Dauteuil, O., 2017. Planation surfaces as a record of mantle dynamics: the case example of Africa. *Gondwana Res.* 53, 82–98. <https://doi.org/10.1016/j.gr.2017.05.015>.
- Hanson, E.K., Moore, J.M., Bordy, E.M., Marsh, J.S., Howarth, G., Robey, J.V.A., 2009. Cretaceous erosion in central South Africa: evidence from upper-crustal xenoliths in kimberlite diatremes. *South African J. Geol.* 112, 125–140. <https://doi.org/10.2113/gsa.2009.3112.125>.
- Heller, B.M., Bressan, S., Allard, T., Aertgeerts, G., Morin, G., Roig, J., Coue, R., Derycke, A., Ansart, C., Pinna-jamme, R., 2022. ScienceDirect Reading the climate signals hidden in bauxite. *Geochim. Cosmochim. Acta* 323, 40–73. <https://doi.org/10.1016/j.gca.2022.02.017>.
- Hénocque, O., Ruffet, G., Colin, F., Ferraud, G., 1998. 40Ar/39Ar dating of West African lateritic cryotomelanes. *Geochim. Cosmochim. Acta* 62, 2739–2756. [https://doi.org/10.1016/S0016-7037\(98\)00185-9](https://doi.org/10.1016/S0016-7037(98)00185-9).
- Hoorn, C., Wesselingsh, F.P., ter Steege, H., Bermudez, M.A., Mora, A., Sevink, J., Sanmartín, I., Sanchez-Meseguer, A., Anderson, C.L., Figueiredo, J.P., Jararilla, C., Riff, D., Negri, F.R., Hooghiemstra, H., Lundberg, J., Stadler, T., Sarkinen, T., Antonelli, A., 2010. Amazonia through time : Andean Science 80–330, 927–931. <https://doi.org/10.1126/science.1194585>.
- Hu, J., Liu, L., Faccenda, M., Zhou, Q., Fischer, K.M., Marshak, S., Lundstrom, C., 2018. Modification of the Western Gondwana craton by plume-lithosphere interaction. *Nat. Geosci.* 11, 203–210. <https://doi.org/10.1038/s41561-018-0064-1>.
- Jaiswara, N.K., Kotluri, S.K., Pandey, P., Pandey, A.K., 2020. MATLAB functions for extracting hypsometry, stream-length gradient index, steepness index, chi gradient of channel and swath profiles from digital elevation model (DEM) and other spatial data for landscape characterisation. *Appl. Comput. Geosci.* 7, 100033. <https://doi.org/10.1016/j.acgs.2020.100033>.
- Jean, A., Beauvais, A., Chardon, D., Arnaud, N., Jayananda, M., Mathe, P.E., 2019. Weathering history and landscape evolution of western ghats (India) from 40Ar/39Ar dating of supergene k-mn oxides. *J. Geol. Soc. London* 177, 523–536. <https://doi.org/10.1144/jgs2019-048>.
- King, L.C., 1953. Canons of landscape evolution. *Bull. Geol. Soc. Am.* 64, 721–752. [https://doi.org/10.1130/0016-7606\(1953\)64<721:COLE>2.0.CO;2](https://doi.org/10.1130/0016-7606(1953)64<721:COLE>2.0.CO;2).
- King, L.A., 1956. Geomorfologia do Brasil oriental. *Rev. Bras. Geociências* 18, 147–256.
- Kotschoubey, B., Truckenbrodt, W., Calaf, J.M.C., 2005. Evolução Geológica da Porção Meridional da Província Bauxitífera de Paragominas durante o Neógeno/Pleistoceno (Nordeste da Bacia do Grajaú, Nordeste do Pará e Extremo oeste do Maranhão). *Bras. J. Geol.* 35, 263–272.
- Kusznir, N.J., Karner, G.D., 2007. Continental lithospheric thinning and breakup in response to upwelling divergent mantle flow: application to the Woodlark, Newfoundland and Iberia margins. *Geol. Soc. Spec. Publ.* 282, 389–419. <https://doi.org/10.1144/GSP282.16>.
- Latrubesse, T.M. de C., 2006. Geomorfologia Goiás e Distrito Federal. *Série Geol. e Mineração* 2, 132.
- Leonardi, F.A., Ladeira, F.S.B., dos Santos, M., 2011. Paleosurfaces and bauxite profiles in the Poco das Caldas plateau, São Paulo/Minas Gerais, Brazil. *Geociências* 30, 147–160.

- Lima, M.d.a G., 2008. A História do Intemperismo na Província Borborema Oriental , Nordeste do Brasil : Implicações Paleoclimáticas e Tectónicas. Unpublished PhD thesis. Universidade Federal do Rio Grande do Norte, 594p.
- Loeterbach, M., Roddaz, M., Antoine, P.-O., Marivaux, L., Adnet, S., Baileul, J., Dantas, E., Santos, R.V., Chemale, F., Baby, P., Sanchez, C., Calderon, Y., 2017. Provenance record of late Maastrichtian-late Palaeocene Andean Mountain building in the Amazonian forearc foreland basin (Madre de Dios basin, Peru). Terra Nov 30, 17–23. <https://doi.org/10.1111/ter.12303>.
- Lucas, Y., 1997. The bauxite of Juriti In: Carvalho, A., Boulangé, B., Melfi, A.J., Lucas, Y. (Eds.), Brazilian Bauxites. USP/FAPESP/ORSTOM, São Paulo, pp. 107–133.
- Magee, C., Bastow, I.D., de Vries, B., van W., Jackson, C.A.L., Hetherington, R., Hagos, M., Hoggett, M., 2017. Structure and dynamics of surface uplift induced by incremental sill emplacement. Geology 45, 431–434. <https://doi.org/10.1130/G38839.1>.
- Maizatto, J.R., 2001. Análise bioestratigráfica, paleoecológica e sedimentológica das bacias terciárias do Gondárea e Fonseca - Quadrilátero Ferrifero - Minas Gerais, com base em aspectos palinológicos e sedimentares. PhD Thesis. Universidade de Ouro Preto, p. 249.
- Mamede, L., Nascimento, M.A.L.S. do, Franco, M.S.M. Geomorfologia, 1981a. Folha SD.22 Goiás: geologia, geomorfologia, pedologia, vegetação. Rio de Janeiro: Radam, Projeto Radambrasil. Levant. Recur. Nat. 25, 635.
- Mamede, L., Ross, J.L.S., Santos, L. M. dos, 1981b. Geomorfologia. In: BRASIL. Ministério das Minas e Energia. Folha SC.22 Tocantins, vol. 22. Projeto Radambrasil, Levantamento de Recursos Naturais, Rio Janeiro, p. 523.
- Marangoni, Y.R., Mantovani, M.S.M., 2013. Geophysical signatures of the alkaline intrusions bordering the Paraná Basin. J. South Am. Earth Sci. 41 <https://doi.org/10.1016/j.james.2012.08.004>.
- Margirier, A., Braun, J., Gautheron, C., Carcaillet, J., Schwartz, S., Pinna Jamme, R., Stanley, J., 2019. Climate control on Early Cenozoic denudation of the Namibian margin as deduced from new thermochronological constraints. Earth Planet Sci. Lett. 527, 115779. <https://doi.org/10.1016/j.epsl.2019.115779>.
- Martins, E.S., Baptista, G.M.M., 1999. Compartimentação geomorfológica do Distrito Federal. Inventário hidrogeológico e dos recursos hídricos superficiais do DF. Brasília: SEMATEC, MMA-SRH, Cap. 2, 51.
- Martins, E. de S., Reatto, A., Carvalho Jr., O., Guimarães, R., 2004. Evolução Geomorfológica Do Distrito Federal. Embrapa Cerrados, p. 57.
- Mathian, M.A.C., Campos, J.E.G., 2017. Compartimentação geomorfológica como suporte para Estudos de evolução geotectônica: Aplicação Na região Da Chapada dos Veadeiros. Go. Rev. Bras. Geomorfol. 18 <https://doi.org/10.20502/rbg.v18i3.1119>.
- Mathian, M., Aufort, J., Braun, J.J., Riotti, J., Selo, M., Balan, E., Fritsch, E., Bhattacharya, S., Allard, T., 2019. Unraveling weathering episodes in Tertiary regoliths by kaolinite dating (Western Ghats, India). Gondwana Res. 69, 89–105. <https://doi.org/10.1016/j.gr.2018.12.003>.
- Melfi, A.J., 1997. Brazilian bauxite deposits: a review. In: Carvalho, A., Boulangé, B., Melfi, A.J., Lucas, Y. (Eds.), Brazilian Bauxites. USP/FAPESP/ORSTOM, São Paulo, pp. 3–22.
- Monteiro, H.S., Vasconcelos, P.M., Farley, K.A., Spier, C.A., Mello, C.L., 2014. U-Th/He geochronology of goethite and the origin and evolution of canangs. Geochim. Cosmochim. Acta 131, 267–289. <https://doi.org/10.1016/j.gca.2014.01.036>.
- Monteiro, H.S., Vasconcelos, P.M.P., Farley, K.A., Lopes, C.A.M., 2018. Age and evolution of diachronous erosion surfaces in the Amazon: combining (U-Th)/He and cosmogenic 3He records. Geochim. Cosmochim. Acta 229, 162–183. <https://doi.org/10.1016/j.gca.2018.02.045>.
- Moraes, J.M., 2014, 2014. In: Moraes, J.M. (Ed.), Geodiversidade do Estado de Goiás e do Distrito Federal. CPRM, Goiânia, p. 131.
- Moraes Neto, J.M., Hegarty, K.A., Karner, G.D., Alkmim, F.F., 2009. Timing and mechanisms for the generation and modification of the anomalous topography of the Borborema Province, northeastern Brazil. Mar. Pet. Geol. 26, 1070–1086. <https://doi.org/10.1016/j.marpgeo.2008.07.002>.
- Moreira, L.H., 1995. Zoneamento geomambiental e agroecológico do Estado de Goiás região norte. Rev. Bras. Geo. Rio de Janeiro 3, 230.
- Moura, V.H.S., 2019. Mineralogia e geoquímica de bauxitas de barro Alto (goiás): considerações genéticas. Dissertação de Mestrado, Instituto de Geociências, Universidade Federal do Pará, p. 83.
- Nascimento, M.A.L.S., 1991. Geomorfologia do Estado de Goiás. Bol. Goiano de Geografia, Goiânia 12, 22.
- Oliveira, S.M.B., Toledo, M.C., 1997. The bauxite of Nazaré Paulista and associated deposits. In: Carvalho, A., Boulangé, B., Melfi, A.J., Lucas, Y. (Eds.), Brazilian Bauxites. USP/FAPESP/ORSTOM, São Paulo, pp. 208–225.
- Oliveira, F.S., Varajão, A.F.D.C., Varajão, C.A.C., Boulangé, B., Gomes, N.S., 2011. Bauxitization of anorthosites from Central Brazil. Geoderma 167–168, 319–327. <https://doi.org/10.1016/j.geoderma.2011.09.006>.
- Oliveira, C.H.E., Jelinek, A.R., Chemale, F., Bermet, M., 2016. Evidence of post-Gondwana breakup in Southern Brazilian Shield: insights from apatite and zircon fission track thermochronology. Tectonophysics 666, 173–187. <https://doi.org/10.1016/j.tecto.2015.11.005>.
- Oliveira, S.B., Da Costa, M.L., Dos Prazeres Filho, H.J., 2016. The lateritic bauxite deposit of Rondon do Pará: a new giant deposit in the Amazon Region, Northern Brazil. Econ. Geol. 111 <https://doi.org/10.2113/econgeo.111.5.1277>.
- Ollier, C.D., Pain, C.F., 1996. Regolith, Soils and Landforms. John Wiley and Sons, Chichester.
- Peixoto, S.F., Horbe, A.M.C., Soares, T.M., Freitas, C.M., Sousa, E.M.D., Iza, E.R.H. de F., 2021. Boolean and fuzzy logic operators and multivariate linear regression applied to airborne gamma-ray spectrometry data for regolith mapping in granite-greenstone terrain in Midwest Brazil. J. South Am. Earth Sci. 112, 103562 <https://doi.org/10.1016/j.james.2021.103562>.
- Peyvast, J.P., Bétard, F., 2021. Morphostratigraphic constraints and low temperature thermochronology: lessons from a review of recent geological and geomorphological studies in northeast Brazil. J. South Am. Earth Sci. 111 <https://doi.org/10.1016/j.james.2021.103464>.
- Pidgeon, R.T., Brander, T., Lippolt, H.J., 2004. Late Miocene (U+Th)-4He ages of ferruginous nodules from lateritic duricrust, Darling Range, Western Australia. Aust. J. Earth Sci. 51 <https://doi.org/10.1111/j.1400-0952.2004.01094.x>.
- Pimentel, M.M., Fuck, R.A., Botelho, N.F., 1999. Granites and the geodynamic history of the Neoproterozoic Brasilian belt, Central Brazil: a review. Lithos 46, 463–483. [https://doi.org/10.1016/S0024-4937\(98\)00078-4](https://doi.org/10.1016/S0024-4937(98)00078-4).
- Pimentel, M.M., Rodrigues, J.B., DellaGiustina, M.E.S., Junges, S., Matteini, M., Armstrong, R., 2011. The tectonic evolution of the Neoproterozoic Brasilian Belt, central Brazil, based on SHRIMP and LA-ICPMS U-Pb sedimentary provenance data: a review. J. South Am. Earth Sci. 31, 345–357. <https://doi.org/10.1016/j.james.2011.02.011>.
- Price, G.D., Valdes, P.J., Sellwood, B.W., 1997. Prediction of modern bauxite occurrence: implications for climate reconstruction Gregory. Palaeogeogr. Palaeoclimatol. Palaeoecol. 131, 1–13.
- Retallack, G.J., 2010. Lateritization and bauxitization events. Econ. Geol. 105, 655–667. <https://doi.org/10.2113/gsgecon.105.3.655>.
- Ribeiro, P.S.E., 2017. Geologia E Recursos Minerais Da Região De Palmas – Folhas Miracema Do Norte Sc . 22-Z-D Porto Nacional Sc . 22-Z-B E Santa Teresinha Sc . 22-Z-A. CPRM.
- Ribeiro, A.C., Riccomini, C., Leite, J.A.D., 2018. Origin of the largest South American transtectonic water divide. Sci. Rep. 8, 1–8. <https://doi.org/10.1038/s41598-018-35546>.
- Roddaz, M., Viers, J., Brusset, J., Baby, P., Héral, G., 2005. Sediment provenances and drainage evolution of the Neogene Amazonian foreland basin. Earth Planet Sci. Lett. 239, 57–78. <https://doi.org/10.1016/j.epsl.2005.08.007>.
- Rodrigues, J.B., Pimentel, M.M., Dardenne, M.A., Armstrong, R.A., 2010. Age, provenance and tectonic setting of the Canastra and Ibiti groups (Brasilian belt, Brazil): implications for the age of a Neoproterozoic glacial event in central Brazil. J. South Am. Earth Sci. 29, 512–521. <https://doi.org/10.1016/j.james.2009.08.008>.
- Ruffet, G., Innocent, C., Michard, A., Féraud, G., Beauvais, A., Nahon, D., Hamelin, B., 1996. A geochronological 40Ar/39Ar and 87Rb/87Sr study of K-Mn oxides from the weathering sequence of Azul Brazil. Geochim. Cosmochim. Acta 60, 2219–2232.
- Saadi, A., 1993. Neotectônica da Plataforma Brasileira: esboço e interpretação preliminares. Geonomos 1, 1–15. <https://doi.org/10.18285/geonomos.v1i1.e2.233>.
- Saadi, A., Bezerra, F.H.R., Costa, R.D., Iglesia, H.L.S., Franzinelli, E., 2005. Neotectônica da Plataforma Brasileira. In: Souza, C.R.G., Suguio, K., Oliveira, A.M.S., Oliveira, P. E. (Eds.), Quaternário Do Brasil. Holo Editora, pp. 211–234. Ribeirão Preto.
- Salgado, A.A.R., 2007. Superfícies de aplanaimento: antigos paradigmas revistos pela ótica dos novos conhecimentos geomorfológicos. Rev. Geogr. 3, 64–78.
- Salgado, A.A.R., Bueno, G.T., Diniz, A.D., Marenz, B.R., 2015. Long-term geomorphological evolution of the Brazilian Territory. In: World Geomorphological Landscapes. https://doi.org/10.1007/978-94-017-8023-0_3.
- Sampaio, T.V.M., Augustin, C.H.R.R., 2014. Índice de concentração da rugosidade: uma nova proposta metodológica para o mapeamento e quantificação da dissecação do relevo como subsídio a cartografia geomorfológica. Rev. Bras. Geomorfol. 15 <https://doi.org/10.20502/rbg.v15i1.376>.
- Schellmann, W., 1983. A new definition of laterite. Geological Survey of India. Memoires Nat. Resour. Dev. 18, 7–21.
- Schobbenhaus, et al., 1975. Carta Geológica Do Brasil Ao Milionésimo; Folha Goiás (SD.22), MME/DGM/DNPM, Brasília, p. 144.
- Shuster, D.L., Vasconcelos, P.M., Heim, J.A., Farley, K.A., 2005. Weathering geochronology by (U-Th)/He dating of goethite. Geochim. Cosmochim. Acta 69, 659–673. <https://doi.org/10.1016/j.gca.2004.07.028>.
- Silva, F., Silva, T., 2018. Perfil de Relevo em Variadura: procedimentos automáticos utilizando sistemas de informação geográfica. Rev. Bras. Cartogr. 70, 846–866. <https://doi.org/10.14393/rbcv70n3-45704>.
- Silva, T.A., Rodrigues Salgado, A.A.A., Rodrigues de Souza, F.C., 2019. Morfogênese do interflúvio Tocantins/São Francisco na região do Rio Paranaí. Rev. Bras. Geomorfol. 20 <https://doi.org/10.20502/rbg.v20i2.1514>.
- Souza, M.V., Coimbra Horbe, A.M., Costa da Silva, B., Peixoto, S.F., Castro, R.T., 2021. Regolith LANDSAT-8/OLI and Hyperion/EO-1 images classification in midwest of Brazil. J. South Am. Earth Sci. 111 <https://doi.org/10.1016/j.james.2021.103460>.
- Spier, C.A., Vasconcelos, P.M., Oliveira, S.M.B., 2006. 40Ar/39Ar geochronological Constraints on the evolution of lateritic iron deposits in the Quadrilátero Ferrifero, Minas Gerais, Brazil. Chem. Geol. 234, 79–104.
- Stanley, J.R., Flowers, R.M., Bell, D.R., 2013. Kimberlite (U-Th)/He dating links surface erosion with lithospheric heating, thinning, and metasomatism in the southern African Plateau. Geology 41, 1243–1246. <https://doi.org/10.1130/G34797.1>.
- Summerfield, M.A., 1991. Global Geomorphology. Longman Scientific & Technical, p. 537.
- Tardy, Y., Roquin, C., 1998. Dérive des continents, Paléoclimats et alterations tropicales. BRGM, Orléans.
- Thomas, E., 1995. Geomorphic Response to Rapid Climatic and Hydrologic Change during the Late Pleistocene and Early Holocene in the Humid and Sub-humid Tropics. vol. 14, pp. 193–207.
- Thomas, M.F., 2008. Understanding the impacts of Late Quaternary climate change in tropical and sub-tropical regions. Geomorphology 101, 146–158. <https://doi.org/10.1016/j.geomorph.2008.05.026>.
- Twidale, C.R., Bourne, J.A., 1998. The use of duricrusts and topographic relationships in geomorphological correlation: conclusions based in Australian experience. Catena 33, 105–122. [https://doi.org/10.1016/S0341-8162\(98\)00065-4](https://doi.org/10.1016/S0341-8162(98)00065-4).

- USGS. Earth explorer. <https://earthexplorer.usgs.gov/>. (Accessed 1 August 2018).
- Valadão, R.C., 2009. Geodinâmica de superfícies de aplanamento, desnudação continental e tectônica ativa como condicionantes da megaegeomorfologia do Brasil oriental. Rev. Bras. Geomorfol. 10, 77–90. <https://doi.org/10.20502/rbg.v10i2.132>.
- Valeton, I., Beissner, H., Carvalho, A., 1991. The Tertiary bauxite belt on tectonic uplift areas in the Serra da Mantiqueira, SouthEast Brazil. In: Fuchtbauer, H., Lisitzin, A., Milliman, J.D., Seibold, E. (Eds.), Contributions to Sedimentology. E. Schweizerbart'sche Verlagbuchhandlung, Stuttgart, pp. 1–99.
- Vasconcelos, P.M., 1999. K-Ar and 40Ar/39Ar geochronology of weathering processes. Annu. Rev. Earth Planet Sci. 27 <https://doi.org/10.1146/annurev.earth.27.1.183>.
- Vasconcelos, P.M., Carmo, I. de O., 2018. Calibrating denudation chronology through 40Ar/39Ar weathering geochronology. Earth Sci. Rev. 179, 411–435. <https://doi.org/10.1016/j.earscirev.2018.01.003>.
- Vasconcelos, P.M., Renne, P.R., Brimhall, G.H., Becker, T.A., 1994. Direct dating of weathering phenomena by 40Ar/39Ar and K-Ar analysis of supergene K-Mn oxides. Geochem. Cosmochim. Acta 58, 1635–1665. [https://doi.org/10.1016/0016-7037\(94\)90565-7](https://doi.org/10.1016/0016-7037(94)90565-7).
- Vidotti, R.M., Ebinger, C.J., Fairhead, J.D., 1998. Gravity signature of the western Paraná basin, Brazil. Earth Planet Sci. Lett. 159 [https://doi.org/10.1016/S0012-821X\(98\)00070-3](https://doi.org/10.1016/S0012-821X(98)00070-3).
- Wells, M.A., Daníšk, M., McInnes, B.I.A., Morris, P.A., 2019. U-Th/He-dating of ferruginous duricrust: insight into laterite formation at Boddington, WA. Chem. Geol. 522, 148–161. <https://doi.org/10.1016/j.chemgeo.2019.05.030>.
- Ye, J., Chardon, D., Rouby, D., Guillocheau, F., Dall'asta, M., Ferry, J.N., Broucke, O., 2017. Paleogeographic and structural evolution of northwestern Africa and its Atlantic margins since the early Mesozoic. Geosphere 13, 1254–1284. <https://doi.org/10.1130/GES01426.1>.
- Zachos, J., Pagani, H., Sloan, L., Thomas, E., Billups, K., 2001. Trends, rhythms, and aberrations in global climate 65 Ma to present. Science (80-) 292, 686–693. <https://doi.org/10.1126/science.1059412>.

CAPÍTULO 5

**ARTIGO 2: CENOZOIC EVOLUTION OF
REGOLITH CRATONIC FROM A
THERMOCHRONOLOGICAL
PERSPECTIVE: INSIGHTS FROM
APATITE FISSION TRACK
THERMOCHRONOLOGY – em prepação**

5 CENOZOIC EVOLUTION OF CRATONIC REGOLITH: INSIGHTS FROM THERMOCHRONOLOGICAL APATITE FISSION TRACK PERSPECTIVE

Rodrigo Tokuta Castro^{a*}; Mauricio Parra^b; Adriana Maria Coimbra Horbe^a; Elton Luiz Dantas^a; Peter Christian Hackspacher^c

a Universidade de Brasília, Instituto de Geociências, Campus Universitário Darcy Ribeiro, Distrito Federal, Brasília, 70910-900, Brazil.

E-mails: *castrortokuta@gmail.com; ahorbe@unb.br ; elton@unb.br ;

b Universidade de São Paulo, Instituto de Geociências, São Paulo, São Paulo, 05508010, Brazil.

E-mail: mparra@iee.usp.br ;

c Universidade Estadual Paulista Júlio de Mesquita Filho, Instituto de Geociências e Ciências Exatas, São Paulo, Rio Claro, 13506-900, Brazil.

E-mail: peter.hackspacher@unesp.br ; IN MEMORIAM

1. INTRODUCTION

In central Brazil, the Tocantins Province (Almeida et al. 1981) is a large Neoproterozoic orogen that resulted from the collision of the Amazonian, São Francisco, and Paranapanema paleocontinents during the Brasiliano/Pan African cycle, as part of West Gondwana amalgamation (Pimentel et al. 1999, 2004).

Elevated areas are typical of tectonically active regions, either within or near plate boundaries or in locations where tectonic activity has occurred recently with tectonic quiescence no more than a few tens of millions of years. This is because, on the geological time scale, erosion is a relatively rapid process, resulting in significant flattening and lowering of elevated areas, over time in millions of years, if surface elevation is inactive for that long (Martins-Ferreira et al., 2020). During the evolution of the continental lithosphere, strength plays a significant role in controlling the initiation and the extensional and compressional deformation character (Kusznir and Park, 1984). Rifting, tectonic reactivation, and reworking are mainly concentrated in segments of weak lithospheres and pre-existing shear zones (Manatschal et al., 2015; Petersen and Schiffer, 2016; Schiffer et al., 2019; Tommasi and Vauchez, 1997). In contrast, rigid and stiff lithosphere, such as cratons characteristic, is more resilient to tectonic events (Artemieva, 2006).

The West Gondwana break-up during the Early Cretaceous seems to have followed the structural lineaments of ancient regional mobile belts (e.g. Araçuaí belt) (Tommasi and Vauchez, 2001; Autin et al., 2013; Reuber and Mann, 2019; Will and Frimmel, 2018). It is believed that the Tocantins Province orogen during the Brasiliano cycle had similar modern Himalayas dimensions. However, intense erosional and denudational processes results in a dissected

plateaus and tablelands surface with altitudes between 600 and 1600 m.s.l. (Martins-Ferreira et al., 2017). In several areas along the Tocantins Province and the São Francisco Craton boundary, particularly where the rocks are more susceptible to erosion, the Brasília and Araguaia belt are being dissected until today (Milani et al., 2007; Salgado et al., 2015) where four Neogene lateritic surfaces were identified (Castro et al. 2022).

However, despite being located in a cratonic domain, the tectonic quiescence and favourable climatic conditions for the formation of lateritic bauxites (Price et al., 1997), only hydrothermal bauxites have been identified in this region (Valeton et al., 1991; Moura, 2019). Low-temperature apatite and zircon fission track thermochronology due to its ability to identify cooling/heating episodes that affected the shallow crust, has been used to constrain reactivations in tectonic environments (e.g. Fernie et al., 2018; Gillespie et al., 2017; Mackintosh et al., 2019) to reconstruct the timing and rate of heating and cooling at temperatures ~50°C to ~320°C (Chew and Spikings 2015; Tagami 2005), as well as the influence in the landscape evolution (Gallagher, 2012). We use apatite fission track thermal modelling to investigate cooling/heating episodes and the possible influence of these processes on the evolution of the Brazilian Midwest regolith.

2. GEOLOGICAL SETTING OF TOCANTINS PROVINCE

The Tocantins Province (Almeida et al., 1981) is an extensive Brasiliano/Pan-African orogen of the South American Platform formed by the collision between the Amazonian, São Francisco/Congo, West African/São Luís and Paranapanema cratons that resulted in the amalgamation of the Western Gondwana supercontinent in the Neoproterozoic (Brasiliano orogeny). The province is composed of three Neoproterozoic fold belts: the Paraguay, Araguaia and Brasília belts (Pimentel et al., 2000a), in this work, only rocks from the Araguaia and Brasilia belts are found. The area is crossed by the Transbrasiliano Lineament (TBL), a major lithospheric discontinuity in the region, which defines the boundary of different crustal domains (Cordani and Sato, 1999; Cordani et al., 2013; Brito Neves and Fuck, 2014).

The Araguaia Belt comprises the central and northern parts of the Tocantins Province (Fig. 1). Along its eastern boundary, the belt is covered by sedimentary rocks of the Paleozoic-Mesozoic Parnaíba basin. This basin covers a rigid lithosphere block, which probably represents its cratonic core (Brito Neves et al., 1984; Castro et al., 2014; Daly et al., 2014). In the western portion by granitoids of the Amazonian Craton. To the southeast, the belt is delimited by the Goiás Massif.

The Brasília Belt borders the western margin of the São Francisco Craton and is one of the most important and preserved Brasiliano orogens of the South American Platform. This belt as an elongated shape in the north-south direction, extending over 1000 km in the central-northern portion of the Brazil (Dardenne, 2000; Fuck et al., 2014; Pimentel, 2016). The Brasília Belt is

formed by External Domain, Passive Margin, Internal Domain and Goiás Magmatic Arc, (Pimentel and Fuck, 1992; Pimentel et al., 2000; Valeriano et al., 2008; Fuck et al., 2014, 2017; Pimentel, 2016; Cordeiro and Oliveira, 2017; Cuadros et al., 2017a).

The External Domain comprises the basement formed by metasedimentary rocks from Ticunzal Formation, the granites from Aurumina and Pedra Branca Suites (Alvarenga et al., 2007; Tanizaki et al., 2015; Cuadros et al., 2017b), and Araí, Paranoá and Bambuí groups (Fuck et al., 2014; Pimentel, 2016). These rocks overlie the basement units, covering an area of approximately 10,000 km² in the northeast of Goiás and southeast of Tocantins states (Dardenne, 2000; Alvarenga et al., 2007; Pimentel, 2016; Tanizaki et al., 2015; Cordeiro and Oliveira, 2017; Martins-Ferreira et al., 2018).

The Passive Margin is formed by metasedimentary rocks from Vazante, Paranoá, Canastra, Andrelândia, and Ibiá Groups (Fuck et al., 2014; Pimentel, 2016; Pimentel et al., 2004; Valeriano et al., 2004, 2008) (Fig. 1). The Internal Domain comprises the Metamorphic Core and the Goiás Massif (Fuck et al., 2014; Pimentel, 2016). The metamorphic core comprises the Neoproterozoic metasedimentary rocks of the Araxá Group and the high-grade rocks of Anápolis–Itauçu Complex and the Goiás massif includes Archean granite-greenstone terrains and Paleoproterozoic orthogneiss, covered by the Paleoproterozoic Serra da Mesa Group (Fuck et al., 2017). The Goiás Magmatic Arc comprises Neoproterozoic orthogneiss terrains and volcanic-sedimentary sequences (Fuck et al., 2017) is divided into Mara Rosa (northern) and Arenópolis (south-southeastern) Magmatic Arcs (Cordeiro and Oliveira, 2017; Fuck et al., 2008, 2014; Laux et al., 2005; Pimentel and Fuck, 1994; Pimentel et al., 2000a, 2004; Pimentel, 2016; Valeriano et al., 2008).

Phanerozoic sedimentary rocks of the Parnaíba and Paraná basins cover the province on the north and south, respectively, these basins also cover older stable continental blocks, such as the so-called Parnaíba and Paranapanema blocks (Fuck et al., 2014, 2017). Post-Paleozoic alkaline magmatism intruded the provinces basement mainly in areas surrounding the Paraná basin and the Brasília Belt, three very similar intracratonic basins were developed in Cretaceous times: the Sanfranciscana, Parecis, and Bauru basins. The Brasília belt hosted several alkaline magmatic pulses between the late Cretaceous and Paleogene (Riccomini et al. 2005). The Sanfranciscana basin developed over the São Francisco Craton and shows the follow Mesozoic stratigraphy: a Lower Cretaceous fluvial-lacustrine sequence (Areado Group) and Upper Cretaceous sequences deposited in the eolian system (Urucuia Group), alluvial fans (Capacete Formation, Mata da Corda Group), and alkaline volcanic (Patos Formation, Mata da Corda group) (Campos and Dardenne 1997). Cretaceous and Cenozoic continental covers, standing out the Pantanal, the Araguaia plain (Almeida et al. 1981) and Sanfranciscan basin are pulses of younger sedimentation (Campos and Dardenne, 1997; Uhlein et al., 2011).

3. THERMOCHRONOLOGY DATA IN TOCANTINS PROVINCE

3.1. Tocantins Province data set

Tocantins province thermochronological data are strongly concentrated in the Brasília belt southern portion (Gallagher et al. 1994; Oliveira 2000; Tello Saenz et al. 2003; 2005; Hackspacher et al. 2004; 2007; Ribeiro et al. 2005a; 2005b; Doranti et al. 2008; Cogné et al. 2011; Doranti-Tiritan et al. 2014; Dias et al. 2017; Fonseca et al. 2020, 2021; Martins-Ferreira et al., 2020).

From these data, there are only two zircon fission track (ZFT) study, the first in the Araguaia belt (Dias et al. 2017) and the second in the Brasilia Belt (Martins-Pereira et al. 2020). Dias et al. (2017) identified in the Araguaia belt distinct ZTF age populations, the older one is related to an orogenic collapse in 498 ± 8 to 489 ± 15 Ma, an intermediate population in 345 ± 13 to 331 ± 8 Ma related to Gondwanides orogeny reactivation event followed by Parnaíba sedimentary deposits erosion. The younger ZTF populations 208 ± 10 to 197 ± 3 Ma is associated with a possible Lower Jurassic Mosquito magmatism reheating (Dias et al. 2017). The Martins-Pereira et al. (2020), recorded three distinct ZTF age populations on basement and metasedimentary rocks 1) The older one (549 ± 26 Ma to 519 ± 41 Ma) in the Neoproterozoic-Cambrian event, is probably related to the orogenic exhumation of the Brasilia Belt and thermal decay of West Gondwana assembly; 2) The intermediate data (398 ± 22 Ma to 328 ± 25 Ma, Devonian-Carboniferous event), are probably related to the Late Famatinian orogeny and early stages of the Gondwanide orogeny; 3) The younger (289 ± 15 Ma, Early Permian event) is linked to the Late Gondwanide orogeny. These results indicate that the supercontinents breakup might significantly affect the plate interior, especially along the ancient orogenic belts. Zircon data indicate thermal decay during and after the West Gondwana assembly (Martins-Pereira et al., 2020).

Fonseca et al. (2020) reveal a Devonian to Permian cooling period and correlate it to the final exhumation of the Brasília Belt, associated with the orogenic collapse and sediment influx to Paraná basin. Martins-Ferreira et al. (2020) reveal TFA data of from 77 ± 11 to 63 ± 2 Ma that are Cretaceous to Paleogene age related it to Pangea breakup according to these authors. Fonseca et. al (2021) show new AFT data from forty-three samples from the Brasília Belt, the São Francisco Craton (SFC) and the Araçuaí Belt, far from the passive margin of the Atlantic coast (~150 to 800 km). Three main periods of basement exhumation were identified by these authors: 1) a Paleozoic, recorded both by samples from the SFC and Brasília Belt; 2) an Early Cretaceous to Cenomanian, recorded by samples from the Araçuaí Orogen; and 3) a Late Cretaceous to Paleocene, inferred in samples from all domains.

In the Brasilia belt region, the Poços de Caldas plateau that was cut by Cretaceous alkaline intrusions (Riccomini, 2005), have AFT data reveal that the thermal effect of the magmatism emplacement was not strong enough to affect the close basement portions and leave any impression on AFT data (Gallagher et al. 1994, Cogné et al. 2011, Doranti et al. 2008; Doranti-Tiritan et al. 2014).

4. MATERIAL AND METHODS

4.1. Low-temperature thermochronology

The low-temperature thermochronology isotope geology focuses on the comprehension of the upper crust thermal history where morphotectonic processes take place, which can be used to reconstruct geological histories, based in the timing and rate of heating and cooling at temperatures ~50°C to ~320°C (Chew and Spikings 2015; Tagami 2005). The most consolidated and employed methods for investigating, includes a set of thermochronometric systems, being fission track (FT) analysis and (U-Th)/He thermochronometry, both in apatite and zircon crystals.

The FT is based on the accumulation of narrow damage trails (i.e., fission tracks) in uranium-rich mineral grains (e.g., apatite, zircon, titanite) and natural glasses, which form as a result of spontaneous nuclear fission decay of ^{238}U , from which the parent isotope splits into two positively charged high-energy nuclei. (Price and Walker 1963; Fleischer et al. 1975). The heavy ionized particles travel at high velocity through the insulating solid (detector) and shape an amorphous damaged channel. These defects in the crystal lattice are the fission tracks, and each one represents a fission-decay event.

The time elapsed since fission tracks began to accumulate is estimated by determining the density of accumulated tracks in a particular material in relation to the uranium content of that material. Polishing and chemical etching can be used to enlarge the fission tracks formed within a mineral in order to make them readily observable under an ordinary optical microscope (Price and Walker 1962). In apatite, newly-formed FTs have a total length of ca. 16 μm and shorten progressively at certain temperature ranges as response to healing of the crystallographic damage in a process called annealing (Wagner and Van den Haute, 1992). The fission tracks are totally annealed when the mineral is subjected to high temperatures; while below such temperature, the tracks are only slowly annealed in a way that they decrease in length with time (Green, 1988; Brown et al., 1990). For geological timescales (10⁶–10⁸ y), a temperature range at which such phenomena occurs is termed Partial Annealing Zone (PAZ); for apatite, annealing experiments estimate that the PAZ is between ~110-60 °C (Laslett et al., 1987). At lower temperatures, the annealing effect became less effective, and the tracks are mostly preserved. Thus, the fission tracks record the passage of the mineral by the PAZ and the residence time in this will influence the observable amount and the length distribution of the tracks. Such information is used to model the thermal history of the minerals and landscape evolution and their relationships related to cooling, uplift and exhumation (Ketcham, 2005; Gallagher, 2012; Malusà and Fitzgerald, 2018).

The power of fission tracks for geological investigations derives precisely from their thermal sensitivity. Fission-track methods are unique among thermochronometers in that upon formation each daughter product becomes a sensitive recorder of the thermal history its host mineral subsequently undergoes (Ketcham, 2019). If the temperature information in a large number of

tracks that formed over a long-time interval can be successfully recovered, that information can be integrated and merged with other geological constraints to ascertain detailed thermal histories (e.g., Green et al. 1989; Gallagher 1995, 2012; Issler 1996; Ketcham 2005).

Understanding the significance of FT age, length and Dpar distributions (Gleadow et al., 1986; Green et al., 1986; Gallagher, 2012) allows the reconstruction of thermal histories of a rock sample and can solve geological problems in tectonics, sedimentation and landscape evolution (Gallagher, 2012).

Along a geological section with EW direction that encompasses the Araguaia and Brasilia Belts and the São Francisco craton, a total of 10 samples were collected from gneiss and granite, prepared, and analyzed using the apatite fission-track method. Three samples from External Domain of the Brasília Belt, comprise Aurumina Suite, Natividade-Cavalcante block and Goiás Magmatic arc yielded sufficient apatites and data quality to study the thermal history of the Tocantins Province.

4.2. APATITE FISSION TRACK SAMPLE PREPARATION AND ANALYSIS

Analyses were performed in the Low-Temperature Thermochronology Laboratory at Instituto de Geociências of Universidade de São Paulo (IGc/USP). Apatite grains were separated by conventional crushing, sieving, magnetic, heavy liquid and hand-picking techniques and mounted in epoxy resin. Mounts were polished and etched using 5.5M HNO₃ at 21 °C for 20 s to reveal spontaneous fission tracks (Donelick et al. 2005). Apatite mounts were covered with mica sheets to obtain fission track ages using the external detector method (Gleadow, 1981). Neutron irradiation was performed at IPEN/CNEN nuclear reactor (São Paulo, Brazil), using a neutron fluence of ~ 9.0 E15 n/cm². After irradiation, mica detectors were etched with 40% HF for 45 min to reveal induced fission tracks. Fission track counting was performed in an Olympus SZX16 microscope at 1250x magnification. Fission track ages were calculated using the zeta calibration approach (Hurford, 1983) with a CN1 dosimeter glass and the Durango apatite age standard. At least 22 grains were counted per sample, except for one sample with 6 datable grains, two samples with 5 and 3 datable grains are discarded for modeling

At least hundred confined horizontal tracks were measured per sample (Gleadow et al., 1986; Gallagher et al., 1998). The track orientation relative to the c-axis was also measured so we used confined mean track length (MTL) for modelling (e.g., Ketchman et al., 2009). Concordant and discordant ages are reported as pooled or central ages, respectively, with percent variation (Galbraith, 1988). Throughout this study, fission track age errors are quoted at the 2σ confidence level and were derived by conventional method (Green, 1981 or Galbraith, 1988). The chi-square test ($P(\chi^2) \geq 5\%$) was used to quantify age

homogeneity (Galbraith, 1990) using the software “IsoplotR” (Vermeesch, 2018). The size of the etch-pit diameter parallel to the c axis (Dpar) was also determined, as it is a kinetic parameter used in thermal history modeling (Donelick et al., 1999; Ketcham et al., 1999; Donelick et al., 2005) at least four Dpar values were measured per crystal (Fig. 2).

4.3. THERMAL HISTORY MODELING

Thermal history inverse modelling consists in determining plausible time-temperature histories for individual samples that agree with the observations (i.e., Aft age and MTL distribution). It was used the QTQt 5.7 software for model the thermal history of each sample (Gallagher, 2012). This software employs a Bayesian trans-dimensional Markov Chain Monte Carlo (MCMC) approach (Sambridge et al., 2006; Gallagher et al., 2009), with the multi-kinetic annealing model of Ketcham et al. (2007) and Dpar values as kinetic parameter. It was opted to run models with a minimum of user-imposed constraints, to avoid a biased thermal history. To initiate the models, a large small t-T box was set with general time-temperature were set to 300 ± 300 Ma and 125 ± 125 °C, time corresponding to the medium and end of the Brasiliano/Pan- African cycle (de Almeida et al., 1981; Hasui, 2010), which in the Tocantins Province has evidence of accretionary processes, in addition to interaction between plates, with closure of oceans and collision between plates, as well as their metamorphic processes.

Constraints on the range of thermal histories are typically defined as regions of time-temperature space through which acceptable models must pass. These constraints may include a range on the present-day temperature of a sample in a borehole or at the surface, requiring a sedimentary sample to be at near-surface temperature at the time of deposition, or that a sample should be at an elevated temperature at the time of intrusion. If required, additional geological information can be incorporated into the modelling to further constrain the range of acceptable models (Gallagher, 2012).

4.4. DATA INTERPRETATION

Regions where AFT ages and MTL decrease systematically indicate that they come from gradually different temperatures, which can be converted into depth by adopting an acceptable geothermal gradient (Van der Beek et al., 1998). In this case, the thermal history recorded in the AFT system reflects the combined effect of denudation and lithospheric heating and cooling (Gleadow and Brown, 2000). Therefore, AFT data can be used to identify differential vertical movements through exhumation-induced cooling and heat flux changes, as this region experienced by Phanerozoic rifting, drifting and magmatism, during which the geothermal gradient oscillated.

5. RESULTS

The results from three apatite fission track (AFT) samples from the Tocantins Province (Brasília Orogen) are summarized in Table 1 and in Fig. 3. All analyses passed in the chi² test of homogeneity ($P(\chi^2)$). The AFT age results obtained, range from 178.5 ± 6.4 Ma (sample LIS-39A) to 154.5 ± 11.2 (sample A-42.1). Sample A-42.1 contained only 6 analysable apatite grains, therefore they are not used for in depth discussion, although they corroborate the results of the other samples (LIS-39A and LIS-49). The track-length distribution is unimodal and quasi symmetrical for all samples (Fig. 3). The mean track length (MTL) ranges from 10.17 ± 0.2 μm (sample LIS-39A) to 11.16 ± 0.1 μm (sample LIS-49) and Dpar measurements range from 1.04 to 1.85 μm .

5.1. Embasement

Sample LIS-49 is a gneiss from the Paleoproterozoic Aurumina Suite (crystalline basement, Goias Magmatic Arc) yielded an AFT age of 178.5 ± 6.4 Ma (76 grains from 4 samples from the same outcrop, Table 1). The age is concordant, that is, passed in the chi² test of homogeneity ($(P(\chi^2) = 8.2\%)$). The composite sample has a MTL of 11.16 ± 0.1 and a unimodal distribution (Fig. 3).

5.2. Goias Magmatic Arc

Sample LIS-39A and A-42.1 are gneiss and granite, respectively, from Paleoproterozoic Aurumina Suite and Neoproterozoic Oeste de Goiás Granite, respectively, that represent Goias Magmatic Arc crustal block, yielded an AFT age 178.5 ± 6.4 to 154.5 ± 11.2 Ma (22 grains from 2 samples from the same outcrop and 6 grains from only sample, respectively, Table 1). Both ages are concordant, with $(P(\chi^2)$ values of 9.4% and 59.8%, respectively. The samples have MTL of 10.17 ± 0.2 and 11.38 ± 0.543 , with an unimodal distribution.

5.3. Thermal modeling of data from External domain (northern Portion) of Brasilia Belt

For the thermal modelling of northern portion of the Brasilian Belt, we ran three models with monotonic cooling paths using QTQt program. This monotonic constrain with general time-temperature were set to 300 ± 300 Ma and 125 ± 125 °C, time corresponding to the medium and end of the Brasiliano/Pan-African. The thermochronometric data of all three samples are compatible with monotonic cooling throughout the Phanerozoic until 60-40°C until the Late Cretaceous (100-80 Ma), when reheating to a temperature of up to 80°C that lasted longer 20 to 10 Ma would have occurred, before final cooling to surface temperatures.

6. DISCUSSION

The FT data from zircon and apatite in the Tocantins Province show the follow data. ZFT data in the Araguaia Belt show central ages from 498 ± 8 to 489 ± 15 Ma, 345 ± 13 to 331 ± 8 Ma, and 208 ± 10 to 197 ± 3 Ma, are associated with orogenic collapse, Gondwanides orogeny and Mosquito

magmatism, respectively (Dias et al., 2017), while in the Brasilia Belt the central ages from 549 ± 26 to 519 ± 41 Ma, 398 ± 22 to 328 ± 25 Ma, and 289 ± 15 Ma are associated with Brasilia Belt exhumation, Famatinian orogeny and Gondwanides orogeny, respectively (Martins-Pereira et al., 2020).

AFT data show central ages from 386 ± 31 to 243 ± 13 Ma, and 331 ± 23 to 206 ± 15 Ma, relates with Brasilia Belt exhumation (Fonseca et al., 2020, 2021), while the central ages from 77 ± 11 from 63 ± 2 Ma are associated with Breaking of Pangea and/or Andean Orogeny (Martins-Ferreira et al., 2020) (Table 2)

The AFT age from this work, show new ranges from 178.51 ± 6.4 to 154.58 ± 11.2 Ma in the north portion of Brasilia Belt that are similar to the Fonseca et al., (2020, 2021), associated with slow Brasilia Belt exhumation, these data corroborate the ancient orogenic episodes well-known and described by Pimentel et al. (2000), Valeriano et al., (2008); Fuck et al., (2014, 2016); Pimentel, (2016).

The MTL ranges from 10.17 ± 0.2 μm to 11.16 ± 0.1 μm (Table 1), are shorter than those of Fonseca et al., (2020, 2021, $10.8 \mu\text{m}$ to $14.5 \mu\text{m}$). These shortening is consequence of a prolonged residence time in Apatite Partial Annealing Zone (APAZ), that is the temperature interval between 120 - 60 °C in which tracks accumulate and progressively shortened (e.g. Ketcham et al., 1999; Wagner and Van den haute, 1992). These shortening progressively increases from southeast to northern portion of Brasilia Belt.

It is observed that the dispersion between the samples may be correlated with differential crustal compartment movements, perhaps associated with tectonic efforts of fault reactivation, compressional or extensional.

The thermal monotonic models indicate a cooling throughout the Phanerozoic until the Late Cretaceous (100-80 Ma) that arrived 60-40°C, and then occurs a reheating to 80°C for a period of 20 to 10 Ma, before the final cooling to surface temperatures (Fig. 3).

The two test thermal models proposed (sample LIS-49) one with cooling < 200 Ma and another for heating starting < 100 Ma (Fig.4), indicate that the opening of the Atlantic Ocean was responsible for the increase in the heat flux until Late Cretaceous (100-80 Ma). For the <200 Ma test model, the cooling starts ~140 Ma with temperature remained ~60-50° C until the Neogene, in the last 20 Ma a new cooling episode started until the recent. In the <100 Ma test heating model the temperature remained slightly higher ~60-80° C, and the final cooling also started in the last 20 Ma.

These models (Fig. 4) suggest a cooling rate of 30-40°C with a gradient of 25°C/Km , which indicates exhumation of 1.2 to 1.8 km, i.e., 60 - 80 m Myr^{-1} . These erosion rates are higher than those of Braucher et al. (2004, 4.5 m Myr^{-1}) and corroborate the fact that the ferruginous lateritic duricrusts are young (<

25 Ma, Castro et al. 2022), they started to be form in the recent time (< 20Ma), when the erosion rate decreased.

7. Conclusions

Thermochronological data from the northern portion of Brasilia Belt, Tocantins Province reveal a monotonic cooling history associated with a important geotectonic event in South American Platform, including Gondwana breakup and the opening of the Atlantic Ocean. Tectonically induced slowly exhumation played an important role in controlling the Brazilian Midwest regolith is characterised by a stepwise landscape of highlands, mountains, plateaus, inselbergs, canyons, and alluvial plans.

The data from this work, associated with data from Fonseca et al., (2020, 2021) suggest that there is a rejuvenation of ages towards the continental margin and that from the Brasília Belt passing through the São Francisco craton and also in the Araguaia Belt, the TFA ages present differentiated behaviors. The two main phases of denudation observed by Fonseca et. al (2020, 2021) in the Brasilia Belt, the Paleozoic and Late Cretaceous-Paleocene related exhumation of the Brasilia Belt, were also evidenced in this work, but with a younger interval.

The distribution of fission track ages on the studied area represents a prolonged residence time in Apatite Partial Annealing Zone, in responses to the increase in the heat flux until Late Cretaceous and the thermal histories imply monotonic cooling throughout the Phanerozoic. The thermal histories models with younger cooling than ~140 Ma indicate higher erosion rates in the <20 Ma, this evidence probably is the origin of the modern Brazilian Midwest regolith with occurrence of only ferruginous lateritic duricrust.

8. REFERENCES

- Almeida, F.F.M., Hasui, Y., Brito Neves, B.B., Fuck, R.A., 1981. Brazilian structural provinces: an introduction. *Earth Sci. Rev.* 17, 1–29. [https://doi.org/10.1016/0012-8252\(81\)90003-9](https://doi.org/10.1016/0012-8252(81)90003-9).
- Alvarenga, C.J.S., Botelho, N.F., Dardenne, M.A., Lima, O.N.B., Machado, M.A., 2007. *Geologia das folhas Monte Alegre de Goiás (SD.23-V-C-III), Cavalcante (SD.23-V- C-V) e Nova Roma (SD.23-V-C-VI). Escala 1:100.000. CPRM-UnB. Sheet mem- oirs*, p. 67.
- Artemieva, I.M., 2006. Global $1^\circ \times 1^\circ$ thermal model TC1 for the continental lithosphere: implications for lithosphere secular evolution. *Tectonophysics* 416, 245–277. <https://doi.org/10.1016/j.tecto.2005.11.022>.
- Autin, J., Bellahsen, N., Leroy, S., Husson, L., Beslier, M.O., d'Acremont, E., 2013. The role of structural inheritance in oblique rifting: Insights from analogue models and application to the Gulf of Aden. *Tectonophysics* 607, 51–64. <https://doi.org/10.1016/j.tecto.2013.05.041>.
- Brito Neves, B.B., Fuck, R.A., Pimentel, M.M., 2014. The Brasiliano collage in South America: a review. *Braz. J. Geol.* 44, 493–518. <https://doi.org/10.5327/Z2317-4889201400030010>.
- Brito Neves, B.B., Fuck, R.A., Cordani, U.G., Thomaz Filho, A., 1984. Influence of base- ment structures in the evolution of the major sedimentary basins of Brazil. *Journal of Geodynamics* 1 (3–5), 495–510.
- Brown, R.W., Rust, D.J., Summerfield, M.A., Gleadow, A.J.W., DeWit, M.C.J., 1990. Na early cretaceous phase of accelerated erosion on the south-western margin of Africa: evidence from apatite fission track analysis and the offshore sedimentary record. *Nucl. Tracks Radiat. Meas.* 17, 339–350. [https://doi.org/10.1016/1359-0189\(90\)90056-4](https://doi.org/10.1016/1359-0189(90)90056-4).

- Braucher, R., Lima, C.V., Bourlès, D.L., Gaspar, J.C., Assad, M.L.L., 2004. Stone-line formation processes documented by in situ-produced ^{10}Be distribution, Jardim River basin, DF, Brazil. *Earth Planet Sci. Lett.* 222, 645–651. <https://doi.org/10.1016/j.epsl.2004.02.033>.
- Campos, J.E.G., Dardenne, M.A., 1997. Origem e evolução tectônica da Bacia Sanfranciscana. *Rev. Bras. Geociencias* 27, 283–294.
- Castro, D.L., Fuck, R.A., Phillips, J.D., Vidotti, R.M., Bezerra, F.H.R., Dantas, E.L., 2014. Crustal structure beneath the Paleozoic Parnaíba Basin revealed by airborne gravity and magnetic data. *Brazil. Tectonophys.* 614 <https://doi.org/10.1016/j.tecto.2013.12.009>.
- Castro, R.T., Horbe, A.M.C., Cherem, L.F.S., 2022. The Brazilian Midwest lateritic domains: Regolith features and dynamic. *J. South Am. Earth Sci.* 118, 103959. <https://doi.org/10.1016/j.jsames.2022.103959>
- Chew D., Spikings R. 2015. Geochronology and thermochronology using apatite: time and temperature, lower crust to surface. *Elements*, 11(3), 189-194. <https://doi.org/10.2113/gselements.11.3.189>
- Cogné N., Gallagher K., Cobbold P.R., Riccomini C., Gautheron C. 2012. Post-breakup tectonics in southeast Brazil from thermochronological data and combined inverse-forward thermal history modeling. *Journal of Geophysical Research*, 117. <https://doi.org/10.1029/2012JB009340>
- Cordani, U.G., Pimentel, M.M., Ganade de Araújo, C.E.G., Fuck, R.A., 2013. The significance of the Transbrasiliiano-Kandy tectonic corridor for the amalgamation of West Gondwana. *Brazilian Journal of Geology* 43, 583–597
- Cordeiro, P.F., Oliveira, C.G., 2017. The Goiás Massif: implications for a pre- Columbia 2.2 to 2.0 Ga continent-wide amalgamation cycle in central Brazil. *Precambrian Res.* <https://doi.org/10.1016/j.precamres.2017.06.021>.
- Cuadros, F.A., Botelho, N.F., Fuck, R.A., Dantas, E.L., 2017a. The Ticunzal Formation in central Brazil: Record of Rhyacian sedimentation and metamorphism in the western border of the São Francisco Craton. *J. South Am. Earth Sci.* 79, 307–325. <https://doi.org/10.1016/j.jsames.2017.08.014>
- Cuadros, F.A., Botelho, N.F., Fuck, R.A., Dantas, E.L., 2017b. The peraluminous Aurumina Granite Suite in central Brazil: An example of mantle-continental crust interaction in a Paleoproterozoic cordilleran hinterland setting? *Precambrian Res.* 299, 75–100. <https://doi.org/10.1016/j.precamres.2017.07.029>
- Daly, M.C., Andrade, V., Barousse, C.A., Costa, R., McDowell, K., Piggott, N., Poole, A.J., 2014. Brasiliiano crustal structure and the tectonic setting of the Parnaíba basin of NE Brazil: results of a deep seismic reflection profile. *Tectonics* 33, 2102–2120.
- Dardenne, M.A., 2000. The Brasília fold belt. In: Cordani, U.G., Milani, E.J., Thomaz Filho, A., Campo, D.A. (Eds.), *Tectonic Evolution of South America*, pp. 231–264.
- Dias A.N.C., Moura C.A.V., Milhomem Neto J.M., Chemale F., Girelli T.J., Masuyama K.M. 2017. Geochronology and thermochronology of the gneisses of the Brasiliiano/Pan-African Araguaia Belt: records of exhumation of West Gondwana and Pangea break up. *Journal of South American Earth Sciences*, 80, 174–191. <https://doi.org/10.1016/j.jsames.2017.09.027>
- Donelick, R.A., Ketcham, R.A., Carlson, W.D., 1999. Variability of apatite fission-track annealing kinetics: II. Crystallographic orientation effects. *Am. Mineral.* 84, 1224–1234. <https://doi.org/10.2138/am-1999-0902>.
- Donelick R.A., O'Sullivan, P.B., Ketcham RA. 2005. Apatite fission-track analysis. In: Reiners P, Ehlers T (eds) *Low-temperature thermochronology*. Rev Min Geochem 58:49–94
- Doranti C., Hackspacher P.C., Hadler Neto J.C., Ribeiro M.C.S., Lima H.C. 2008. Evolução do relevo da região do Planalto de Poços de Caldas: correlações entre níveis planálticos e termocronologia por traços de fissão em apatitas. *Revista Geografias*, 87–92. <https://doi.org/10.35699/2237-549X.13255>
- Doranti-Tiritan C., Hackspacher P.C., Ribeiro M.C.S., Glasmacher U.A., Souza D.H. 2014. Relief evolution of Poços de Caldas (SP/MG) Region based in thermochronology data

- and 3D thermokinematic modeling. *Revista Brasileira Geomorfologia*, 15, 291–310. <https://doi.org/10.20502/rbg.v15i2.491>
- Fernie, N., Glorie, S., Jessell, M.W., Collins, A.S., 2018. Thermochronological insights into reactivation of a continental shear zone in response to Equatorial Atlantic rifting (northern Ghana). *Sci. Rep.* 8, 1–14. <https://doi.org/10.1038/s41598-018-34769-x>.
- Fleischer R.L., Price P.B., Walker R.M. 1975. Nuclear tracks in solids: Principles and applications. Berkeley CA, University of California Press.
- Fonseca, A.C., Piffer, G.V., Nachtergael, S., Van Ranst, G., De Grave, J., Novo, T.A., 2020. Devonian to Permian post-orogenic denudation of the Brasília Belt of West Gondwana: insights from apatite fission track thermochronology. *J. Geodyn.* 137. <https://doi.org/10.1016/j.jog.2020.101733>
- Fonseca, A.C.L., Novo, T.A., Nachtergael, S., Fonte-Boa, T.M.R., Van Ranst, G., De Grave, J., 2021. Differential Phanerozoic evolution of cratonic and non-cratonic lithosphere from a thermochronological perspective: São Francisco Craton and marginal orogens (Brazil). *Gondwana Res.* 93, 106–126. <https://doi.org/10.1016/j.gr.2021.01.006>
- Fuck, R.A., Dantas, E.L., Pimentel, M.M., Botelho, N.F., Armstrong, R.A., Laux, J.H., Junges, S.L., Soares, J.E.P., Praxedes, I.F. 2014. Paleoproterozoic crust-formation and reworking events in the Tocantins Province, central Brazil: A contribution for Atlantica supercontinent reconstruction. *Precambrian Research* 244, 53–74. <http://dx.doi.org/10.1016/j.precamres.2013.12.003>
- Fuck, R.A., Pimentel, M.M., Alvarenga, C.J.S., Dantas, E.L., 2017. The northern Brasília belt. In: Heilbron, M., Cordani, U.G., Alkmim, F.F., Orgs (Eds.), *Regional Geology Reviews*, pp. 205–220. https://doi.org/10.1007/978-3-319-01715-0_11.
- Galbraith, R.F., 1990. The radial plot: Graphical assessment of spread in ages. *Int. J. Radiat. Appl. Instrumentation. Part D. Nucl. Tracks Radiat. Meas.* 17, 207–214. [https://doi.org/10.1016/1359-0189\(90\)90036-W](https://doi.org/10.1016/1359-0189(90)90036-W)
- Galbraith, R.F. 1988. Graphical display of estimates having differing standard errors. *Technometrics* 30:271–281. <https://doi.org/10.2307/1270081>
- Galbraith, R.F., 1981. On statistical models for fission track counts. *Math. Geol.* 13, 471–478. <https://doi.org/10.1007/BF01034498>.
- Gallagher, K., Brown, R., Johnson, C. 1998. Fission track analysis and its applications to geological problems. *Ann Rev Earth Planet Sci* 26 (1):519–572. <https://doi.org/10.1146/annurev.earth.26.1.519>
- Gallagher, K., 2012. Transdimensional inverse thermal history modelling for quantitative thermochronology. *J. Geophys. Res.* 117, 1–16. <https://doi.org/10.1029/2011JB008825>.
- Gallagher, K., Charvin, K., Nielsen, S., Sambridge, M., Stephenson, J., 2009. Markov chain Monte Carlo (MCMC) sampling methods to determine optimal models, model resolution and model choice for Earth Science problems. *Mar. Pet. Geol.* 26, 525–535. <https://doi.org/10.1016/J.MARPETGEO.2009.01.003>
- Gallagher, K., Hawkesworth, C.J., Mantovani, M.S.M., 1994. The denudation history of the onshore continental margin of SE Brazil inferred from apatite fission track data. *J. Geophys. Res.* 99, 18117–18145. <https://doi.org/10.1029/94JB00661>.
- Gillespie, J., Glorie, S., Xiao, W., Zhang, Z., Collins, A.S., Evans, N., McInnes, B., De Grave, J., 2017. Mesozoic reactivation of the Beishan, southern Central Asian Orogenic Belt: insights from low-temperature thermochronology. *Gondwana Res.* 43, 107–122. <https://doi.org/10.1016/j.gr.2015.10.004>.
- Gleadow, A.J.W., 1981. Fission-track dating methods: What are the real alternatives? *Nucl. Tracks* 5, 3–14. [https://doi.org/10.1016/0191-278X\(81\)90021-4](https://doi.org/10.1016/0191-278X(81)90021-4)
- Gleadow, A.J.W., Brown, R.W. 2000. Fission-track thermochronology and the long-term denudational response to tectonics. In: Summerfield MA (ed) *Geomorphology and global tectonics*, John Wiley & Sons, p 57–75
- Gleadow A.J.W., Duddy I.R., Green P.F., Lovering J.F. 1986. Confined fission track lengths in apatite: a diagnostic tool for thermal history analysis. *Contributions to Mineralogy and Petrology*, 94, 405–415. <https://doi.org/10.1007/BF00376334>

- Green, P.F., Duddy, I.R., Gleadow, A.J.W., Tingate, P.R., Laslett, G.M., 1986. Thermal annealing of fission tracks in apatite. *Chem. Geol. Isot. Geosci. Sect.* 59, 237–253. [https://doi.org/10.1016/0168-9622\(86\)90074-6](https://doi.org/10.1016/0168-9622(86)90074-6).
- Hackspacher P.C., Godoy D.F., Ribeiro L.F.B., Hadler Neto J.C., Franco A.O.B. 2007. Modelagem térmica e geomorfologia da borda sul do Cráton do São Francisco: termocronologia por traços de fissão em apatita. *Revista Brasileira de Geociências*, 37, 76–86. DOI: 10.25249/0375-7536.200737S47686
- Hackspacher P.C., Ribeiro L.F.B., Ribeiro M.C.S., Fetter A.H., Hadler Neto J.C., Tello C.E.S., Dantas E.L. 2004. Consolidation and break-up of the South American Platform in southeastern Brazil: tectonothermal and denudation histories. *Gondwana Research*, 7, 91–101. [https://doi.org/10.1016/S1342-937X\(05\)70308-7](https://doi.org/10.1016/S1342-937X(05)70308-7)
- Hurford, A.J. 2019. An Historical Perspective on Fission-Track Thermochronology. In: Malusà, M., Fitzgerald, P. (eds) *Fission-Track Thermochronology and its Application to Geology*. Springer Textbooks in Earth Sciences, Geography and Environment. Springer, Cham. https://doi.org/10.1007/978-3-319-89421-8_1
- Hurford, A.J., Green, P.F., 1983. The zeta age calibration of fission-track dating. *Isot. Geosci.* 1, 285–317. [https://doi.org/10.1016/S0009-2541\(83\)80026-6](https://doi.org/10.1016/S0009-2541(83)80026-6).
- Iunes, P.J., Hadler N, J.C., Bigazzi, G., Tello S, C.A., Guedes O, S., Paulo, S.R., 2002. Durango apatite fission-track dating using length-based age corrections and neutron fluence measurements by natural thorium thin films and natural U-doped glasses calibrated through natural uranium thin films. *Chem. Geol.* 187, 201–211. [https://doi.org/10.1016/S0009-2541\(02\)00045-1](https://doi.org/10.1016/S0009-2541(02)00045-1)
- Japsen, P., Bonow, J.M., Green, P.F., Cobbold, P.R., Chiossi, D., Lilletveit, R., Magnavita, L.P., Pedreira, A., 2012. Episodic burial and exhumation in NE Brazil after opening of the South Atlantic. *Bull. Geol. Soc. Am.* 124, 800–816. <https://doi.org/10.1130/B30515.1>.
- Jelinek, A.R., Chemale, F., van der Beek, P.A., Guadagnin, F., Cupertino, J.A., Viana, A., 2014. Denudation history and landscape evolution of the northern East-Brazilian continental margin from apatite fission-track thermochronology. *J. South Am. Earth Sci.* 54, 158–181. <https://doi.org/10.1016/j.jsames.2014.06.001>.
- Ketcham R.A. 2005. Forward and inverse modeling of low-temperature thermochronometry data. *Reviews in Mineralogy and Geochemistry*, 58(1), 275–314. <https://doi.org/10.2138/rmg.2005.58.11>
- Ketcham, R.A. 2019. Fission-Track Annealing: From Geologic Observations to Thermal History Modeling. In: Malusà, M., Fitzgerald, P. (eds) *Fission-Track Thermochronology and its Application to Geology*. Springer Textbooks in Earth Sciences, Geography and Environment. Springer, Cham. https://doi.org/10.1007/978-3-319-89421-8_3
- Ketcham, R.A., Carter, A., Donelick, R.A., Barbarand, J., Hurford, A.J., 2007. Improved modeling of fission-track annealing in apatite. *Am. Mineral.* 92, 799–810. <https://doi.org/10.2138/am.2007.2281>.
- Ketcham, R.A., Donelick, R.A., Carlson, W.D., 1999. Variability of apatite fission-track annealing kinetics: III. Extrapolation to geological time scales. *Am. Mineral.* 84, 1235–1255. <https://doi.org/10.2138/am-1999-0902>.
- Kusznir, N.J., Park, R.G., 1984. Intraplate lithosphere deformation and the strength of the lithosphere. *Geophys. J. Int.* 79, 513–538. <https://doi.org/10.1111/j.1365-246X.1984.tb02238.x>.
- Laux, J.H., Pimentel, M.M., Dantas, E.L., Armstrong, R., Junges, S.L., 2005. Two neoproterozoic crustal accretion events in the Brasília belt, central Brazil. *J. South Am. Earth Sci.* 18, 183–198. <https://doi.org/10.1016/j.jsames.2004.09.003>
- Laslett, G.M., Green, P.F., Duddy, I.R., Gleadow, A.J.W., 1987. Thermal annealing of fission tracks in apatite 2. A quantitative analysis. *Chem. Geol. Isot. Geosci. Sect.* 65, 1–13. [https://doi.org/10.1016/0168-9622\(87\)90057-1](https://doi.org/10.1016/0168-9622(87)90057-1)
- Mackintosh, V., Kohn, B., Gleadow, A., Gallagher, K., 2019. Long-term reactivation and morphotectonic history of the Zambezi Belt, northern Zimbabwe, revealed by multi-method thermochronometry. *Tectonophysics* 750, 117–136. <https://doi.org/10.1016/j.tecto.2018.11.009>.

- Fitzgerald PG, Malusà MG. 2018. Chapter 9. Concept of the exhumed partial annealing (retention) zone and age-elevation profiles in thermochronology. In: Malusà MG, Fitzgerald PG (eds) *Fission-track thermochronology and its application to geology*. Springer
- Manatschal, G., Lavier, L., Chenin, P., 2015. The role of inheritance in structuring hyperextended rift systems: some considerations based on observations and numerical modelling. *Gondwana Res.* 27, 140–164. <https://doi.org/10.1016/j.gr.2014.08.006>.
- Martins-Ferreira, M.A.C., Campos, J.E.G., 2017. Compartimentação geomorfológica como suporte para Estudos de evolução geotectônica: Aplicação Na região da Chapada dos Veadeiros. *Go. Rev. Bras. Geomorfol.* 18 <https://doi.org/10.20502/rbg.v18i3.1119>.
- Martins-Ferreira, M.A.C., Chemale, F., Dias, A.N.C., Campos, J.E.G., 2018. Proterozoic intracontinental basin succession in the western margin of the São Francisco Craton: Constraints from detrital zircon geochronology. *J. South Am. Earth Sci.* 81, 165–176. <https://doi.org/10.1016/j.jsames.2017.11.018>
- Martins-Ferreira M.A.C., Dias A.N.C., Chemale F., Campos J.E.G. 2020. Intracontinental uplift of the Brazilian Central Plateau linked to continental breakup, orogenies, and basin filling, supported by apatite and zircon fission-track data. *Arabian Journal of Geosciences*, 13(17), 1-14. <https://doi.org/10.1007/s12517-020-05885-8>
- Milani, E.J., Melo, J.H.G., Souza, P.A., Fernandes, L.A., França, A.B., 2007. Bacia do Paraná. *Boletim de Geociências Da Petrobras*, pp. 265–287.
- Moura, V.H.S., 2019. Mineralogia e geoquímica de bauxitas de Barro Alto (Goiás): considerações genéticas. Dissertação de Mestrado, Instituto de Geociências, Universidade Federal do Pará, p. 83.
- Oliveira S.G., Hackspacher P.C., Hadler Neto J.C., Iunes P.J., DE Paulo, S.R., Ribeiro L.F.B., SÁENZ C.A.T. 2000. Constraints on the evolution and thermal history of the continental platform of southeast Brazil, São Paulo state, using apatite fission track analysis (afta). *Revista Brasileira de Geociências*, 30(1), 107– 109. Available on line at: <http://www.ppegeo.igc.usp.br/index.php/rbg/article/view/10929>
- Petersen, K.D., Schiffer, C., 2016. Wilson cycle passive margins: control of orogenic inheritance on continental breakup. *Gondwana Res.* 39, 131–144. <https://doi.org/10.1016/j.gr.2016.06.012>.
- Pimentel, M.M., 2016. The tectonic evolution of the Neoproterozoic Brasília Belt, central Brazil: a geochronological and isotopic approach. *Brazil. J. Geol.* 46, 67–82. <https://doi.org/10.1590/2317-4889201620150004>.
- Pimentel, M.M., Fuck, R.A. Neoproterozoic crustal accretion in central Brazil. *Geology* 20(4), 375–379, 1992.
- Pimentel, M.M., Fuck, R.A., Botelho, N.F., 1999. Granites and the geodynamic history of the Neoproterozoic Brasília belt, Central Brazil: A review. *Lithos* 46, 463–483. [https://doi.org/10.1016/S0024-4937\(98\)00078-4](https://doi.org/10.1016/S0024-4937(98)00078-4).
- Pimentel, M.M., Fuck, R.A., Jost, H., Ferreira Filho, C.F., Araujo, S.A. 2000b. The basement of the Brasília Fold Belt and the Goiás Magmatic Arc. In: Cordani, U.G., Milani, E.J., Thomaz Filho, A., Campos, D. A. (Org.). *The Tectonic Evolution of South America*. Rio de Janeiro, 31st International Geological Congress, 195–229.
- Pimentel, M.M., Fuck, R.A., Gioia, S.M.C.L., 2000b. The neoproterozoic Goiás Magmatic Arc, Central Brazil: A review and new Sm-Nd isotopic data. *Rev. Bras. Geociências* 30, 035–039. <https://doi.org/10.25249/0375-7536.2000301035039>
- Pimentel M.M., Jost H., Fuck R.A. 2004. O embasamento da Faixa Brasília e o Arco Magmático de Goiás. In: Mantesso-Neto V., Bartorelli A., Carneiro C.D.R., Brito-Neves B.B. (ed.). *Geologia do continente sul-americano: Evolução da obra de Fernando Flávio Marques de Almeida, Beca*. P. 324–355.
- Pimentel, M.M., Rodrigues, J.B., DellaGiustina, M.E.S., Junges, S., Matteini, M., Armstrong, R., 2011. The tectonic evolution of the Neoproterozoic Brasília Belt, central Brazil, based on SHRIMP and LA-ICPMS U-Pb sedimentary provenance data: A review. *J. South Am. Earth Sci.* 31, 345–357. <https://doi.org/10.1016/j.jsames.2011.02.011>.

- Price, G.D., Valdes, P.J., Sellwood, B.W., 1997. Prediction of modern bauxite occurrence: implications for climate reconstruction Gregory. *Palaeogeogr. Palaeoclimatol. Palaeoecol.* 131, 1–13.
- Reuber, K., Mann, P., 2019. Control of Precambrian-to-Paleozoic orogenic trends on alongstrike variations in Early Cretaceous continental rifts of the South Atlantic Ocean. *Interpretation* 7, SH45–SH69. <https://doi.org/10.1190/INT-2018-0257.1>.
- Ribeiro L.F.B., Hackspacher P.C., Ribeiro M.C.S., Hadler Neto J.C., Tello S.C.A., Iunes P.J., Franco A.O.B., Godoy D.F. 2005a. Thermotectonic and fault dynamic analysis of Precambrian basement and tectonic constraints with the Parana basin. *Radiation Measurements*, 39, 669–673. <https://doi.org/10.1016/j.radmeas.2004.09.007>
- Ribeiro L.F.B., Saenz C.A.T., Iunes P.J., Hackspacher P.C., Hadler Neto, J.C., Paulo S.R 2005b. Phanerozoic brittle tectonics in the South American continental platform, southeast Brazil: new insights from fission-track studies on apatite in reactivated fault zones. *Revista Brasileira Geociências*, 35, 151–164. DOI: 10.25249/0375-7536.2005352151164
- Riccomini, C., Velázquez, V.F., Gomes, C.B., 2005. Tectonic controls of the Mesozoic and Cenozoic alkaline magmatism in the central-southeastern Brazilian Platform. In: Comin-Chiaromonti, P., Gomes, C.B. (Eds.), *Mesozoic to Cenozoic Alkaline Magmatism in the Brazilian Platform*. Editora da Universidade de São Paulo, São Paulo, pp. 31–57.
- Salgado, A.A.R., Bueno, G.T., Diniz, A.D., Marent, B.R., 2015. Long-term geomorphological evolution of the Brazilian Territory. In: *World Geomorphological Landscapes*. https://doi.org/10.1007/978-94-017-8023-0_3.
- Schiffer, C., Doré, A.G., Foulger, G.R., Franke, D., Geoffroy, L., Gernigon, L., Holdsworth, B., Kusznir, N., Lundin, E., McCaffrey, K., Peace, A.L., Petersen, K.D., Phillips, T.B., Stephenson, R., Stoker, M.S., Welford, J.K., 2019. Structural inheritance in the North Atlantic. *Earth Sci. Rev.*, 102975 <https://doi.org/10.1016/j.earscirev.2019.102975>.
- Tagami, T. 2005. Zircon fission-track thermochronology and applications to fault studies. *Reviews in Mineralogy and Geochemistry*, 58(1), 95–122. <https://doi.org/10.2138/rmg.2005.58.4>
- Tanizaki, M.L.N., Campos, J.E.G., Dardenne, M.A., 2015. Estratigrafia do Grupo Araí: Registro de rifteamento paleoproterozoico no Brasil Central. *Brazilian J. Geol.* 45, 95–108. <https://doi.org/10.1590/23174889201500010007>
- Tello Saenz CA, Hackspacher PC, Hadler Neto JC, Iunes P.J., Guedes S., Ribeiro L.F.B, Paulo S.R. 2003. Recognition of Cretaceous, Paleocene, and Neogene tectonic reactivation through apatite fissiontrack analysis in Precambrian areas of southeast Brazil: Association with the opening of the South Atlantic Ocean. *Journal of South American Earth Sciences*, 15, 765–774. [https://doi.org/10.1016/S0895-9811\(02\)00131-1](https://doi.org/10.1016/S0895-9811(02)00131-1)
- Tello Saenz C.A., Hadler Neto J.C., Iunes P.J., Guedes S., Hackspacher P.C., Ribeiro L.F.B., Paulo S.R., Osorio A.M.A. 2005. Thermochronology of the South American platform in the state of São Paulo, Brazil, through apatite fission tracks. *Radiation Measurements*, 39, 635–640. <https://doi.org/10.1016/j.radmeas.2004.08.005>
- Tommasi, A., Vauchez, A., 1997. Continental-scale rheological heterogeneities and complex intraplate tectono-metamorphic patterns: insights from a case-study and numerical models. *Tectonophysics* 279, 327–350. [https://doi.org/10.1016/S0040-1951\(97\)00117-0](https://doi.org/10.1016/S0040-1951(97)00117-0).
- Tommasi, A., Vauchez, A., 2001. Continental rifting parallel to ancient collisional belts: an effect of the mechanical anisotropy of the lithospheric mantle. *Earth Planet. Sci. Lett.* 185, 199–210. [https://doi.org/10.1016/S0012-821X\(00\)00350-2](https://doi.org/10.1016/S0012-821X(00)00350-2).
- Uhlein, A., Alvarenga, C.J.S., Dardenne, M.A., Trompette, R.R., 2011. Chapter 51 The glaciogenic Jequitá Formation, southeastern Brazil. *Geol. Soc. Mem.* 36, 541–546. <https://doi.org/10.1144/M36.51>
- Valeriano, C.M., Dardenne, M.A., Fonseca, M.A., Simões, L.S.A., Seer, H.J., 2004. A evolução tectônica da Faixa Brasília. In: Mantesso Neto, V., Bartorelli, A., Carneiro, C.D.R., Brito Neves, B.B. (Org.), *Geologia do Continente Sul-Americano – Evolução da obra de Fernando Flávio Marques de Almeida*. São Paulo, Beca, pp. 575–592.

- Valeriano, C.M., Pimentel, M.M., Heilbron, M., Almeida, J.C.H., Trouw, R.A.J., 2008. Tectonic evolution of the Brasilia Belt, central Brazil, and early assembly of Gondwana. Geological Society, London Special Publication 294, p.197–p.210. <https://doi.org/10.1144/SP294.1>
- Valeton, I., Beissner, H., Carvalho, A., 1991. The Tertiary bauxite belt on tectonic uplift areas in the Serra da Mantiqueira, SouthEast Brazil. In: Fuchtbauer, H., Lisitzin, A., Milliman, J.D., Seibold, E. (Eds.), Contributions to Sedimentology. E. Schweizerbart'sche Verlagsbuchhandlung, Stuttgart, pp. 1–99.
- Van Der Beek, P., Mbede, E., Andriessen, P., Delvaux, D., 1998. Denudation history of the Malawi and Rukwa Rift flanks (East African Rift System) from apatite fission track thermochronology. *J. African Earth Sci.* 26, 363–385. [https://doi.org/10.1016/S0899-5362\(98\)00021-9](https://doi.org/10.1016/S0899-5362(98)00021-9)
- Vermeesch, P., 2018. IsoPlotR: A free and open toolbox for geochronology. *Geosci. Front.* 9, 1479–1493. <https://doi.org/10.1016/j.gsf.2018.04.001>.
- Wagner, G., Van den haute, P., 1992. Fission Tracks dating. Kluwer Academic Publishers, Dordrecht. <https://doi.org/10.1016/B0-44-452747-8/00052-1>.
- Will, T.M., Frimmel, H.E., 2018. Where does a continent prefer to breakup? Some lessons from the South Atlantic margins. *Gondwana Res.* 53, 9–19. <https://doi.org/10.1016/j.gr.2017.04.014>.

FIGURE CAPTIONS

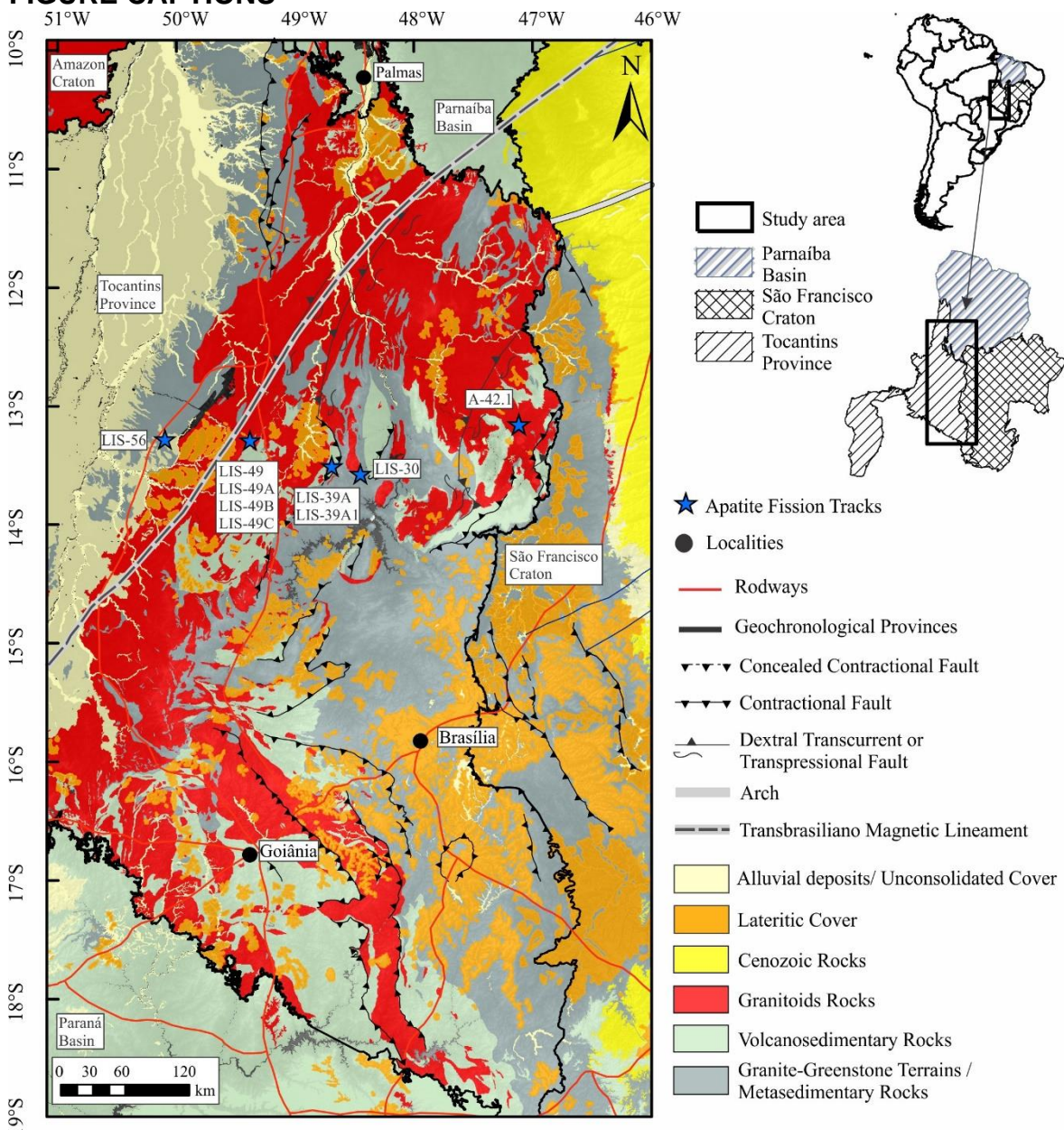


Fig. 1: Simplified geological map of the studied area and sampling locations.

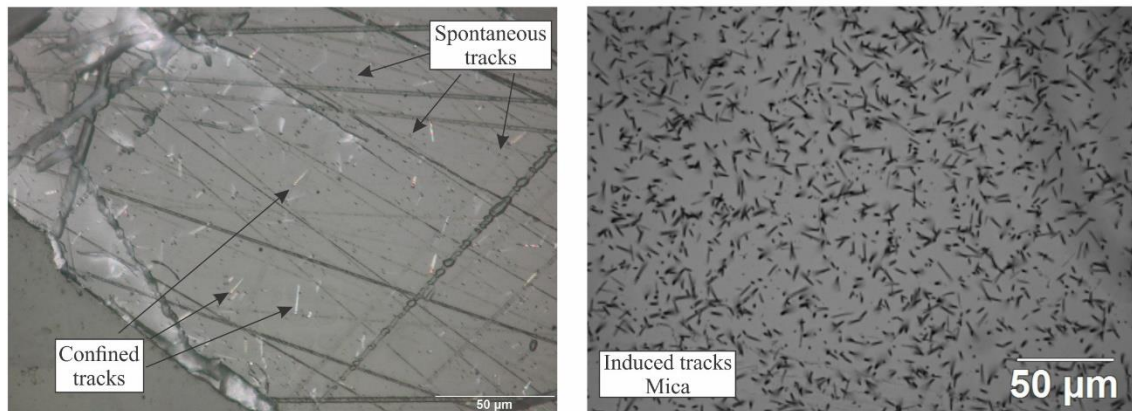
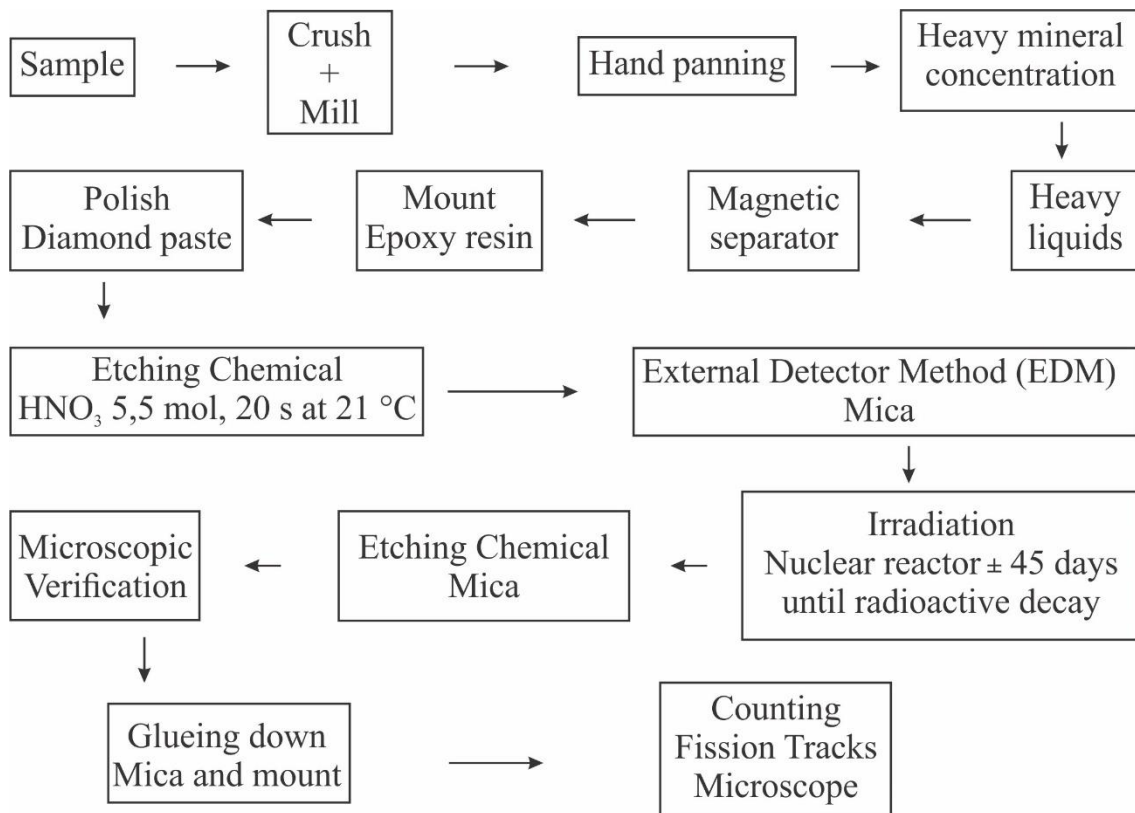


Fig. 2: Sample preparation of apatite fission track and counting on microscope.

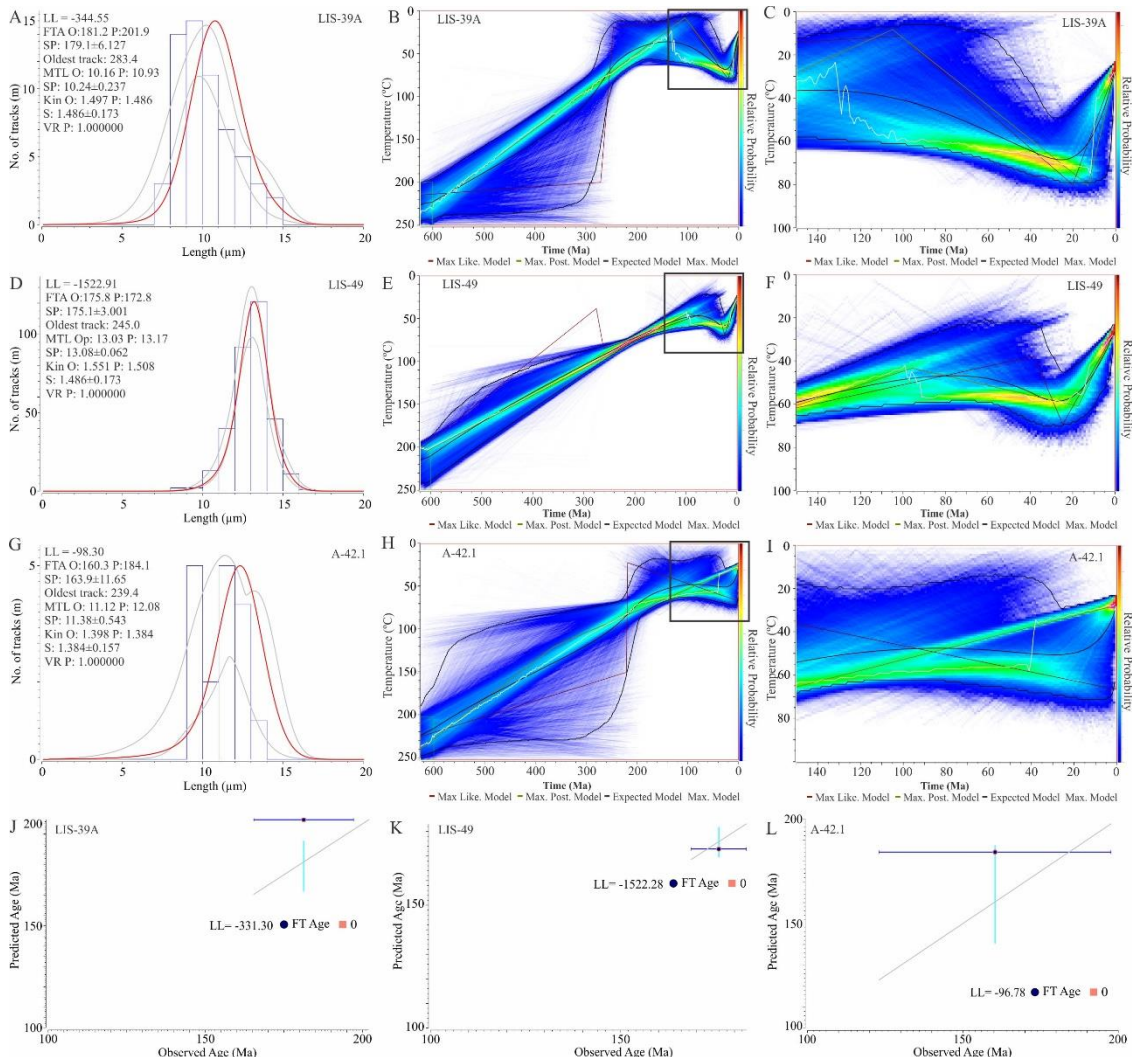


Fig. 3: AFT data from samples LIS-39A first line, LIS-49 second and, A-42.1 third line. Track length histograms showing number of measured tracks (m), the MTL and standard deviation are presented in the Figures 3A, 3D and 3G. Thermal history models reconstructed using the QTQt software (Gallagher, 2012) and the (Ketcham et al., 2007) algorithm are presented in the Figures 3B, 3E, 3H, details of the thermal history over the last 100 My are shown in the figures on the right of the respective samples in the Figures 3C, 3F, and 3I. The fourth line, Figures 3J to 3L correspond to predictive versus observed ages.

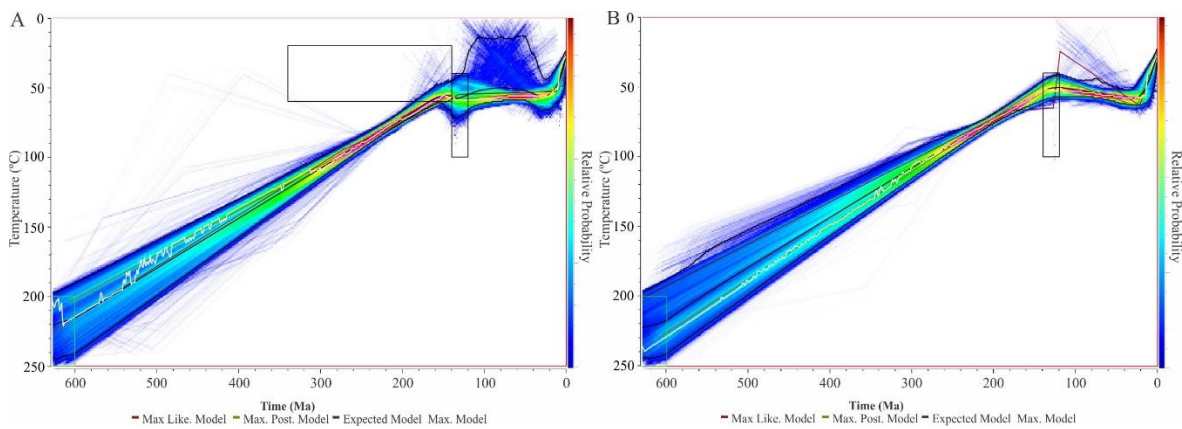


Figure 4: Test thermal history models reconstructed using the QTQt software (Gallagher, 2012) and the (Ketcham et al., 2007) from sample LIS-49. A) Test thermal history model for cooling < 200 Ma. B) Test thermal history model heating <100 Ma in the last 140 Ma.

Table 5.1: Basement apatite fission track analysis results of northern of Brasilia Belt – Tocantins Province; $\zeta = 102.25$.

Sample	Rock	Unit	Crustal Block	Latitude (S)	Longitude (W)	Elevation	N grains	Central Age	Pooled Age	P (χ^2)	M
LIS-39A	Gneiss	Aurumina Suíte	Goiás Magmatic Arc	13°30'22.68"	48°41'26.52"	343	22	179.1 ± 6.127	178.51 ± 6.42	0.00028	100
LIS-49	Gneiss	Aurumina Suíte	Crystalline basement	13°17'7.44"	49°22'41.88"	401	76	162.2 ± 11.1	175.1 ± 3.001	0.08200	110
A-42.1	Granite	Oeste de Goiás Granite	Goiás Magmatic Arc	12°35'32.08"	47° 8'16.90"	384	6	163.9 ± 11.65	154.58 ± 11.18	0.37000	110
LIS-30	Metasedimentary	Paranoá Group	Brasília Belt	13°34'12.72"	48°26'43.80"	469	5	139.3 ± 22.5	100.7 ± 10.4	0.23000	9.08
LIS-56	Tonalite	Xambioá Formation	Araguaia Belt	13°16'35.04"	50° 5'40.56"	305	3	70.6 ± 11.9	74.29 ± 11.5	0.74000	8.71

The samples LIS-30 and LIS-56 less than 5 analysable apatite grains and are not used in the Track length histograms and Thermal history models.

Table 5.2: FT data for the Tocantins Province

	(Dias et al. 2017)		Martins-Pereira et al. 2020	
ZFT	498 ± 8 to 489 ± 15 Ma	Orogenic collapse	549 ± 26 Ma to 519 ± 41 Ma	Brasilia Belt exhumation
	345 ± 13 to 331 ± 8 Ma	Gondwanides orogeny	398 ± 22 Ma to 328 ± 25 Ma	Famatinian orogeny
	208 ± 10 to 197 ± 3 Ma	Mosquito Magmatism	289 ± 15 Ma	Gondwanides orogeny
		Araguaia Belt	Brasilia Belt	
AFT	Fonseca et al. 2020		Fonseca et al. 2021	
	386±31 to 243±13 Ma	Brasilia Belt exhumation	331 ± 23 to 206 ± 15 Ma	Brasilia Belt exhumation
	Martins-Pereira et al. 2020		This work	
	77 ± 11 to 63 ± 2 Ma	Breaking of Pangea and/or Andean Orogeny	178.51 ± 6.4 to 154.58 ± 11.2 Ma	Brasilia Belt exhumation
Brasilia Belt				

CAPÍTULO 6

**ARTIGO 3: MINERALOGY AND
GEOCHEMISTRY OF REGOLITH IN THE
BRAZILIAN MIDWEST LATERITIC
DOMAINS – esboço**

6 MINERALOGY AND GEOCHEMISTRY OF REGOLITH IN THE BRAZILIAN MIDWEST LATERITIC DOMAINS – ESBOÇO

1. INTRODUCTION

Tropical shields are mantled by lateritic regolith generally derived from intense rock weathering under warm/humid and seasonally contrasted climates (Tardy, 1997). Weathering is a fundamental process in the tropical lateritic regolith evolution and is commonly associated with the formation of lateritic profiles with supergenic enrichment in iron, aluminium, titanium, and other residual elements and depleted in silica and base elements (Nahon and Tardy, 1992; Tardy, 1997). Lateritic weathering profiles (up to c. 100 m thickness) are currently exposed on relict palaeolandsurfaces over large cratonic areas of Africa, South America, Australia and India.

Ferruginous and bauxitic laterites are common features in the tropical to subtropical landscape, typically located on flat planation surfaces (King, 1962; Théveniaut and Freyssinet, 2002), they are products of intense subaerial rock weathering and can lead to Al and/or Fe accumulation, that consist predominantly of secondary minerals in a rather simple mineral assemblages of kaolinite, goethite, hematite, aluminium hydroxides and quartz. Bauxitic laterites differ from ferruginous laterites, in that bauxitization results in an almost complete elimination of silica and a stronger enrichment of aluminium hydroxides, such as gibbsite, boehmite and diaspore (Bardossy and Aleva, 1990).

The classical laterites are deep stratified weathering profiles, frequently capped by a ferruginous duricrusts but without important Al enrichment, while lateritic bauxites are weathering products in which Al and Fe accumulated (Valeton, 1972; Bardossy and Aleva, 1990; Carvalho et al., 1997), both are formed under tropical and subtropical climatic conditions (Bardossy and Aleva, 1990; Schellmann, 1994; Tardy and Roquin, 1998; Valeton, 1999). Among specific environmental conditions necessary, preferentially under more seasonally contrasted monsoonal tropical to subtropical climate to form ferruginous laterites, whereas bauxitic laterites require generally a more precipitations and short dry periods (Price et al., 1997; Tardy, 1997; Tardy and Roquin, 1998), in addition specific drainage conditions with high permeability of parent rock and strong dissection of the surface are also necessary to bauxites genesis (Bardossy and Aleva, 1990).

Over the geological times, the lateritic regolith are thus records of past climate and landscape, containing information on the evolution of the continental surfaces, especially in areas of tectonic quiescence prone to weathering, this particularity contribute to preservation of laterites from dismantling for long periods of exposition, making them potential good records of local past environmental conditions prevailing during the lateritic regolith evolution (e.g., Vasconcelos et al., 1994, 2015, 2019; Tardy and Roquin, 1998; Balan et al., 2005; Monteiro et al., 2014, 2018; Riffel et al., 2015; Allard et al., 2018;).

The Midwest lateritic regolith is composed for Archean to Paleozoic rocks outcrop, and unlike the well-developed and preserved lateritic bauxites of the Amazon, only large ferruginous lateritic duricrusts occur (Martins et al., 2004; Latrubesse, 2006; Moraes, 2014; Ribeiro, 2017; Souza et al., 2021; Peixoto et al., 2021). However, despite being located in a cratonic domain, the tectonic quiescence and favourable climatic conditions for the formation of lateritic bauxites (Price et al., 1997), only hydrothermal bauxites have been identified in this region (Valeton et al., 1991; Moura, 2019).

2.GEOLOGICAL SETTING OF TOCANTINS PROVINCE

The Tocantins Province (Almeida et al., 1981) is an extensive Brasiliano/Pan-African orogen of the South American Platform formed by the collision between the Amazonian, São Francisco/Congo, West African/São Luís and Paranapanema cratons that resulted in the amalgamation of the Western Gondwana supercontinent in the Neoproterozoic (Brasiliano orogeny). The province is composed of three Neoproterozoic fold belts: the Paraguay, Araguaia and Brasília belts (Pimentel et al., 2000), in this work, only rocks from the Araguaia and Brasília belts are found. The area is crossed by the Transbrasiliano Lineament (TBL), a major lithospheric discontinuity in the region, which defines the boundary of different crustal domains (Cordani and Sato, 1999; Cordani et al., 2013; Brito Neves and Fuck, 2014).

The Araguaia Belt comprises the central and northern parts of the Tocantins Province (Fig. 1). Along its eastern boundary, the belt is covered by sedimentary rocks of the Paleozoic-Mesozoic Parnaíba basin. This basin covers a rigid lithosphere block, which probably represents its cratonic core (Brito Neves et al., 1984; Góes et al., 1993; Nunes, 1993; Brito Neves, 1998; Castro et al., 2014; Daly et al., 2014). In the western portion by granitoids of the Amazonian Craton. To the southeast, the belt is delimited by the Goiás Massif.

The Brasília Belt borders the western margin of the São Francisco Craton and is one of the most important and preserved Brasiliano orogens of the South American Platform. This belt has an elongated shape in the north-south direction, extending over 1000 km in the central-northern portion of the Brazil (Dardenne, 2000; Fuck et al., 2014; Pimentel, 2016). The Brasília Belt is formed by External Domain, Passive Margin, Internal Domain and Goiás Magmatic Arc, (Pimentel and Fuck, 1992, 1994; Pimentel et al., 2000a, 2000b; Valeriano et al., 2008; Fuck et al., 2014, 2017; Pimentel, 2016; Cordeiro and Oliveira, 2017; Cuadros et al., 2017a).

The External Domain comprises the basement formed by metasedimentary rocks from Ticunzal Formation, the granites from Aurumina and Pedra Branca suites (Alvarenga et al., 2007; Tanizaki et al., 2015; Cuadros et al., 2017b), and Araí, Paranoá and Bambuí groups (Fuck et al., 2014; Pimentel, 2016). These rocks overlie the basement units, covering an area of approximately 10,000 km² in the northeast of Goiás and southeast of Tocantins states (Dardenne, 2000; Alvarenga et al., 2007; Pimentel, 2016; Tanizaki et al., 2015; Cordeiro and Oliveira, 2017; Martins-Ferreira et al., 2018).

The Passive Margin is formed by metasedimentary rocks from Vazante, Paranoá, Canastra, Andrelândia, and Ibiá Groups (Fuck et al., 2014; Pimentel, 2016; Pimentel et al., 2004; Valeriano et al., 2004, 2008) (Fig. X). The Internal Domain comprises the Metamorphic Core and the Goiás Massif (Fuck et al., 2014; Pimentel, 2016). The metamorphic core comprises the Neoproterozoic metasedimentary rocks of the Araxá Group and the high-grade rocks of Anápolis–Itauçu Complex and the Goiás massif includes Archean granite-greenstone terrains and Paleoproterozoic orthogneiss, covered by the Paleoproterozoic Serra da Mesa Group (Fuck et al., 2017). The Goiás Magmatic Arc comprises Neoproterozoic orthogneiss terrains and volcanic-sedimentary sequences (Fuck et al., 2017) is divided into Mara Rosa (northern) and Arenópolis (south-southeastern) Magmatic Arcs (Cordeiro and Oliveira, 2017; Fuck et al., 2008, 2014; Laux et al., 2005; Pimentel and Fuck, 1994; Pimentel et al., 2000a, 2000b; 2004; Pimentel, 2016; Valeriano et al., 2008).

Phanerozoic sedimentary rocks of the Parnaíba and Paraná basins cover the province on the north and south, respectively, these basins also cover older stable continental blocks, such as the so-called Parnaíba and Paranapanema blocks (Fuck et al., 2014, 2017). Post-Paleozoic alkaline magmatism intruded the provinces basement mainly in areas surrounding the Paraná basin and the Brasília Belt, three very similar intracratonic basins were developed in Cretaceous times: the Sanfranciscana, Parecis, and Bauru basins. The Brasília belt hosted several alkaline magmatic pulses between the late Cretaceous and Paleogene (Riccomini et al. 2005). The Sanfranciscana basin developed over the São Francisco Craton and shows the following Mesozoic stratigraphy: a Lower Cretaceous fluvial-lacustrine sequence (Areado Group) and Upper Cretaceous sequences deposited in the eolian system (Urucuia Group), alluvial fans (Capacete Formation, Mata da Corda Group), and alkaline volcanic (Patos Formation, Mata da Corda group) (Campos and Dardenne 1997a, b). Cretaceous and Cenozoic continental covers, standing out the Pantanal, the Araguaia plain (Almeida et al. 1981) and Sanfranciscan basin are pulses of younger sedimentation (Campos and Dardenne, 1997 a, b; Uhlein et al., 2011).

3. MATERIAL AND METHODS

3.1. GEOCHEMICAL SAMPLE PREPARATION

The mineral composition of the pulverized samples was determined by X-ray diffraction (Rigaku ULTIMA IV with Cu tube). In all pulverized samples, the total main oxides (SiO_2 , Al_2O_3 , Fe_2O_3 , TiO_2 , and P_2O_5) were analysed by ICP-OES and the trace elements (Ba, Be, Co, Cs, Ga, Hf, Nb, Rb, Sc, Sr, Ta, Th, U, V, W, Zr, Y, and REE) by ICP-MS. Both groups of elements were analysed after fusing an aliquot with either Li metaborate or tetraborate, followed by dissolution in dilute nitric solution (total extraction).

Table 6.1 Chemical composition values express as wt %

Sample	Type	Surface	SiO ₂	Al ₂ O ₃	Fe ₂ O ₃	CaO	MgO	Na ₂ O	K ₂ O	TiO ₂	P ₂ O ₅	LOI	Total
1	Duricrust	2	28	18.5	44.1	0.01	0.59	0.03	1.86	0.74	0.02	7.95	101.84
2	Duricrust	2	20.5	12.75	55.8	0.01	0.06	0.01	0.16	0.73	0.05	10.7	100.78
3	Duricrust	2	22.2	17.15	45.7	0.01	0.08	0.03	0.32	1.93	0.11	12.1	99.68
4	Duricrust	2	20.3	17.75	43.4	0.01	0.01	0.01	0.08	1.2	0.15	14.7	97.7
5	Duricrust	2	38.1	3.53	46.6	0.01	0.01	0.01	0.01	0.14	0.03	6.49	94.92
6	Duricrust	2	34.7	7.18	43.4	0.01	0.01	0.01	0.02	0.40	0.03	10.1	95.95
7	Duricrust	2	24.8	11.2	49.7	0.01	0.01	0.01	0.03	0.73	0.06	12.4	98.96
8	Duricrust	2	19.0	13.4	54.5	0.01	0.03	0.02	0.13	0.64	0.08	12.6	100.37
9	Duricrust	2	25.4	18.8	42.5	0.01	0.04	0.02	0.26	0.96	0.08	13.25	101.37
10	Duricrust	2	18.5	15.6	50.4	0.01	0.03	0.01	0.2	0.84	0.11	13.00	98.65
11	Duricrust	2	20.7	15.5	51.8	0.01	0.07	0.02	0.37	0.83	0.11	9.82	99.29
12	Duricrust	2	26.9	23.1	33.6	0.01	0.06	0.01	0.35	1.53	0.06	13.60	99.26
13	Duricrust	2	17.9	15.5	52.4	0.01	0.03	0.01	0.18	0.75	0.10	12.00	98.84
14	Duricrust	2	26.0	20.0	40.4	0.01	0.01	0.01	0.09	1.10	0.06	11.10	98.83
15	Duricrust	2	25.8	17.0	42.0	0.04	0.06	0.03	0.32	1.02	0.06	12.65	99.02
16	Duricrust	2	22.4	20.1	41.4	0.01	0.06	0.01	0.28	0.85	0.11	13.50	98.75
17	Duricrust	2	23.0	20.5	40.4	0.01	0.1	0.03	0.4	0.98	0.07	13.40	99.12
18	Duricrust	2	16.3	13.9	54.5	0.01	0.07	0.02	0.51	0.54	0.11	12.30	98.29
19	Duricrust	2	27.2	18.7	42.3	0.01	0.02	0.01	0.13	1.11	0.05	10.80	100.38
20	Duricrust	2	26.4	21.8	38.6	0.01	0.03	0.01	0.14	1.32	0.10	11.05	99.54
21	Duricrust	2	20.9	17.7	47.6	0.01	0.09	0.05	0.61	0.74	0.08	12.50	100.28
22	Duricrust	2	19.9	16.1	49.9	0.01	0.12	0.01	0.43	0.96	0.06	11.35	98.83
23	Duricrust	2	23.2	18.6	43.8	0.01	0.02	0.02	0.31	0.97	0.10	12.20	99.22
24	Duricrust	2	28.9	23.4	33.4	0.01	0.06	0.01	0.2	1.07	0.03	12.15	99.25
25	Duricrust	2	26.3	16.4	42.7	0.01	0.08	0.02	0.35	0.36	0.11	13.05	99.41
26	Duricrust	2	30.5	17	40.9	0.01	0.11	0.21	0.52	0.79	0.13	11.55	101.90
27	Duricrust	2	33.0	23.4	28.5	0.02	0.17	0.02	0.57	0.41	0.02	13.50	100.05
28	Duricrust	2	27.2	9.6	47	0.02	0.03	0.01	0.12	0.99	0.59	12.15	99.09
29	Duricrust	3	23	12.1	49	0.01	0.09	0.01	0.26	0.6	0.15	11.1	96.31
30	Duricrust	3	25.4	13.8	47.7	0.01	0.16	0.02	0.55	0.47	0.21	12.45	101
31	Duricrust	3	35.4	14.85	38	0.01	0.13	0.01	0.28	0.84	0.27	11.65	101.51
32	Duricrust	3	51.3	9.29	27.6	0.01	0.11	0.01	0.47	0.28	0.03	7.68	96.81
33	Duricrust	3	29.9	15.4	41.9	0.02	0.29	0.01	0.93	0.9	0.09	11.9	101.6
34	Duricrust	3	38.9	15.5	32.9	0.01	0.23	0.01	0.72	0.72	0.05	11.15	100.22
35	Duricrust	3	48.2	14.05	26.8	0.05	0.24	0.01	0.62	0.79	0.05	8.73	99.59
36	Duricrust	3	31.6	22	32.9	0.01	0.03	0.01	0.04	0.93	0.08	12.6	100.3
37	Duricrust	3	28	20.8	37.7	0.01	0.05	0.02	0.12	1.04	0.16	12.55	100.54
38	Duricrust	3	31.6	17.25	38.4	0.04	0.08	0.02	0.06	1	0.17	12.55	101.34
39	Duricrust	3	27.2	12.9	50.1	0.01	0.1	0.02	0.41	0.49	0.2	10.2	101.94
40	Duricrust	3	50	15.15	27.3	0.02	0.07	0.02	0.41	0.37	0.05	8.36	101.8
41	Duricrust	3	29.6	14.7	40.8	0.01	0.14	0.01	0.4	0.73	0.13	12.55	99.13
42	Duricrust	3	40.8	10.15	35.4	0.01	0.14	0.01	0.44	0.58	0.12	9.46	97.15
43	Duricrust	3	37.1	14.6	37.1	0.06	0.02	0.01	0.11	0.46	0.07	10.5	100.07
44	Duricrust	3	40.9	16.45	27.8	0.08	0.02	0.01	0.36	1.65	0.06	10.6	98.15
45	Duricrust	3	41.1	13.3	34.3	0.17	0.04	0.03	0.43	0.68	0.02	9.95	100.23
46	Duricrust	3	35.5	12.25	41.3	0.05	0.03	0.01	0.04	0.43	0.14	8.15	98.01

47	Duricrust	3	39.4	14.25	34.5	0.07	0.03	0.01	0.1	0.43	0.08	10.05	98.95
48	Duricrust	3	21.3	14.35	49.2	0.12	0.03	0.01	0.19	0.81	0.11	11.85	98.20
49	Duricrust	3	39.0	9.7	39.1	0.11	0.04	0.01	0.2	0.90	0.34	9.41	98.88
50	Duricrust	3	34.0	18.5	32.5	0.08	0.04	0.01	0.09	1.27	0.08	12.60	99.20
51	Duricrust	3	27.3	13.9	43.2	0.09	0.10	0.01	0.02	0.83	0.03	11.90	98.33
52	Duricrust	3	40.4	13.2	34.4	0.18	0.03	0.01	0.35	0.42	0.04	10.10	99.17
53	Duricrust	3	44.0	9.6	34.5	0.02	0.02	0.01	0.02	0.36	0.20	10.00	98.73
54	Duricrust	3	39.0	12.3	36.3	0.11	0.01	0.01	0.3	0.74	0.10	10.30	99.15
55	Duricrust	3	45.6	11.9	33.6	0.05	0.02	0.01	0.12	0.36	0.07	8.79	100.56
56	Duricrust	3	32.6	15.8	38.3	0.01	0.13	0.01	0.39	0.36	0.06	11.00	98.70
57	Rock	3	64.4	16.8	4.57	2.73	2.16	3.68	3.29	0.54	0.15	1.29	99.61
58	Rock	3	37.1	9.59	46.6	0.01	0.11	0.02	0.48	0.82	0.14	6.04	100.91
59	Rock	3	49.3	15.2	12.35	7.15	10.00	2.77	0.23	0.87	0.07	1.88	99.77
60	Rock	3	51.5	12.65	17.6	3.59	7.20	2.81	1.46	3.46	0.75	0.21	101.23
61	Rock	3	54.3	14.15	10.3	5.50	6.00	4.11	1.48	0.83	0.14	2.17	98.98
62	Rock	3	55.1	13.7	9.61	4.79	8.86	4.25	0.45	0.79	0.11	1.75	99.41
63	Rock	3	43.4	11.0	12.6	5.11	9.87	1.63	0.52	0.87	0.10	13.20	98.30
64	Rock	3	65.3	16.8	7.6	0.04	1.23	0.05	5.2	0.75	0.07	4.46	101.50
65	Rock	3	65.8	17.0	8.0	0.01	0.46	0.15	4.28	0.62	0.04	3.76	100.11
66	Rock	2	45.1	3.3	13.6	4.23	32.37	0.14	0.02	0.39	0.06	7.28	106.55
67	Rock	2	52.4	13.2	12.0	10.58	8.30	2.34	0.17	0.93	0.07	1.69	101.64
68	Rock	2	61.5	16.6	6.8	2.95	2.15	8.78	0.48	0.73	0.14	3.72	103.93
69	Rock	2	57.6	15.3	11.7	4.73	3.46	3.68	1.64	1.16	0.24	1.08	100.60

Table 6.2 - Chemical composition values express as ppm

Sample	Type	Surface	Ba	Co	Cr	Cs	Ga	Hf	Nb	Ni	Pb	Rb	Sc	Sr	Th	U	V	Y	Zn	Zr
1	Duricrust	2	139	1	140	3.07	25.4	7.3	17.1	1	32	60	13	3.9	27	1.69	123	8.6	2	247
2	Duricrust	2	33.6	1	190	1.83	24.8	7.3	14.4	1	55	9.1	11	9.3	15.1	5.15	401	16.6	35	263
3	Duricrust	2	134	10	120	1.02	34.2	7.5	54.1	16	23	12.5	12	64.7	15.6	3.95	376	9.6	73	302
4	Duricrust	2	50	3	260	0.61	34.8	8.4	23.1	30	42	4.3	43	33	21.5	8.11	1090	10.8	95	366
5	Duricrust	2	11	31	70	0.03	11.3	2.3	4.4	1	21	0.5	14	1.9	15.8	0.83	531	1.9	2	93
6	Duricrust	2	63	21	140	0.1	20.7	6	10.6	8	31	1.2	22	4.3	13.75	3.07	565	6	32	232
7	Duricrust	2	27.3	11	120	0.36	18.7	6	19.6	8	55	2.3	35	23.9	29.3	5.52	974	7.1	48	231
8	Duricrust	2	33.6	1	120	1.4	23.3	4.8	12.7	11	45	9.1	18	20.6	18.55	5.3	592	8.4	44	180
9	Duricrust	2	63.6	6	240	2.78	37.9	6.6	20.1	22	36	19.6	34	35.7	32.7	6.41	634	21.1	84	251
10	Duricrust	2	47	1	170	1.32	26	6.2	15.2	13	49	13.2	15	29.5	24.4	5.14	559	18.2	51	230
11	Duricrust	2	68	8	260	1.59	32	5.7	14.5	16	124	17.6	21	13.7	21.3	3.74	732	17.9	28	217
12	Duricrust	2	84	4	240	1.88	45	12.9	29.1	20	29	18.6	16	46.1	26.6	5.49	518	18.8	55	458
13	Duricrust	2	31	7	520	1.04	42	5.6	13.7	14	68	10	25	20.8	35.3	4.55	1145	13.0	54	226
14	Duricrust	2	30	4	380	0.90	34	8.9	22.3	20	104	5.2	15	25.3	21.6	3.63	847	14.7	40	342
15	Duricrust	2	46	7	140	1.17	25	7.3	18.7	16	37	17.3	17	21.9	19.15	4.65	620	16.3	49	269
16	Duricrust	2	66	9	200	2.43	37	7.0	16.3	30	39	21.2	17	41.4	18.8	11.4	544	15.7	108	250
17	Duricrust	2	55	29	320	2.71	62	7.9	18.8	27	58	24	27	21.3	34.8	5.74	753	26.9	196	292
18	Duricrust	2	62	14	130	2.42	21	4.3	9.7	26	42	34	14	17.8	17.55	3.81	712	9.7	80	163
19	Duricrust	2	44	19	360	1.35	34	9.3	20.5	17	53	8	10	25.5	22.3	3.36	491	16.6	31	358
20	Duricrust	2	117	9	270	1.49	44	10.1	27.2	29	67	8.2	15	34.8	25.1	4.37	715	18.5	62	369
21	Duricrust	2	68	9	330	2.77	54	6.3	14.5	18	30	39	12	15.3	25.6	2.8	869	15.4	62	225
22	Duricrust	2	48	20	230	1.77	35	7.9	18.0	25	41	20.3	19	13.2	25.8	4.27	385	16.8	68	292
23	Duricrust	2	64	8	210	1.82	36	7.1	19.0	21	48	20.6	27	31.9	28.3	4.69	520	19.2	54	243
24	Duricrust	2	24	5	180	1.35	42	9.9	22.2	11	29	7	10	15.3	20.9	2.65	379	18.5	28	364
25	Duricrust	2	91	22	90	1.27	19	2.8	5.3	17	20	15.4	13	6.5	7.34	6.14	170	2.4	4	105
26	Duricrust	2	191	136	460	1.89	29	4.8	8.1	64	52	23.5	16	33.2	7.89	7.19	661	10.8	60	185
27	Duricrust	2	259	83	40	1.53	43	9.1	12.3	3	309	33.4	7	7.50	14.1	15.45	83	52.2	164	340

28	Duricrust	2	1995	192	170	0.44	15	5.4	9.7	67	12	10.3	23	6.50	9.19	4.18	674	43.6	279	215
29	Duricrust	3	47.2	1	120	2.66	17.4	6.5	12.2	1	49	27.3	10	6.5	12.35	8.12	199	17.3	2	239
30	Duricrust	3	295	6	290	2.22	18.1	6.2	8.1	9	43	36.2	10	10.9	16.15	6.59	385	13	12	216
31	Duricrust	3	76.3	21	200	3.31	18	11.5	16.2	21	33	26.7	12	6.4	13.8	8.93	422	22.5	8	427
32	Duricrust	3	93.5	39	190	1.53	12.9	5.3	5.8	3	23	28.5	11	4.4	11.65	9.85	153	6.5	2	196
33	Duricrust	3	163.5	14	290	4.23	21.6	10	16.7	23	40	64.6	14	10.5	15.45	10.55	455	19.3	12	384
34	Duricrust	3	139	33	280	3.77	23.5	9.5	13.1	27	36	55.8	15	7.8	15.15	10.1	385	22.2	12	357
35	Duricrust	3	126	10	320	5.74	27.9	8.4	14.1	15	50	57.6	16	8.6	17.75	4.92	397	20.7	8	321
36	Duricrust	3	8.9	4	760	0.64	43.4	14.1	14.2	22	52	2.6	9	3	18.5	5.28	1030	7.4	17	547
37	Duricrust	3	98.8	9	320	0.44	38.2	15.5	21.5	15	40	4.8	14	44.1	34.5	5.75	554	26.6	23	596
38	Duricrust	3	63.5	112	340	0.5	46.4	7	6.8	63	14	3.5	27	3.9	5.97	2.24	1010	9.7	17	290
39	Duricrust	3	270	24	320	1.2	22	4.8	5.8	19	26	16.7	11	6.6	8.26	3.14	377	5.8	29	194
40	Duricrust	3	62	13	190	1.55	23.9	5.6	7.1	16	23	32.4	10	3.8	20.6	14.5	233	5.1	16	198
41	Duricrust	3	93.4	14	280	4.09	26.7	10.7	15.4	20	33	35.3	19	7.6	16.3	8.17	679	18.6	37	414
42	Duricrust	3	111	13	220	3.25	15.6	8	11.9	14	29	39.7	8	6.8	9.88	5.05	362	13.8	23	309
43	Duricrust	3	34	20	150	0.69	21	6.2	4.3	18	28	7.9	8	3.5	4.29	2.12	630	2.5	7	252
44	Duricrust	3	151	55	190	1.39	21	6.4	10.9	49	34	24.9	16	4.6	14.15	2.19	361	6.8	39	242
45	Duricrust	3	142	107	220	0.59	20	3.3	3.9	43	20	21.7	18	5.8	3.68	2.09	683	5.7	21	127
46	Duricrust	3	11	24	570	0.70	20	4.5	4.4	26	24	4.8	17	2.5	3.6	0.87	741	2.6	11	178
47	Duricrust	3	33	14	160	0.70	21	5.4	4.4	19	27	7.9	12	4.0	4.06	2.02	612	2.6	12	215
48	Duricrust	3	179	49	220	0.75	24	5.2	6.6	33	79	12.7	31	4.8	8.28	4.11	886	15.4	26	212
49	Duricrust	3	79	21	80	1.06	15	6.9	7.7	9	30	20.0	15	16.8	6.08	1.86	364	10.1	22	275
50	Duricrust	3	25	23	150	0.24	31	6.2	6.5	34	16	3.9	22	4.1	5.42	2	613	5.1	19	228
51	Duricrust	3	576	283	970	0.32	23	2.6	3.4	202	21	3.6	23	6.4	1.22	0.92	737	7.6	34	88
52	Duricrust	3	178	27	80	0.61	25	11.7	4.8	19	36	19.6	8	4.4	24.10	1.63	562	25.6	18	461
53	Duricrust	3	8	18	80	0.16	16	6.7	4.7	8	19	1.1	12	2.1	3.16	2.21	805	3.0	8	274
54	Duricrust	3	80	27	170	1.31	24	5.9	6.0	39	31	18.3	21	4.5	6.61	2.2	711	7.9	32	214
55	Duricrust	3	28	26	560	0.70	21	6.7	3.3	52	23	13.2	17	1.7	4.42	1.2	776	4.6	13	272
56	Duricrust	3	98	12	610	2.64	36	9.5	8.9	11	16	35.1	13	2.8	18.85	13.45	288	17.5	9	350
57	Rock	3	773	92	80	7.98	26.2	4.2	6.6	42	3	197.5	8	370	5.29	1.29	58	10.1	97	170
58	Rock	3	190	2.0	80	1.17	16.9	15.2	17.6	9	6	19.2	17	34.1	18.45	2.31	278	24.5	18	607

59	Rock	3	51	67	300	0.20	13	1.3	1.3	146	2	5.6	42	100.5	0.25	0.06	234	20.7	99	47
60	Rock	3	740	72	50	0.78	21	6.6	17.5	32	13	32.7	31	315.0	5.28	1.03	231	44.6	171	262
61	Rock	3	406	73	60	0.35	16	3.4	5.7	70	21	38.4	30	138	3.67	0.69	235	22.0	94	129
62	Rock	3	123	69	60	0.07	16	3.2	5.4	69	33	12.6	31	174.5	3.62	0.47	169	19.7	77	119
63	Rock	3	58	59	80	0.39	12	1.5	2.5	78	7	15.4	36	95.4	0.29	0.1	239	19.3	111	49
64	Rock	3	955	29	80	7.71	23	6.2	15.4	10	16	209	15	18.5	14.35	2.44	69	19	24	232
65	Rock	3	498	8	90	8.45	24	3.8	10.3	26	5	179	15	30.5	10.60	1.35	72	14.9	12	134
66	Rock	2	15	119	1583	0.09	4.7	0.5	1.3	2093	3	0.74	13.7	71.45	0.13	0.07	42	6.11	88	15.3
67	Rock	2	26	49	385	0.04	16	1.6	2.5	130.2	3.3	0.78	38.0	110.7	0.28	0.08	295	17	87	54
68	Rock	2	280	18	103	0.34	20	4.3	8.8	39.7	5.3	9.4	13.7	212.7	6.12	2.03	137	18	50	162
69	Rock	2	638	25	32	4.24	21	3.7	5.7	20.3	5.7	53.3	27.3	282.9	2.79	0.97	273	35	154	131

Table 6.3 - REE values express as ppm

Sample	Type	Surface	La	Ce	Pr	Nd	Sm	Eu	Gd	Tb	Dy	Ho	Er	Tm	Yb	Lu	Σ LREE	Σ HREE	Σ REE
1	Duricrust	2	11.6	13.8	1.63	5.1	1.05	0.19	1.01	0.22	1.42	0.31	1	0.25	1.38	0.25	33.4	5.84	39.2
2	Duricrust	2	15.2	54.7	5.35	21.7	5.11	0.99	3.98	0.7	4.41	0.78	2.35	0.41	2.51	0.39	103.1	15.53	118.6
3	Duricrust	2	41.9	53	6.68	19.6	2.55	0.48	1.58	0.28	1.95	0.41	1.34	0.21	1.53	0.25	124.2	7.55	131.8
4	Duricrust	2	34.4	43.1	5.78	17.5	3.11	0.64	2.15	0.4	2.56	0.51	1.44	0.26	1.85	0.25	104.5	9.42	114.0
5	Duricrust	2	2.8	4.8	0.5	1.9	0.4	0.07	0.35	0.06	0.42	0.08	0.25	0.04	0.26	0.06	10.5	1.52	12.0
6	Duricrust	2	7.5	13	1.66	5.8	1.33	0.24	1.03	0.2	1.26	0.26	0.79	0.15	0.99	0.2	29.5	4.88	34.4
7	Duricrust	2	17.3	26.3	2.85	8.8	1.42	0.37	1.15	0.21	1.14	0.31	0.9	0.17	1.11	0.15	57.0	5.14	62.2
8	Duricrust	2	19.9	25.5	2.45	7.3	1.15	0.26	1.05	0.24	1.37	0.31	0.99	0.16	1.21	0.17	56.6	5.5	62.1
9	Duricrust	2	42.2	45.3	5.77	16.1	2.37	0.5	2.55	0.56	3.61	0.76	2.12	0.41	2.39	0.41	112.2	12.81	125.1
10	Duricrust	2	28	34.2	4.47	14.6	2.40	0.51	2.30	0.47	3.12	0.68	2.2	0.34	2.32	0.36	84.2	11.79	96.0
11	Duricrust	2	25.5	28.8	5.63	21	3.84	0.71	3.51	0.53	3.33	0.67	2.26	0.35	2.28	0.34	85.5	13.27	98.8
12	Duricrust	2	46.1	62.2	6.95	22.3	3.56	0.65	2.87	0.54	3.28	0.75	2.48	0.4	3.16	0.45	141.8	13.93	155.7
13	Duricrust	2	24.6	27.8	3.36	10.4	1.52	0.32	1.68	0.32	2.25	0.47	1.64	0.28	1.79	0.29	68.0	8.72	76.7
14	Duricrust	2	20.3	28.9	3.46	12	2.14	0.42	2.05	0.34	2.54	0.56	1.94	0.33	2.22	0.33	67.2	10.31	77.5
15	Duricrust	2	28.3	28.7	3.37	9.6	1.46	0.46	2.20	0.43	2.86	0.67	2	0.36	2.2	0.37	71.9	11.09	83.0
16	Duricrust	2	34.1	40.7	5.27	16.4	3.09	0.58	2.69	0.50	3.00	0.65	2.19	0.38	2.59	0.41	100.1	12.41	112.6
17	Duricrust	2	37.8	62.1	8.04	29.1	5.70	1.07	5.02	0.78	5.49	1.08	3.34	0.52	3.4	0.5	143.8	20.13	163.9
18	Duricrust	2	24.7	23.3	2.59	7.0	1.20	0.27	1.24	0.24	1.72	0.37	1.15	0.19	1.37	0.19	59.1	6.47	65.5
19	Duricrust	2	21.9	33.8	3.64	11.8	2.08	0.41	2.07	0.39	2.77	0.61	2.02	0.38	2.32	0.38	73.6	10.94	84.6
20	Duricrust	2	51	57.5	8.16	23.2	3.44	0.52	2.60	0.47	3.26	0.68	2.37	0.38	2.71	0.39	143.8	12.86	156.7
21	Duricrust	2	9.5	10.8	1.35	4.2	0.87	0.24	1.61	0.33	2.46	0.56	1.73	0.27	1.97	0.28	27.0	9.21	36.2
22	Duricrust	2	15.2	21.3	2.71	8.9	1.95	0.39	2.12	0.40	3.08	0.61	2.03	0.34	2.53	0.35	50.5	11.46	61.9
23	Duricrust	2	30.7	34.1	4.29	11.8	1.97	0.41	2.56	0.51	3.30	0.68	2.44	0.39	2.59	0.36	83.3	12.83	96.1
24	Duricrust	2	17	24.9	2.87	9.1	1.72	0.35	2.12	0.38	2.60	0.59	1.96	0.35	2.33	0.36	55.9	10.69	66.6
25	Duricrust	2	6.4	11.8	1.30	4.3	0.84	0.21	0.67	0.07	0.53	0.08	0.43	0.06	0.49	0.05	24.9	2.38	27.2
26	Duricrust	2	6.9	632	2.39	9.3	2.07	0.60	2.41	0.54	2.81	0.51	1.79	0.3	2.15	0.3	653.3	10.81	664.1
27	Duricrust	2	28.6	2410	6.99	27.2	5.83	1.13	6.89	1.54	7.95	1.75	5.77	0.92	6.08	0.88	2479.8	31.78	2511.5

28	Duricrust	2	33.7	88.4	11.35	45.6	10.55	2.07	9.31	1.63	10.95	2.12	6.56	1.05	7.44	1.01	191.7	40.07	231.7
29	Duricrust	3	18.5	36.7	4.39	15.6	3.27	0.6	2.81	0.55	3.01	0.7	1.84	0.35	2.38	0.33	79.1	11.97	91.0
30	Duricrust	3	12.5	32	2.78	9.5	1.95	0.37	2.12	0.4	2.21	0.51	1.55	0.22	1.55	0.26	59.1	8.82	67.9
31	Duricrust	3	18.5	66.3	3.98	13.7	2.56	0.56	2.95	0.56	3.73	0.8	2.65	0.42	2.71	0.45	105.6	14.27	119.9
32	Duricrust	3	7.8	22.4	2.13	7.2	1.5	0.28	1.34	0.21	1.32	0.3	0.8	0.18	1.18	0.2	41.3	5.53	46.8
33	Duricrust	3	11.9	27.1	2.7	9.7	2.25	0.45	2.57	0.51	3.18	0.73	2.06	0.39	2.4	0.36	54.1	12.2	66.3
34	Duricrust	3	24.2	25.2	5.35	18.7	3.55	0.68	3.56	0.6	3.63	0.85	2.49	0.42	2.48	0.4	77.7	14.43	92.1
35	Duricrust	3	22.5	23	4.87	16.7	3.47	0.56	3.12	0.53	3.3	0.75	2.01	0.38	2.25	0.38	71.1	12.72	83.8
36	Duricrust	3	9.2	31	2.27	7.4	1.49	0.26	1.13	0.19	1.45	0.3	0.92	0.15	1.21	0.19	51.6	5.54	57.2
37	Duricrust	3	47.8	110	10.95	37.2	6.96	1.24	5.17	0.76	5.09	1	3.08	0.52	3.51	0.56	214.2	19.69	233.8
38	Duricrust	3	6.5	81.8	1.9	7.8	1.92	0.52	1.83	0.33	2.07	0.44	1.47	0.25	1.53	0.25	100.4	8.17	108.6
39	Duricrust	3	7.2	49.4	1.7	6.1	1.39	0.35	1.11	0.19	1.29	0.25	0.73	0.14	0.92	0.17	66.1	4.8	70.9
40	Duricrust	3	7.2	12	1.46	5.2	1.16	0.17	0.96	0.16	0.99	0.18	0.53	0.07	0.67	0.11	27.2	3.67	30.9
41	Duricrust	3	18.8	34.5	3.71	12.8	2.42	0.48	2.44	0.5	3.37	0.73	1.98	0.34	2.2	0.36	72.7	11.92	84.6
42	Duricrust	3	14.6	26.4	2.91	9.9	1.75	0.38	1.65	0.33	2.04	0.5	1.4	0.21	1.54	0.26	55.9	7.93	63.9
43	Duricrust	3	1.9	5.3	0.52	2.1	0.53	0.16	0.53	0.08	0.51	0.11	0.35	0.07	0.45	0.08	10.5	2.18	12.7
44	Duricrust	3	21.4	73.6	4.5	17.5	2.99	0.27	2.03	0.27	1.44	0.31	0.86	0.14	0.85	0.17	120.3	6.07	126.3
45	Duricrust	3	6.4	31.8	1.33	5.6	1.15	0.29	1.01	0.17	1.08	0.24	0.67	0.11	0.74	0.13	46.6	4.15	50.7
46	Duricrust	3	2.5	9.4	0.7	2.7	0.47	0.13	0.49	0.09	0.51	0.11	0.33	0.06	0.42	0.09	15.9	2.1	18.0
47	Duricrust	3	2.0	6.0	0.5	2.2	0.53	0.16	0.54	0.08	0.52	0.12	0.35	0.07	0.43	0.08	11.4	2.19	13.6
48	Duricrust	3	13.4	202.0	2.8	11.8	2.08	0.55	2.32	0.45	2.59	0.59	1.71	0.27	1.85	0.3	232.6	10.08	242.7
49	Duricrust	3	24.9	43.9	4.8	18.1	3.22	0.73	2.70	0.40	2.39	0.46	1.35	0.22	1.46	0.26	95.6	9.24	104.9
50	Duricrust	3	2.4	6.4	0.7	3.1	0.77	0.28	1.02	0.18	1.22	0.25	0.86	0.15	1.07	0.19	13.6	4.94	18.6
51	Duricrust	3	4.6	47.0	1.26	5.6	1.35	0.41	1.53	0.28	1.81	0.38	1.12	0.18	1.16	0.19	60.2	6.65	66.9
52	Duricrust	3	11.4	234	2.34	8.2	1.49	0.41	2.10	0.38	2.79	0.68	2.25	0.39	2.51	0.44	257.8	11.54	269.4
53	Duricrust	3	2.1	14.7	0.58	2.4	0.59	0.17	0.53	0.11	0.69	0.13	0.43	0.08	0.56	0.1	20.5	2.63	23.2
54	Duricrust	3	10.6	27.5	2.44	9.6	1.70	0.41	1.75	0.27	1.59	0.31	1.09	0.15	1.25	0.21	52.3	6.62	58.9
55	Duricrust	3	3.2	7.2	0.67	2.7	0.56	0.17	0.61	0.11	0.73	0.14	0.49	0.09	0.67	0.11	14.5	2.95	17.5
56	Duricrust	3	9.2	14.7	2.33	9.2	2.10	0.44	2.17	0.41	2.83	0.69	2.19	0.35	2.43	0.34	38.0	11.41	49.4
57	Rock	3	31.3	57.5	7.02	24	4.15	1.09	2.84	0.36	2.13	0.33	1.12	0.16	0.94	0.12	125.1	8	133.1
58	Rock	3	31.8	58.2	5.66	17.7	3.47	0.66	2.99	0.6	4.52	1.01	3.25	0.52	3.69	0.56	117.5	17.14	134.6

59	Rock	3	3.3	8.1	1.2	6.2	1.92	0.61	3.23	0.55	3.42	0.74	2.27	0.31	2.19	0.35	21.3	13.06	34.4
60	Rock	3	44.3	90.5	10.5	44.9	8.92	2.52	9.94	1.44	8.39	1.71	4.5	0.67	3.95	0.59	201.6	31.19	232.8
61	Rock	3	18.4	39.0	4.5	19.8	3.99	1.11	4.04	0.64	3.95	0.81	2.1	0.33	1.96	0.32	86.8	14.15	101.0
62	Rock	3	17.7	36.8	4.0	18.0	3.59	0.99	3.93	0.54	3.81	0.76	1.92	0.31	1.89	0.3	81.1	13.46	94.6
63	Rock	3	4.7	11.9	1.7	8.5	2.24	0.90	3.47	0.61	3.35	0.73	2.01	0.31	2.2	0.37	29.9	13.05	43.0
64	Rock	3	57.1	88.9	12.7	41.4	6.45	0.99	4.89	0.59	3.75	0.71	2.16	0.35	2.74	0.39	207.5	15.58	223.1
65	Rock	3	37.3	71.4	7.5	23.7	3.38	0.59	2.72	0.44	2.8	0.51	1.54	0.21	1.74	0.24	143.9	10.2	154.1
66	Rock	2	5.0	0.7	3.5	1.01	0.37	1.23	0.20	1.24	0.23	0.69	0.10	0.60	0.09	10.567	4.4	14.961	25.5
67	Rock	2	8.5	1.2	6.4	2.03	0.76	2.98	0.50	3.09	0.65	1.92	0.29	1.76	0.25	18.9	11.4	30.37	49.3
68	Rock	2	55.3	6.6	25.4	4.70	1.25	4.14	0.57	3.23	0.66	1.98	0.31	1.86	0.28	93.3	13.0	106.3	199.7
69	Rock	2	39.9	5.0	21.2	4.93	1.32	5.75	0.94	5.98	1.28	3.74	0.58	3.70	0.56	72.3	22.5	94.85	167.2

CAPÍTULO 7

CONSIDERAÇÕES FINAIS E SUGESTÕES PARA ESTUDOS FUTUROS

7 CONSIDERAÇÕES FINAIS E SUGESTÕES PARA ESTUDOS FUTUROS

7.1 Conclusões

A Província Tocantins, onde está inserida a área de estudo, é um extenso orógeno Brasiliense/Pan-Africano da Plataforma Sul-Americana formado por diversidade de rochas ígneas, metamórficas e sedimentares proterozóicas a cenozóicas agrupadas nas faixas Brasília, Araguaia e Paraguai. A ação da erosão e do intemperismo nessas rochas, gerou um regolito escalonado, complexo, constituído por planaltos, serras, chapadas, inselbergs, cânions e planícies aluviais. Essas feições configuram quatro superfícies morfoestratigráficas (S1, S2, S3 e S4) que indicam rejuvenescimento sequencial por meio de dissecação da paisagem, processo pelo qual os remanescentes da paleopaisagem encontram-se isolados como geoformas reliquias. As características das superfícies e das crostas lateríticas (altitude, textura, mineralogia e química) desenvolvidas nas S2 e S3, e as correlações estratigráficas com outras crostas lateríticas eminentemente ferruginosas (Vasconcelos et al., 1994; Ruffet et al., 1996; Costa et al., 2005; Shuster et al., 2005; Lima, 2008; Monteiro et al., 2014, 2018; Vasconcelos and Carmo, 2018; dos Santos Albuquerque et al., 2020; Heller et al., 2022), as vinculam ao Neógeno (<25 Ma), ou seja, estabilidade apenas no final do Paleógeno. Esse fato, a ausência de bauxitas intempéricas na região, que necessitam período mais longo de estabilidade tectônica (Price et al., 1997), os pulsos magmáticos alcalinos entre o final do Cretáceo e o Paleógeno (Riccomini et al. 2005) e as feições que indicam efeitos neotectônicos na região (Campos et al., 2016), reforçaram reacomodação de blocos litosféricos no centro da plataforma Sul Americana devido a separação África-América do Sul e a consequente subida dos Andes, como já indicado por Martins-Ferreira et al., (2020) e Fonseca et al., (2020 e 2021).

Esses autores mostraram evidências de pelo menos dois e no máximo três episódios distintos de resfriamento devido a soerguimento litosférico, anteriores a 100 Ma na Província Tocantins na porção leste da Faixa Brasília, do Devoniano Médio (386 ± 31 Ma) ao Triássico Médio (243 ± 13 Ma) (Fonseca et al., 2020) na porção central do Cretáceo Superior (77 ± 11 Ma) ao Paleoceno Inferior (63 ± 2 Ma) (Martins-Ferreira et al., 2020) e na porção sudoeste do Carbonífero (331 ± 23 Ma) ao Triássico (206 ± 15 Ma) (Fonseca et al., 2021). Como as crostas lateríticas necessitam clima sazonal e estabilidade tectônica o que confere erosão mínima, e a sua idade inferida de <25 Ma, a reacomodação de blocos deveria ter se estendido por todo o Cenozoico. Essa instabilidade tectônica no Cenozoico sugerida por Martins-Ferreira et al. (2020), é referendada como exumação e aumento do fluxo de calor entre ~60 e ~30 Ma e um resfriamento mais jovem neste estudo. Portanto, as feições do regolito da região estudada são produto de longo processo erosivo e que a estabilidade tectônica da região, necessária para a formação das crostas lateríticas, é muito recente (<20Ma).

7.2 Participação em artigos científicos

[Journal of South American Earth Sciences 106 \(2021\) 103096](#)



Advances in geochemical footprint, iron speciation, and Pb isotopes in the tropical regolith of north-northwestern Amazonia, Brazil

Adriana Maria Coimbra Horbe*, Márcio Fernando dos Santos Albuquerque, Rodrigo Tokuta Castro, Sanclever Freire Peixoto

Universidade de Brasília, Instituto de Geociências, Campus Universitário Darcy Ribeiro, 70910-900, Brasília, Distrito Federal, Brasil



<https://doi.org/10.1016/j.jsames.2020.103096>

[Journal of South American Earth Sciences 111 \(2021\) 103460](#)



Regolith LANDSAT-8/OLI and Hyperion/EO-1 images classification in midwest of Brazil



Marcus Vinicius Souza, Adriana Maria Coimbra Horbe*, Bárbara Costa da Silva, Sanclever Freire Peixoto, Rodrigo Tokuta Castro

Instituto de Geociências, Universidade de Brasília (UnB), Campus Universitário Darcy Ribeiro, 70910-900, Brasília, DF, Brasil

<https://doi.org/10.1016/j.jsames.2021.103460>

Lateritic regolith mapping in tropical environments using multispectral and multisensor Landsat-8 OLI and Sentinel-2 MSI data.

Bárbara Costa da Silva¹, Adriana Maria Coimbra Horbe¹, Sanclever Freire Peixoto², Rodrigo Tokuta Castro¹

Submetido ao International Journal of Remote Sensing

7.3 Sugestões para estudos futuros

- Estender o mapeamento de crostas lateríticas, para aumentar o detalhe e controle de amostragem. Obter maior quantidade de amostras de crostas lateríticas, sempre buscando identificar e diversificar as rochas mãe dos perfis lateríticos.
- Aplicar a datação de crostas lateríticas ferruginosas por U-Th/He para obtenção de idades e corroborar as evidências de duas superfícies com crostas lateríticas em níveis distintos no regolito do Centro-Oeste e estabelecer relações com os eventos de lateritização que ocorreram na região, para compará-los com os dados da literatura.
- Datar mais amostras por traços de fissão em apatita, aumentar a quantidade de dados, para melhorar parâmetros estatísticos, como a maior quantidade de cristais datados, desta forma obter maior quantidade de traços confinados, para gerar mais modelos de termocronologia de baixa temperatura e compará-los com outras regiões da Plataforma Sulamericana, que possuem maior quantidade de dados e modelos, que auxiliam no entendimento dos eventos de evolução tectônica.

ANEXOS

8 ANEXOS - DADOS DA CONTAGEM DE TRAÇOS DE FISSÃO EM APATITA

Tabela: Dados obtidos para cálculo da idade de traços de fissão da amostra LIS-49

Grain	NS	NA	Area (cm²)	RhoS (cm- 2)	Dpar	NI	Rhol (cm-2)	FT age	1s	U ppm	Ns/Ni	Squares	Psj
Grain01	138	100	6.40E-05	2.16E+06	1.749	92	1.438E+06	204.87	27.63	19.92	1.50	65	129
Grain02	99	100	6.40E-05	1.55E+06	1.754	91	1.422E+06	149.23	21.71	19.70	1.09	65	107
Grain03	76	100	6.40E-05	1.19E+06	1.487	71	1.109E+06	146.86	24.27	15.37	1.07	65	83
Grain04	138	100	6.40E-05	2.16E+06	1.634	116	1.813E+06	163.01	20.58	25.11	1.19	65	143
Grain06	64	100	6.40E-05	1.00E+06	1.491	57	8.906E+05	153.96	28.07	12.34	1.12	65	68
Grain07	71	100	6.40E-05	1.11E+06	1.663	43	6.719E+05	225.16	43.55	9.31	1.65	65	64
Grain08	68	100	6.40E-05	1.06E+06	1.692	44	6.875E+05	210.98	40.86	9.53	1.55	65	63
Grain09	148	100	6.40E-05	2.31E+06	1.624	116	1.813E+06	174.67	21.71	25.11	1.28	65	148
Grain10	106	100	6.40E-05	1.66E+06	1.777	64	1.000E+06	225.84	35.80	13.86	1.66	65	96
Grain12	104	100	6.40E-05	1.63E+06	1.375	102	1.594E+06	139.96	19.54	22.08	1.02	65	116
Grain13	112	100	6.40E-05	1.75E+06	1.432	68	1.063E+06	224.61	34.58	14.72	1.65	65	101
Grain14	76	100	6.40E-05	1.19E+06	1.543	57	8.906E+05	182.43	32.00	12.34	1.33	65	75
Grain16	114	100	6.40E-05	1.78E+06	1.561	76	1.188E+06	204.87	30.39	16.45	1.50	65	107
Grain17	121	100	6.40E-05	1.89E+06	1.506	111	1.734E+06	149.53	19.69	24.03	1.09	65	130
Grain20	109	100	6.40E-05	1.70E+06	1.494	91	1.422E+06	164.12	23.35	19.70	1.20	65	112
Grain21	97	100	6.40E-05	1.52E+06	1.641	94	1.469E+06	141.64	20.53	20.35	1.03	65	107
Grain22	151	100	6.40E-05	2.36E+06	1.499	145	2.266E+06	142.92	16.66	31.39	1.04	65	166
Grain23	78	100	6.40E-05	1.22E+06	1.627	67	1.047E+06	159.57	26.61	14.51	1.16	65	82
Grain24	121	100	6.40E-05	1.89E+06	1.529	88	1.375E+06	188.04	26.39	19.05	1.38	65	117
Grain25	171	100	6.40E-05	2.67E+06	1.919	135	2.109E+06	173.43	20.02	29.23	1.27	65	172
Grain26	151	100	6.40E-05	2.36E+06	1.508	118	1.844E+06	175.18	21.58	25.55	1.28	65	151
Grain27	112	100	6.40E-05	1.75E+06	1.273	80	1.250E+06	191.41	28.07	17.32	1.40	65	108
Grain28	154	100	6.40E-05	2.41E+06	1.396	100	1.563E+06	210.25	27.06	21.65	1.54	65	143

Grain29	108	40	2.56E-05	4.22E+06	1.372	73	2.852E+06	202.11	30.67	39.51	1.48	26	102
Grain30	124	40	2.56E-05	4.84E+06	1.704	83	3.242E+06	204.06	28.99	44.92	1.49	26	116
Grain31	118	40	2.56E-05	4.61E+06	1.503	111	4.336E+06	145.86	19.33	60.08	1.06	26	129
Grain32	126	100	6.40E-05	1.97E+06	1.752	88	1.375E+06	195.70	27.24	19.05	1.43	65	120
Grain33	109	100	6.40E-05	1.70E+06	1.646	86	1.344E+06	173.53	25.07	18.62	1.27	65	110
Grain34	59	100	6.40E-05	9.22E+05	1.537	44	6.875E+05	183.45	36.57	9.53	1.34	65	58
Grain36	143	40	2.56E-05	5.59E+06	1.432	102	3.984E+06	191.68	24.90	55.21	1.40	26	138
Grain37	100	40	2.56E-05	3.91E+06	1.558	80	3.125E+06	171.17	25.72	43.30	1.25	26	101
Grain39	64	100	6.40E-05	1.00E+06	1.37	44	6.875E+05	198.76	38.96	9.53	1.45	65	61
Grain40	31	100	6.40E-05	4.84E+05	1.34	28	4.375E+05	151.84	39.61	6.06	1.11	65	33
Grain41	67	100	6.40E-05	1.05E+06	1.67	43	6.719E+05	212.68	41.60	9.31	1.56	65	62
Grain42	98	100	6.40E-05	1.53E+06	1.432	77	1.203E+06	174.24	26.58	16.67	1.27	65	98
Grain43	100	100	6.40E-05	1.56E+06	1.714	66	1.031E+06	206.91	32.86	14.29	1.52	65	93
Grain44	112	100	6.40E-05	1.75E+06	1.516	105	1.641E+06	146.35	19.92	22.73	1.07	65	122
Grain45	105	100	6.40E-05	1.64E+06	1.7	70	1.094E+06	204.87	31.66	15.16	1.50	65	98
Grain46	133	100	6.40E-05	2.08E+06	1.491	124	1.938E+06	147.15	18.41	26.85	1.07	65	144
Grain47	89	100	6.40E-05	1.39E+06	1.737	81	1.266E+06	150.70	23.18	17.54	1.10	65	96
Grain49	121	100	6.40E-05	1.89E+06	1.97	80	1.250E+06	206.55	29.82	17.32	1.51	65	113
Grain50	110	100	6.40E-05	1.72E+06	1.523	103	1.609E+06	146.53	20.13	22.30	1.07	65	120
Grain51	66	100	6.40E-05	1.03E+06	1.725	54	8.438E+05	167.42	30.75	11.69	1.22	65	67
Grain52	128	100	6.40E-05	2.00E+06	1.539	96	1.500E+06	182.43	24.68	20.78	1.33	65	126
Grain53	94	40	2.56E-05	3.67E+06	1.31	67	2.617E+06	191.82	30.71	36.26	1.40	26	90
Grain54	75	100	6.40E-05	1.17E+06	1.54	81	1.266E+06	127.23	20.42	17.54	0.93	65	88
Grain55	61	100	6.40E-05	9.53E+05	1.43	61	9.531E+05	137.30	24.89	13.21	1.00	65	69
Grain56	82	40	2.56E-05	3.20E+06	1.696	46	1.797E+06	242.75	44.77	24.90	1.78	26	72
Grain57	109	100	6.40E-05	1.70E+06	1.805	91	1.422E+06	164.12	23.35	19.70	1.20	65	112
Grain58	161	100	6.40E-05	2.52E+06	1.491	126	1.969E+06	174.93	20.86	27.28	1.28	65	161
Grain59	71	100	6.40E-05	1.11E+06	1.752	72	1.125E+06	135.41	22.68	15.59	0.99	65	80

Grain60	55	40	2.56E-05	2.15E+06	1.562	38	1.484E+06	197.79	41.76	20.57	1.45	26	52
Grain61	60	40	2.56E-05	2.34E+06	1.7	39	1.523E+06	210.04	43.24	21.11	1.54	26	56
Grain62	119	100	6.40E-05	1.86E+06	1.338	71	1.109E+06	228.49	34.32	15.37	1.68	65	107
Grain63	107	100	6.40E-05	1.67E+06	1.56	78	1.219E+06	187.61	27.98	16.89	1.37	65	104
Grain64	128	40	2.56E-05	5.00E+06	1.404	110	4.297E+06	159.49	20.78	59.54	1.16	26	134
Grain65	63	100	6.40E-05	9.84E+05	1.34	66	1.031E+06	131.12	23.12	14.29	0.95	65	73
Grain66	51	100	6.40E-05	7.97E+05	1.469	58	9.063E+05	120.88	23.23	12.56	0.88	65	61
Grain68	41	100	6.40E-05	6.41E+05	1.84	39	6.094E+05	144.26	32.29	8.44	1.05	65	45
Grain69	61	100	6.40E-05	9.53E+05	1.566	43	6.719E+05	193.92	38.65	9.31	1.42	65	58
Grain70	41	100	6.40E-05	6.41E+05	2.08	30	4.688E+05	186.92	44.94	6.50	1.37	65	40
Grain71	93	100	6.40E-05	1.45E+06	1.521	64	1.000E+06	198.57	32.29	13.86	1.45	65	88
Grain72	47	100	6.40E-05	7.34E+05	1.564	45	7.031E+05	143.34	29.92	9.74	1.04	65	52
Grain73	28	100	6.40E-05	4.38E+05	1.267	24	3.750E+05	159.90	44.50	5.20	1.17	65	29
Grain74	45	100	6.40E-05	7.03E+05	1.03	25	3.906E+05	245.07	61.17	5.41	1.80	65	39
Grain75	134	100	6.40E-05	2.09E+06	1.639	81	1.266E+06	225.58	31.81	17.54	1.65	65	121
Grain76	120	40	2.56E-05	4.69E+06	1.796	71	2.773E+06	230.38	34.55	38.43	1.69	26	107
Grain77	125	100	6.40E-05	1.95E+06	1.96	86	1.344E+06	198.61	27.88	18.62	1.45	65	119
Grain78	88	100	6.40E-05	1.38E+06	1.25	49	7.656E+05	244.53	43.64	10.61	1.80	65	77
Grain80	94	100	6.40E-05	1.47E+06	1.456	65	1.016E+06	197.63	31.93	14.07	1.45	65	89
Grain81	120	100	6.40E-05	1.88E+06	1.947	86	1.344E+06	190.79	27.00	18.62	1.40	65	116
Grain83	106	40	2.56E-05	4.14E+06	1.6	112	4.375E+06	130.02	17.65	60.62	0.95	26	123
Grain84	167	40	2.56E-05	6.52E+06	1.767	138	5.391E+06	165.79	19.12	74.69	1.21	26	171
Grain85	107	100	6.40E-05	1.67E+06	1.472	98	1.531E+06	149.76	20.98	21.22	1.09	65	115
Grain86	70	40	2.56E-05	2.73E+06	1.77	46	1.797E+06	207.79	39.48	24.90	1.52	26	65
Grain87	95	40	2.56E-05	3.71E+06	1.614	79	3.086E+06	164.76	25.13	42.76	1.20	26	98
Total	7508		4.288E-03	1.751E+06	1.58	5849	1.364E+06	175.72	3.41	18.90	1.2836		

Vidro utilizado: CN1; ND: 13736; RhoD: 2714399.77; Zeta: 102.25; Lambda D: 1.55E-10; Area: 6.40E-07; Grãos: 76; Pooled age: 175.71 ± 3.41; χ^2 : 92.6; degrees: 75; P(χ^2): 8.2%.

Tabela: Dados obtidos para cálculo da idade de traços de fissão da amostra LIS-39A

Grain	NS	NA	Area (cm ²)	RhoS (cm ⁻²)	Dpar	NI	Rhol (cm ⁻²)	FT age	1s	U ppm	Ns/Ni	Squares	Psj	Pij	(Nsj-Psj) ² /Psj
Grain1	47	100	6.40E-05	7.34E+05	1.262	28	4.375E+05	231.97	55.41	5.98	1.68	65	42	33	0.5
Grain2	101	100	6.40E-05	1.58E+06	1.569	80	1.250E+06	175.25	26.27	17.08	1.26	65	102	79	0.0
Grain3	43	100	6.40E-05	6.72E+05	1.492	28	4.375E+05	212.55	51.65	5.98	1.54	65	40	31	0.2
Grain4	79	100	6.40E-05	1.23E+06	1.582	58	9.063E+05	188.87	32.70	12.38	1.36	65	77	60	0.0
Grain6	64	100	6.40E-05	1.00E+06	1.539	52	8.125E+05	170.90	31.94	11.10	1.23	65	65	51	0.0
Grain7	88	100	6.40E-05	1.38E+06	1.629	68	1.063E+06	179.57	29.03	14.52	1.29	65	88	68	0.0
Grain9	32	100	6.40E-05	5.00E+05	1.879	22	3.438E+05	201.49	55.83	4.70	1.45	65	30	24	0.1
Grain10	55	100	6.40E-05	8.59E+05	1.587	27	4.219E+05	280.45	65.94	5.76	2.04	65	46	36	1.7
Grain11	81	100	6.40E-05	1.27E+06	1.489	38	5.938E+05	293.17	57.70	8.11	2.13	65	67	52	2.9
Grain12	46	100	6.40E-05	7.19E+05	1.352	28	4.375E+05	227.12	54.47	5.98	1.64	65	42	32	0.5
Grain13	39	100	6.40E-05	6.09E+05	1.211	29	4.531E+05	186.51	45.76	6.19	1.34	65	38	30	0.0
Grain14	87	100	6.40E-05	1.36E+06	1.752	58	9.063E+05	207.69	35.25	12.38	1.50	65	82	63	0.4
Grain15	178	100	6.40E-05	2.78E+06	1.34	143	2.234E+06	172.82	19.46	30.53	1.24	65	181	140	0.0
Grain16	46	100	6.40E-05	7.19E+05	1.5	53	8.281E+05	120.99	24.40	11.32	0.87	65	56	43	1.7
Grain17	156	100	6.40E-05	2.44E+06	1.66	154	2.406E+06	140.99	16.06	32.88	1.01	65	174	136	1.9
Grain18	180	100	6.40E-05	2.81E+06	1.63	130	2.031E+06	191.95	22.15	27.76	1.38	65	174	136	0.2
Grain19	117	100	6.40E-05	1.83E+06	1.59	118	1.844E+06	138.03	18.05	25.20	0.99	65	132	103	1.8
Grain20	137	100	6.40E-05	2.14E+06	1.58	108	1.688E+06	176.07	22.71	23.06	1.27	65	138	107	0.0
Grain21	116	100	6.40E-05	1.81E+06	1.728	101	1.578E+06	159.62	21.77	21.57	1.15	65	122	95	0.3
Grain22	81	100	6.40E-05	1.27E+06	1.07	72	1.125E+06	156.39	25.37	15.37	1.13	65	86	67	0.3
Grain23	66	100	6.40E-05	1.03E+06	1.31	41	6.406E+05	222.62	44.31	8.75	1.61	65	60	47	0.6
Grain24	34	100	6.40E-05	5.31E+05	1.61	20	3.125E+05	234.88	66.22	4.27	1.70	65	30	24	0.4
Total	1873		1.41E-03	1.33E+06	1.52	1456	1.034E+06	178.52	6.42	14.13	1.29				13.1

Vidro utilizado: CN1; ND: 13736; RhoD: 2752323.988; Zeta: 102.25; Lambda D: 1.55125E-10; Area: 6.40E-07; Grãos: 22; Pooled age: 178.51 ± 6.42; χ²: 29.91%; degrees: 21; P(χ²): 9.4%.

Tabela: Dados obtidos para cálculo da idade de traços de fissão da amostra A-42.1

Grain	NS	NA	Area (cm ⁻²)	RhoS (cm ⁻²)	Dpar	NI	Rhol (cm ⁻²)	FT age	1s	U ppm	Ns/Ni	Squares	Psj	Pij	I
Grain1	61	100	6.40E-05	9.53E+05	1.98	40	6.250E+05	200.54	40.84	9.00	1.53	65	54	47	
Grain2	82	100	6.40E-05	1.28E+06	1.256	63	9.844E+05	171.54	28.78	14.17	1.30	65	78	67	
Grain3	41	100	6.40E-05	6.41E+05	1.593	30	4.688E+05	180.00	43.27	6.75	1.37	65	38	33	
Grain4	61	100	6.40E-05	9.53E+05	1.355	63	9.844E+05	128.04	23.03	14.17	0.97	65	67	57	
Grain5	71	100	6.40E-05	1.11E+06	1.264	57	8.906E+05	164.26	29.25	12.82	1.25	65	69	59	
Grain6	101	100	6.40E-05	1.58E+06	1.653	103	1.609E+06	129.66	18.19	23.17	0.98	65	110	94	
Total	417		3.20E-04	1.30E+06	1.517	356	1.113E+06	154.58	11.23	16.02	1.17				

Vidro utilizado: CN1; ND: 13736; RhoD: 2612521.079; Zeta: 102.25; Lambda D: 1.55125E-10; Area: 6.40E-07; Grãos: 6; Pooled age: 154.58 ± 11.23; χ₂: 3.67%; degrees: 5; P(χ₂): 59.8%

Tabela: Dados obtidos para modelagem térmica das amostras LIS-49, LIS-39A e A-42.1

Sample-LIS49												Sample-LIS39A		
length	angle	Dpar	length	angle	Dpar	length	angle	Dpar	length	angle	Dpar	length	angle	Dpar
10.392	85.938	1.599	10.972	63.018	1.624	9.336	40.755	1.432	11.697	55.888	1.487	9.261	85.977	1.309
11.961	89.356	1.599	11.279	59.308	1.624	11.182	69.044	1.432	11.568	58.932	1.487	8.237	16.656	1.309
12.134	81.218	1.599	10.906	37.228	1.624	12.025	37.541	1.432	12.471	57.001	1.487	10.146	40.364	1.309
11.354	77.926	1.599	10.073	39.016	1.624	13.721	77.474	1.432	9.68	73.675	1.487	7.363	54.471	1.314
11.645	87.512	1.599	9.022	52.703	1.55	9.982	74.503	1.432	13.886	27.946	1.487	10.378	57.271	1.469
11.47	37.654	1.814	9.172	67.593	1.55	13.54	77.274	1.434	12.086	82.101	1.487	11.095	72.947	1.469
11.668	41.877	1.814	9.571	53.058	1.55	11.922	33.431	1.434	14.574	25.027	1.487	8.954	68.095	1.292
10.443	71.742	1.814	11.26	46.973	1.55	9.185	33.337	1.496	12.546	49.336	1.802	9.09	76.475	1.292
8.891	35.037	1.814	9.976	41.479	1.55	8.78	22.846	1.496	11.75	56.266	1.802	13.047	26.553	1.292
9.907	43.225	1.814	15.337	50.167	1.548	11.096	53.563	1.496	11.658	55.695	1.802	10.336	39.125	1.749
10.842	25.132	1.492	12.138	89.505	1.548	14.328	85.487	1.496	13.35	52.621	1.802	8.661	85.462	1.749
11.295	67.76	1.492	12.174	51.868	1.548	11.31	32.279	1.817	10.931	65.402	1.802	10.809	6.974	1.438
10.777	70.132	1.492	10.482	80.894	1.548	11.745	69.067	1.817	13.408	55.224	1.802	14.494	79.568	1.144
11.271	65.852	1.492	12.192	60.307	1.548	7.913	61.731	1.817	10.371	67.334	1.802	12.292	36.739	1.144
11.208	45.816	1.492	9.8	64.041	1.529	12.002	58.7	1.817	10.719	24.16	1.802	12.956	39.671	1.681
11.162	53.273	1.492	10.089	73.41	1.529	13.851	56.259	1.817	15.259	19.946	1.802	9.219	43.447	1.681
10.759	25.761	1.492	13.9	65.371	1.377	11.846	39.129	1.817	11.725	63.542	1.802	10.829	23.916	1.681
12.15	34.962	1.635	13.794	47.635	1.377	13.214	81.8	1.423	12.003	42.444	1.281	11.766	54.978	1.353
11.353	78.756	1.635	10.002	77.464	1.377	13.607	71.362	1.423	8.816	53.67	1.281	8.287	29.865	1.353
9.753	36.691	1.635	11.748	38.036	1.377	12.154	81.046	1.423	12.059	68.135	1.281	9.438	79.522	1.353
8.477	30.037	1.635	10.832	73.335	1.377	12.679	88.177	1.423	8.856	59.322	1.281	10.166	80.994	1.535
11.667	47.219	1.635	11.078	56.025	1.594	11.865	60.426	1.423	8.867	46.399	1.281	11.036	84.993	1.854
12.058	84.206	1.635	11.24	57.877	1.594	13.341	27.947	1.423	12.139	79.937	1.7	7.902	58.152	1.854
12.705	79.136	1.635	12.315	56.35	1.594	14.85	44.083	1.423	10.963	77.515	1.7	9.58	88.921	1.854

10.078	77.911	1.635	12.792	46.583	1.594	12.146	75.385	1.479	11.935	64.758	1.7	9.215	79.733	1.854
11.813	8.265	1.635	11.1	42.225	1.594	8.982	72.972	1.479	12.807	83.914	1.7	9.072	83.2	1.355
12.821	56.075	1.334	11.12	83.335	1.278	11.745	86.439	1.722	8.788	87.582	1.677	11.802	4.908	1.614
11.778	77.852	1.334	12.253	44.8	1.278	8.695	0.035	1.722	14.083	82.386	1.677	11.042	24.282	1.555
12.589	68.301	1.334	12.96	71.098	1.278	8.853	65.345	1.722	9.834	42.699	1.677	8.052	12.216	1.555
12.338	62.96	1.334	10.827	64.819	1.278	10.597	45.608	1.722	11.274	74.258	1.677	12.505	32.061	1.555
11.86	40.18	1.334	11.756	49.127	1.403	8.908	3.166	1.722	9.493	46.874	1.718	12.597	73.274	1.555
11.399	64.29	1.334	12.078	30.803	1.403	9.532	23.091	1.722	15.359	44.019	1.718	8.699	58.661	1.555
11.167	59.318	1.334	12.247	38.227	1.403	10.437	22.606	1.722	11.74	68.059	1.718	9.51	8.181	1.555
14.108	43.602	1.334	11.884	28.356	1.403	12.437	2.97	1.764	9.879	28.804	1.718	14.612	69.294	1.554
12.043	72.247	1.236	11.73	26.503	1.444	10.665	6.121	1.764	9.984	80.206	1.718	9.859	77.428	1.554
8.473	11.219	1.236	13.83	82.879	1.444	8.31	49.838	1.764	8.356	55.973	1.718	8.38	60.329	1.554
10.038	74.801	1.236	8.319	83.534	1.444	10.327	15.823	1.652	7.944	57.175	1.718	9.536	49.809	1.554
9.16	60.026	1.236	10.966	61.712	1.257	10.138	41.784	1.652	7.622	70.427	1.718	8.413	82.326	1.554
8.553	81.925	1.236	10.099	51.29	1.257	10.754	82.35	1.652	10.102	83.133	1.004	10.582	40.249	1.554
12.752	44.178	1.236	10.986	68.799	1.552	11.016	71.819	1.652	9.907	83.684	1.004	8.799	71.695	1.554
11.922	48.116	1.236	12.146	49.934	1.552	12.349	57.221	1.652	11.238	89.577	1.004	10.694	1.856	1.554
10.419	84.523	1.436	9.835	86.271	1.552	9.647	58.424	1.652	9.077	26.589	1.004	11.326	33.617	1.554
14.319	10.24	1.436	14.106	47.516	1.552	10.422	41.994	1.652	11.419	52.001	1.724	13.645	61.423	1.597
10.167	45.641	1.436	11.728	82.966	1.669	12.59	68.378	1.652	10.205	70.549	1.724	10.565	77.101	1.597
13.728	46.077	1.454	12.042	32.816	1.669	9.812	71.793	1.715	11.18	68.006	1.724	9.652	88.862	1.597
10.475	78.069	1.454	9.208	82.131	1.574	11.422	8.64	1.715	10.65	58.759	1.724	9.059	56.951	1.597
14.812	52.333	1.454	13	38.172	1.574	9.574	36.034	1.839	10.577	67.997	1.724	8.993	76.56	1.597
11.369	55.989	1.454	11.585	55.296	1.574	11.986	47.646	1.839	10.215	62.169	1.724	13.897	77.842	1.456
12.502	69.809	1.454	11.578	72.598	1.574	10.306	70.103	1.839	9.338	65.191	1.724	9.815	83.819	1.456
12.994	41.572	1.685	9.315	72.119	1.574	12.279	81.676	1.602	12.329	77.851	1.724	12.162	84.488	1.456
13.708	10.908	1.685	10.909	30.177	1.631	10.245	50.887	1.602	9.286	77.662	1.724	9.775	44.151	1.456
11.828	73.001	1.685	8.624	79.719	1.631	10.748	71.732	1.602	9.986	71.725	1.594	11.026	64.916	1.456

10.431	42.985	1.685	12.161	59.544	1.631	11.471	18.084	1.602	11.865	46.759	1.594	10.682	78.448	1.259
13.225	66.396	1.685	11.846	55.317	1.631	13.708	52.13	1.602	12.296	45.695	1.594	9.608	43.389	1.259
11.697	54.244	1.685	12.152	50.019	1.631	12.744	17.054	1.602	9.615	53.056	1.594	10.681	51.568	1.259
11.836	25.95	1.374	10.029	86.7	1.631	10.951	10.615	1.421	10.314	54.462	1.594	8.346	66.758	1.259
10.549	52.511	1.616	12.646	53.929	1.631	9.64	20.363	1.421	8.533	51.839	1.664	7.867	58.272	1.369
8.908	58.108	1.616	7.233	72.831	1.408	11.151	81.595	1.421	10.954	69.925	1.664	8.24	10.939	1.369
10.034	59.618	1.616	6.914	39.742	1.408	10.309	66.527	1.421	11.246	74.274	1.664	8.055	39.613	1.379
13.04	74.741	1.616	7.026	38.351	1.408	10.485	57.421	1.421	12.146	50.074	1.664	8.014	50.455	1.379
12.376	22.617	1.616	7.298	75.274	1.408	12.087	61.299	1.683	11.625	27.082	1.664	Sample-A-42.1		
9.663	82.804	1.519	8.159	39.705	1.335	13.292	57.897	1.683	9.739	59.085	1.664	length	angle	Dpar
10.871	78.271	1.519	15.596	60.204	1.469	14.094	48.154	1.683	11.839	61.731	1.664	11.634	35.508	1.461
8.066	59.536	1.519	10.108	38.029	1.469	13.91	58.118	1.683	13.81	42.417	1.51	9.488	78.734	1.461
10.298	37.548	1.519	10.053	38.085	1.469	10.016	79.047	1.683	11.318	61.537	1.51	9.467	63.204	1.461
11.151	73.487	1.519	8.241	67.477	1.469	12.673	30.162	1.683	11.653	55.428	1.51	12.491	16.676	1.392
11.4	85.402	1.519	11.976	65.793	1.469	12.722	0.496	1.683	11.38	74.751	1.51	12.447	74.476	1.392
9.526	74.031	1.519	12.129	82.77	1.469	12.117	54.467	1.683	13.153	60.038	1.51	9.699	73.844	1.392
10.267	39.833	1.495	8.393	36.006	1.469	11.229	14.698	1.683	11.301	51.234	1.51	11.546	70.783	1.392
9.836	86.286	1.495	9	38.986	1.141	14.412	74.462	1.487	11.743	49.436	1.51	10.245	77.971	1.392
9.33	51.294	1.495	8.607	77.553	1.141	10.552	54.591	1.487	13.551	38.132	1.51	11.889	15.286	1.392
8.858	74.85	1.495	12.63	34.265	1.141	9.566	78.786	1.487	10.709	71.029	1.51	13.373	87.679	1.392
9.654	69.618	1.495	10.756	55.914	1.141	10.649	63.127	1.487	12.055	53.143	1.51	9.08	83.286	1.392
12.333	58.441	1.676	10.123	46.978	1.141	8.702	68.049	1.487	10.17	39.75	1.51	10.176	38.798	1.392
10.941	81.637	1.676	12.737	66.493	1.546	13.383	81.511	1.487	10.814	75.088	1.51	12.993	22.466	1.392
8.816	73.64	1.419	9.176	13.839	1.546	12.2	52.03	1.487	11.521	70.271	1.51	11.324	12.064	1.185
10.253	56.295	1.419	10.007	88.266	1.546	13.049	47.416	1.487	11.955	39.208	1.737	11.242	73.91	1.185
11.918	28.142	1.624	12.479	5.153	1.546	11.575	46.803	1.487	8.684	30.185	1.737	9.695	58.705	1.185
11.722	48.992	1.624	11.621	21.584	1.6	10.676	40.794	1.487	10.105	54.464	1.737	12.273	63.498	1.185
11.537	73.575	1.624	11.398	79.902	1.647	12.119	44.225	1.487	11.462	58.21	1.737			

10.862	79.547	1.624	11.937	0.83	1.647	10.83	74.766	1.487	9.981	38.846	1.737		
11.997	45.091	1.624	10.958	47.262	1.647	10.86	73.497	1.487	11.155	15.277	1.737		